

A 1m Normal Incidence Multi-Channel
Spectrometer For Laser Plasma Spectroscopy

A thesis for the degree of
Master of Science

submitted to

School of Physical Sciences
Dublin City University

by

Barry Doyle B.Sc.

Research Supervisor
Dr. John T. Costello

September 1995.

Declaration

I hereby certify that this material, which I now submit for assessment on the programme of study to the award of Masters of Science, is entirely my own work and has not been taken from the work of others save and to the extent that such work has been cited and acknowledged within the text of my work.

Signature: Barry Doyle

Date: 20 Sept 1995

To Breege and my parents

Table of Contents

Chapter 1 Introduction

1 1	Laser Produced Plasma Physics - An Overview	
1 1 1	Introduction	2
1 1 2	Review of Laser Plasma Properties	3
1 1 3	Formation of Laser Produced Plasmas	4
1.2	Background to Carbon Plasma Diagnostics	
1 2 1	Introduction	9
1 2 2	Early Carbon Laser Plasma Studies	9
1 2 3	Carbon Plasma Analysis	11
1 3	Theory of the Concave Diffraction Grating	
1 3 1	Introduction	14
1 3 2	General Theory	14
1 3 3	Grating Equation	17
1 3 4	Dispersion	18
1 3 5	Resolving Power	21
1 3 6	Grating Efficiency	23
1 4	The Normal Incidence Spectrometer Mount	
1 4 1	Introduction	25
1 4 2	General Theory.	25

Chapter 2 Experiment

2 0	Introduction	31
2 1	The Acton VM-521 1m Spectrometer	
2 1 1	General Specification	32
2.1.2	Entrance Slit Assembly	32
2 1 3	Exit Slit Assembly	32
2.1.4	Bausch & Lomb Concave Grating	33

2.1.5	SpectraDrive Controller	33
2.1.6	Vacuum Specifications	33
2.2	The Galileo Channel Electron Multiplier Array (CEMA)	
2.2.1	Introduction to CEMA's	35
2.2.2	Mode of Operation	36
2.3	The EG&G Optical MultiChannel Analyser	
2.3.1	The Model 1453A Detector	38
2.3.2	The Model 1471A Detector Controller Interface	39
2.3.3	OMA Operation and Specification	39
2.4	The Nd YAG Laser System	45
2.5	Modifications to the Acton VM-521 Spectrometer	
2.5.1	Target Chamber and Mounting Design	47
2.5.2	The Optical Detector Coupling Design	51
2.5.3	The Vacuum System	52
2.6	The PC OmaSoft Package	
2.6.1	Introduction	55
2.6.2	Setup Menu	55
2.6.3	Files Menu	56
2.6.4	Run Menu	56
2.6.5	Math Menu	57
2.6.6	Plot Menu	58
2.6.7	Terminal Menu	58
2.6.8	Parameters Menu	58
2.6.9	Scan Menu	59
2.7	Plasma Radiation - Spectrometer Coupling Considerations	
2.7.1	Basic System Modelling	60
2.8	Experimental Procedures	
2.8.1	Experimental Preparation	62

Chapter 3 Results and Analysis

3 0	Introduction	67
3 1	Noise Levels in the EG&G Photodiode Array	
3 1 1	Introduction	67
3 1 2	Noise Characteristics	67
3 1.3	Analysis of System Noise	69
3 2	Single -vs - Multi-Laser Shot Averaged Spectra	
3 2 1	Introduction	72
3 2 2	Analysis of Spectra Obtained	72
3 3	Spectral Orders in Carbon Emission Spectra	
3 3 1	Introduction	78
3 3 2	Spectral Order Analysis	78
3 4	Comparison of Carbon Spectra from Acton 1m and McPherson 2 2m Vacuum Spectrometers	
3 4 1	Introduction	81
3 4 2	Spectral Wavelength Coverage	81
3 4 3	Resolution Performance	82
3 5	Spectral Resolution Enhancement using Deconvolution Techniques	
3 5 1	Introduction	84
3.5 2	Maximum Likelihood -vs- Fourier Deconvolution	84
3.5 3	Instrument Function	86
3 5 4	Deconvolved Carbon Spectra	87
3 6	Complete Carbon and Tungsten Spectra	
3 6 1	Introduction	89
3 6 2	Spectral Analysis	89

Chapter 4 Conclusions

4 1 Summary Conclusions	92
4 2 Future Work	92
References	94
Acknowledgements	98
Appendix A - Acton Spectrometer	100
Appendix B - Galileo Channel Electron Multiplier Assembly	101
Appendix C - EG&G Optical MultiChannel Analyser	102
Appendix D - Technical Drawings	103

Abstract

The development of a Vacuum-UV (VUV) multichannel recording spectrometer for laser plasma spectroscopy is described. The instrument covers the spectral region 30 - 325nm and complements an existing Extreme-UV (EUV) system covering the 5 - 50nm range. It is based on an Acton Research Corporation (ARC) VM-521 1m normal incidence vacuum spectrometer fitted with a 1024 element VUV linear array detector.

The array detector comprises of a Galileo VUV-25R Channel Electron Multiplier Array (CEMA), butt-coupled to an EG&G Optical Multi-channel Analyser (OMA) system.

The complete set-up was tested using spectra from laser produced plasmas of polyethylene. Selected spectral lines were chosen to illustrate the system performance with respect to resolution, signal to noise ratio etc and compared with both computed and manufacturer stated performance. Potential resolution enhancement using deconvolution procedures is illustrated by preliminary results.

This thesis concludes with a brief description of future work on system optimisation and future applications.

Chapter 1

Introduction

1.1 Laser Produced Plasma Physics - An Overview .

1.1.1 Introduction

The present chapter contains a discussion of the main features, production of and atomic processes associated with laser produced plasmas This discussion is followed by an extensive treatment of the concave grating and normal incidence spectrometer mount

A laser produced plasma (LPP) is generated by focusing the output of a high power laser onto a solid target usually *in vacuo* Although short lived, the plasma emits an intense burst of radiation over a broad spectral range (x-ray to infrared) which makes it ideally suited to spectrographic studies Early investigations of laser produced plasmas concentrated on line emissions originating from multiply ionised species More recently, studies of VUV and EUV continuum emission originating from bremsstrahlung and recombination radiation have shown LPP to be useful as high flux alternatives to more conventional VUV and EUV light sources (e g synchrotrons) The benefits of laser produced plasmas as both photon and ion sources have been cited in previous publications [1 - 5], but it is worth summarising them here

A laser plasma is generated quite easily by a high peak power laser (pulsed) of appropriate characteristics and a suitable target material, preferably but not necessarily moveable in a controlled and pre-determined way to ensure shot to shot reproducibility In most cases the reproducibility of intensity output is better than 5% [1] With a suitable choice of target materials, complete spectral coverage from 40Å to 9000Å can be achieved The type of emission (line - vs - continuum) may also be 'tuned' by choice of target material In general low Z targets yield predominantly lines while intense continua are emitted by rare-earth and other high Z plasmas [3-9]

The duration of the plasma pulse (at least in the Extreme - UV) is determined by the length of the optical output pulse of the laser ($\approx 15\text{ns}$) This short time scale makes the laser produced plasma particularly suitable for time-resolved spectroscopy

Laser produced plasmas have proved to be a valuable source of highly ionised species Since highly ionised atoms do not occur naturally on earth, the large densities of electrons and ions generated by the laser plasma make it particularly suitable for spectral comparison of stellar interiors. The state of ionisation observed from a LPP can be varied by (1) adjusting the focusing conditions of the laser pulse on the target and

(2) locating the plasma plume so as to optimise the ion stage observed by the spectral detector

The spectra of laser produced plasmas on targets of moderate to high Z, show a remarkable continuum emission over a wide wavelength range [6] These continua are very useful for absorption spectroscopy, microscopy, lithography etc and offer an alternative to the synchrotron radiation source, when polarised radiation is not required (although the addition of multilayer optics can provide polarised narrow band light from LPP for particular geometry's if required) Because of the pulsed mode of the LPP and its point like emission, these continua are very suitable for applications requiring time and space resolved studies

The vacuum pressure in the chamber containing the target can be varied with little or no effect on the nature of the plasma radiation Usually the target chamber is vacuum isolated from the spectrographic detector by means of a LiF window (105nm - visible) or by a differential pressure assembly

Laser plasmas are characterised by their high electron and ion densities and temperatures The density of the plasma core may be as high as $10^{17} - 10^{22} \text{ cm}^{-3}$, with electron temperatures typically 10 - 1000eV (1eV = 10000°K) It is possible for the plasma density at the core to exceed that of its parent matter (e.g. in Inertial Confinement Fusion experiments)

1.1.2 Review of Laser Plasma Properties

It is estimated that 99% of all matter in the universe is present in the form of plasma [1] In its simplest terms, a plasma is a collection of electrons and ions An ion is an atom from which one or more electrons have been removed Overall neutrality is maintained in the transition from neutral matter to ions and electrons i.e

$$n_e = \sum_z n_z z \quad (11)$$

where n_e is the electron density number, n_z is the density of ions of charge z

The behaviour of the plasma is markedly different to that of its parent matter, due to the strong and long-range Coulombic force between charged particles in the plasma The Coulombic force is so dominant in the plasma that a considerable number of particles in the plasma respond collectively to any perturbing field This collective behaviour may be

considered to be a basic plasma pre-requisite and is characterised by the so-called Debye Length, λ_d . This quantity is the distance over which Coulombic forces act within the plasma before being counterbalanced by other surrounding species, i.e. it is a measure of the shielding effect of surrounding species on a charged particle (ion) within the plasma. The Debye length (m k s) is expressed as

$$\lambda_d = \left(\frac{\epsilon_0 k T}{n_e e^2} \right)^{1/2} = 69.0 (T / n_e)^{1/2} \quad (1.2)$$

where T is the electron temperature (in Kelvin), n_e is the electron number density (m^{-3}), and the other terms have their usual meaning. For $n_e = 10^{25} / m^3$ then $\lambda_d = 21.8 \text{ nm}$

If the collective behaviour is to dominate, then the dimensions of the plasma system L must satisfy $L \gg \lambda_d$. This collective behaviour results in plasma oscillations having an angular frequency of

$$\omega_p = \left(\frac{n_e e^2}{m_e \epsilon_0} \right)^{1/2} = 56.4 n_e^{1/2} \quad (1.3)$$

where the quantity ω_p is usually known as the plasma frequency. For $n_e = 10^{25} / m^3$ then $\omega_p \approx 1.8 \times 10^{14} \text{ rads sec}^{-1}$

The plasma frequency determines the response of the plasma to the incoming laser radiation of frequency ω . The dispersion relation for electromagnetic waves travelling through a plasma is given by

$$\omega^2 = \omega_p^2 + c^2 k^2 \quad (1.4)$$

Since an electron density gradient exists in a LPP, ω_p varies according to equation 1.3 so that in the range for $\omega_p < \omega$, k is real and the EM laser wave propagates, where $\omega_p > \omega$, k is imaginary and the wave is reflected at this position (deflagration zone). This density is called the critical density n_c (m^{-3}) and is found from equation 1.3 to be

$$n_c = \frac{\epsilon_0 m_e \omega^2}{e^2} = 3.14 \times 10^{-4} \omega^2 \quad (1.5)$$

1.1.3 Formation of Laser Produced Plasma

The evolution of a LPP is characterised by two phases , initiation and growth [1] The initiation process is different for conducting and insulating target materials This is due to the higher ionisation energies associated with insulating materials The threshold power density for plasma formation varies with the operating wavelength of the laser due to the wavelength dependent absorbance of the target surface

- **Initiation of Plasma**

When the electromagnetic (EM) field of the laser radiation is focused onto a metallic surface, it penetrates to a depth of less than one laser wavelength and causes rapid vaporisation of the condensed-phase matter into gases. This depth is commonly referred to as the skin depth δ , and is related to the metal conductivity (σ) by

$$\delta = (\pi f \mu_0 \sigma)^{-1/2} \text{ (m k s units)} \quad (16)$$

where μ_0 is the permeability of free space, f is the frequency of the laser radiation and σ is the conductivity in mhos m^{-1}

For aluminium with $\sigma = 3.54 \times 10^7$ mhos m^{-1} with a Nd YAG laser of frequency 2.81×10^{14} Hz, the depth of penetration of the laser radiation is $\delta \approx 5\text{nm}$ The electric field vector is such that it strips electrons from the surface of the metal The r m s electric field (E) is related to the irradiance ϕ (W m^{-2}) by

$$\bar{E}_{rms} = 19.4\phi^{1/2} \text{ (V cm}^{-1}\text{)} \quad (17)$$

In the set-up used for this thesis, a Nd YAG laser is used with an irradiance of $\phi \approx 10^{15}$ W m^{-2} E_{rms} has a corresponding value of $6 \times 10^8 \text{ Vcm}^{-1}$, which is greater than the typical ionisation potential of valence and sub-valence electrons Collisions between free electrons and the vaporised matter leads to a rise in temperature and pressure of the gas The net effect is to produce a cold, low density plasma over the target surface

For an insulating materials the E-field strength can be less than the ionisation potential of the material However, for sufficiently large radiation fluxes, primary electrons are generated because of surface imperfections, impurities and non-linear effects such as Multi-Photon Ionisation (MPI)[2 and references therein] Once these priming electrons are produced, heating, evaporation and ionisation begin, forming a low density, cold plasma above the target surface as for the metallic target

- **Growth of Plasma**

Growth of the subsequent plasma is identical for both insulating and conducting materials. The incoming radiation is absorbed in the primary plasma by means of Inverse Bremsstrahlung (IB). The rate of absorption K_w is dependent on n_e^2 when $\omega \gg \omega_p$. The absorbed energy causes an increase in the kinetic energy of the electrons (i.e. increase in electron temperature) until such time as the electron number density n_e approaches that of the critical density n_c . At this point the plasma becomes opaque to the incoming radiation and in fact, reflects it back towards the laser. Laser radiation is no longer reaching the target surface to generate new plasma material. However because the plasma is being driven away from the target at high velocities, the electron density decreases and radiation again reaches the target. This self-regulating operation occurs continuously over the duration of the laser pulse.

The electron temperature reaches uniform equilibrium very quickly which implies a high thermal conductivity. The energy gained by the electrons through IB, is transferred to the ions by collisions. The time taken for equilibrium to be attained by the ions (electron/-ion thermalisation time) is dependent on Z (atomic number) and T_e and may not be achieved over the duration of the laser pulse.

1.1.4 Atomic Processes in Laser Produced Plasmas

Electrons lose energy by elastic and inelastic collisions with particles through excitation of the electronic states of atoms and ions in a plasma. Some electrons will be lost by attachment, but new electrons will be generated by ionising collisions. If the laser irradiance is high enough, then a few electrons will gain energy larger than the ionisation potential (in spite of all the loss mechanisms). These electrons in turn will generate new electrons by impact ionisation of atoms and lead to the cascade growth of the plasma. An important point regarding these processes is that usually, for each such process in the plasma, an opposite process exists also. The main atomic processes in a LPP are listed below [1]

- *Bound-Bound* (Collision Excitation/De-Excitation)
(B - B) (Photo-Excitation/De-Excitation)
- *Free-Bound* (Collisional Ionisation/Recombination)
(B - F) (Photo-Ionisation/Recombination)
- *Free-Free* (Bremsstrahlung /
(F - F) Inverse Bremsstrahlung)

- Bound-Bound Transitions

When an atom or ion makes a transition from one bound energy state to another state of lower energy, the energy of the emitted photon is well defined. In the absence of external perturbations the transition gives rise to a spectral line whose profile depends upon the spontaneous lifetime of the initial state, Stark (Ion-Field) broadening and Doppler shifting due to electron velocity distributions. This type of transition is characterised by line radiation.



(Photoexcitation/ De-excitation)



(Collision Excitation/ De-excitation)

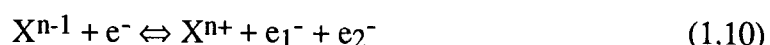
In a cool partially ionised gas ($T_e = 1\text{eV}$), much of the line radiation will be in the infrared-visible regions. As the temperature rises, atoms can be raised to more energetic excited states and thus tend to emit lines of shorter wavelengths. At sufficiently high temperatures, when virtually all the ions are reduced to bare nuclei, bound-bound line radiation ceases.

- Bound-Free Transitions

When a free electron is captured by an n -times ionised atom and makes a transition to a bound state of the $(n-1)$ times ionised atom, the surplus energy may be emitted as a photon. The emission is known as recombination radiation.



For a particular final bound state, the emission spectrum is a continuum with a fairly sharp low-frequency cut-off (recombination limit). Each bound state will have its own continuum, and these overlap. The inverse process to recombination radiation is known as photoionization, i.e. a photon transfers enough energy to an atom to eject an electron from a bound state. For electrons the corresponding processes are electron impact ionisation and 3-body recombination.



- Free-Free Transitions

Free-free radiation or Bremsstrahlung occurs when high energy photons/electrons collide with other particles upon traversing a plasma and emit radiation as they slow down. The spectrum is characterised by a continuum emission. In a sufficiently hot plasma ($T_e > 1\text{KeV}$) of moderate atomic number target, most of the ions are stripped of all their orbital electrons, and electron-ion Bremsstrahlung is the dominant radiation mechanism.

The relative importance of each of these three atomic processes is dependent in large measure on the atomic number of the target material as will be illustrated later when emission spectra of carbon ($Z=6$) and tungsten ($Z=74$) are presented

1.2

Background to Carbon Plasma Diagnostics

1.2.1

Introduction

With the invention of the Q-switched ruby laser (McClung & Hellworth)[15], the available laser pulse power was immediately raised from the kW to MW range. The first measurements taken from laser heated plasmas was reported by Linlor [16] who found that the distribution of ion energies emitted from varying atomic mass targets consistently had a maximum energy of 1keV. It was later shown by Isenor [17] that the energy of the fastest ions was directly proportional to the peak laser power density. Carbon was a popular target material used for plasma diagnostics during the early years of high power laser produced plasmas. Initial studies concentrated on electron/ion densities, electron temperature distributions, momentum transfer, plasma duration studies and spatial profiling.

1.2.2

Early Carbon Laser Plasma Studies.

Bazov et al [18], using a Nd: glass laser providing 200MW peak power pulses in 15ns, investigated a carbon plasma expansion by means of (1) an electrostatic probe, (2) by high speed streak photography and (3) by shadow photography of the plasma using some of the Nd laser radiation and a gated image converter. The screened Faraday cylinder probe received a potential which was first negative, corresponding to the halo of electrons surrounding the plasma, then fell to zero and became positive as the rest of the plasma moved past. The time of passage for the surface of charge neutrality in the plasma was measured accurately and was found to vary with the fourth root of the peak laser power. Subsequent work [19] using a Mach-Zehnder interferometer allowed a detailed picture of the density and velocity profiles in the plasma to be constructed together with the vaporisation rate (4 gm s^{-1}) and peak plasma pressure ($2.5 \times 10^6 \text{ atm}$) values.

Koopman [20] et al using a cylindrical Langmuir probe examined the plasma expansion properties from a carbon foil target irradiated by a ruby laser with peak powers up to 200MW. Table 1.1 shows the experimental values obtained.

Target Thickness (cm)	0.025
Front Velocity (cm μs^{-1})	17.5
Front Ion Kinetic Energy (keV)	1.85
Peak Electron Density (10^{11} cm^{-3})	10.5
Velocity of Electron Density Peak (cm μs^{-1})	13.5

Table 1.1: Measurements on plasmas expanding at a distance of 32.6mm from the target.

Boland et al [21], also Boland & Irons [22] investigated plasmas produced from a polyethylene target by a ruby laser with a peak output power of about 300MW. They made detailed space-resolved measurements of both C V and C VI free-bound continuum intensities, and deduced the electron temperature distribution. Boland *et al* also carried out the spectroscopic equivalent of time-of-flight measurements on ions from carbon plasmas, by measuring the time-dependence of line-intensities emitted from small elements of the plasma at various distances z from the target surface. The results at $z=2.5$, and 10mm are shown in Figure 1.1

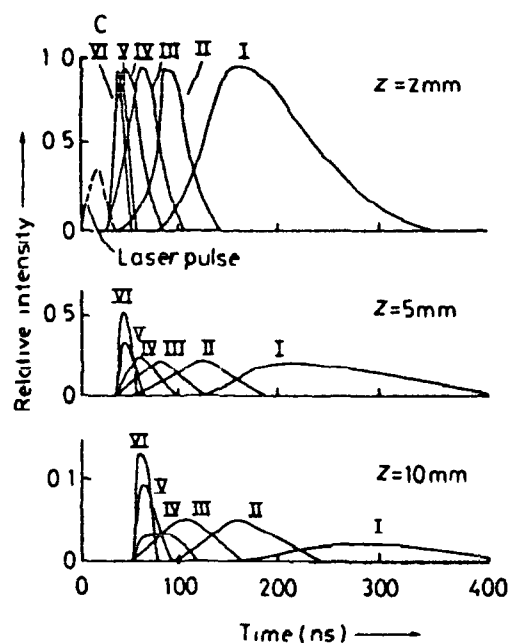


Figure 1.1: Line Intensities emitted from elements of a polyethylene plasma at three different distances from the target surface (Boland et al (1968))

The distance of the region of peak intensity from the target surface is plotted for each ion as a function of time in Figure 1.1. Most of the radiation emitted in the visible region comes from the less highly ionised atoms, which explains why streak photography shows lower velocities than those obtained from time of flight of the fastest ions. Clearly X-ray streak photography would match ion kinetic measurements better.

From the absolute intensities (taking into account the depth of the plasma) and electron temperature distribution and the known transition probabilities of the lines, Boland et al, calculated the electron and ions densities. It was found that throughout the plasma, from the target surface up a distance z of 5mm, the electron temperature and density were related by the expression $T_e = 2 \times 10^{-11} n_e^{2/3}$ where T_e is in eV and n_e in cm^{-3} . This is consistent with an adiabatic expansion of an electron gas where the electron thermal energy is transferred to the ions during expansion.

1.2.3 Carbon Plasma Analysis.

Griffin and Schluter (1968) [23] carried on the analysis of the experiment of Boland et al and were able to show that the laser beam interacts directly with about 2.4×10^{17} carbon atoms in the polyethylene target. The experiment conducted by Boland *et al* had shown that the total number of ionised atoms in the plasma was $\sim 10^{16}$ (4% ionisation). The rest of the target material must have been present presumably in order to absorb the recoil from the plasma jet.

The main results of Boland's [21] paper are summarised in table 1.2, where the distribution of energy expressed as a percentage of the incident laser energy is given. In order to account for 100% of the incident radiation, it is necessary to conclude that almost 80% or more of the incident energy is converted to the kinetic energy of the ions.

Reflected and Transmitted (Griffin and Schluter 1968)	6-14%
Electron Thermal Energy	$\sim 2\%$
Ionisation Energy	$\sim 4\%$
Recoil Energy	15 - 3%
Ion Kinetic Energies	$\leq 80\%$

Table 1.2: Energy Distribution as percentage of Incident Laser Energy (Boland *et al*, [21])

Irons et al [13] made further spectroscopic studies of plasmas formed by 5J, 17ns ruby laser pulses focused on polyethylene targets. The spectrum of light emitted at right angles to the target normal, at different distances from the target surface and from the laser beam axis was studied with time resolution (figure 1.2). The spatial distributions of intensity of lines C I to C VI at different times were determined and also the line profiles in terms of the Doppler effect due to streaming velocities of the ions.

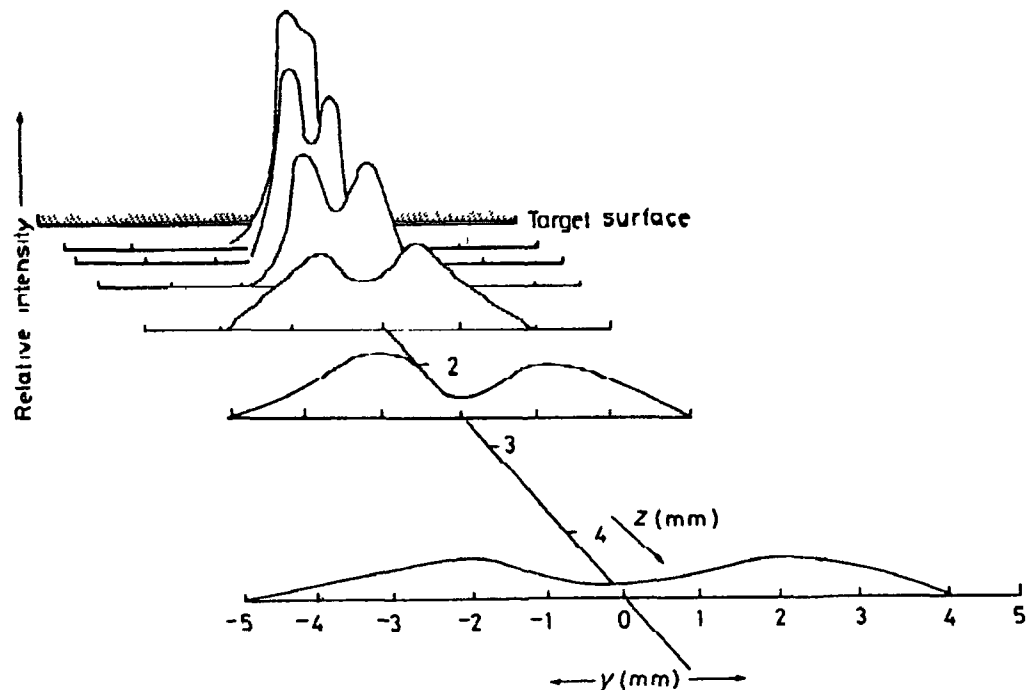


Figure 1.2: Spatial distribution of Intensity of CV 2271Å at $t=45\text{ns}$
after (Irons et al [13])

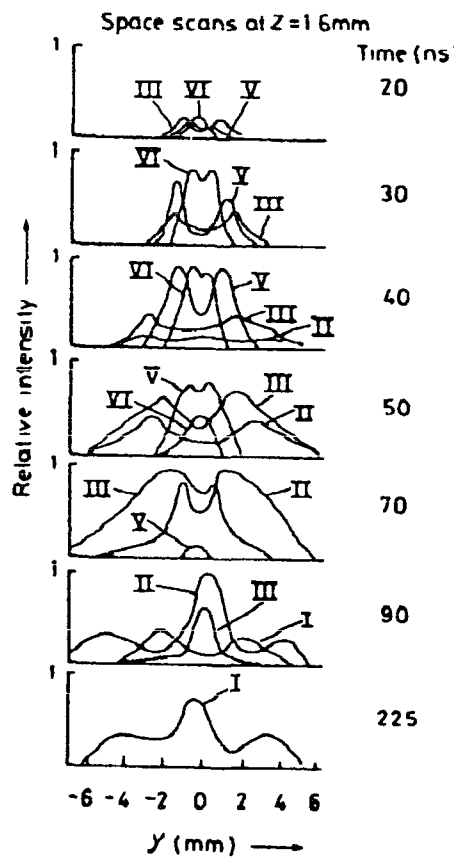


Figure 1.3: Sequence of spatial distributions for CI to CVI 1.6mm away from the target surface The maximum laser irradiance occurred at $t=20\text{ns}$ (Irons et al[13])

Figure 1 2 show the spatial distribution of the C V λ 2271 Å at $t = 45$ ns, while Figure 1 3 shows a sequence of intensity distributions in the same plane at different times for C I to C VI. In general, it was found that the various ion species tended to be separated in space, forming conical annular regions surrounding the laser beam axis, the most highly charged being on the axis. The mean radial velocity increased with distance from the axis. Within about 2mm of the target surface the electron and ion densities are very high, and first-order Stark broadening dominates the spectral line profiles of several Hydrogen-like C VI and quasi-like C V lines. At larger distances from the target (12mm) Doppler broadening dominated the much narrower line profiles.

1.3 Theory of the Concave Diffraction Grating.

1.3.1 Introduction

The concave diffraction grating was originally developed by H. A. Rowland in 1882. He recognised that VUV light could be dispersed and focused, when a concave grating was placed tangentially on a circle of diameter R , equal to the radius of curvature (R) of the grating. If the grating centre lies on the circumference of the circle, the spectrum from the entrance slit lying on the circle will also be focused onto this circle.

Grating (Radius of Curvature R , Diameter $2R$)

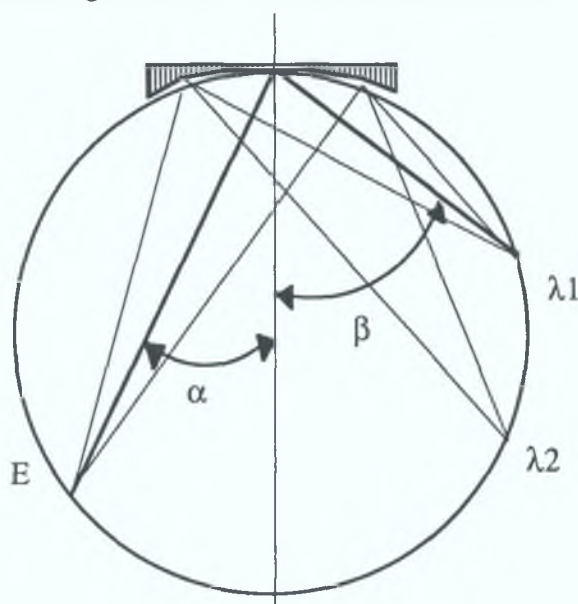


Figure 1.4: Rowland Circle Mount:

Radiation from the source is dispersed and focused by the grating at λ_1 , λ_2 , etc.
 α and β are the angles of incidence and diffraction with $\lambda_1 < \lambda_2$.

Since Rowland's early treatment there have been numerous contributions made to the theory of the concave grating mainly by Namioka [24-25] and Beutler [26]. The general theory which follows is taken substantially from Samson [27].

1.3.2 General Theory

A Cartesian co-ordinate system is set up with the origin O at the centre of the ruled grating (Figure 1.5). The x -axis is the grating normal with the z -axis parallel to the grating rulings. Let the points $A(x,y,z)$, $B(x',y',z')$, and $P(u,w,l)$ correspond to, an

illuminated point on the entrance slit, a focal point at the exit slit and any point on the grating rulings. The co-ordinates u, w, l are used only for points on the grating and w has only discrete values i.e., ratio of w/d is an integer (points on the ruled grating), where d is the groove separation in metres.

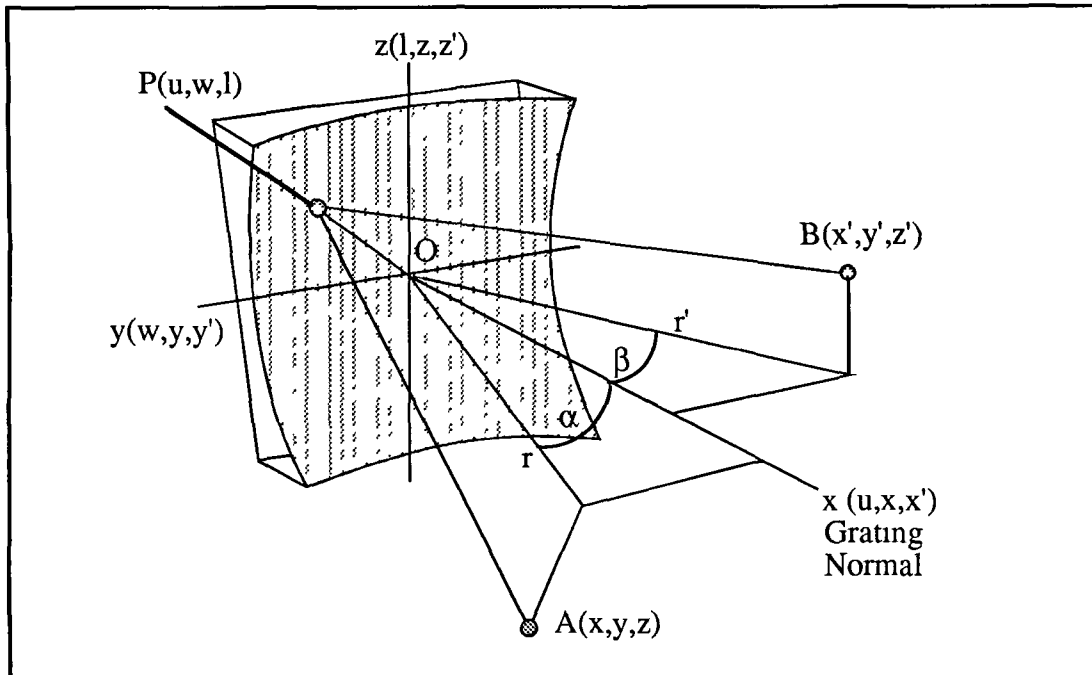


Figure 1.5: Image Formation by a Concave Grating

For the ideal case, in order that any two rays diffracted from the grating rulings, to reinforce at B , their path difference must equal an integral number of wavelengths. For two grooves separated a distance w apart, the corresponding path difference is $m\lambda w/d$ where d = constant groove separation, m is the spectral order ($=1,2,3$) and λ is the wavelength of the incident light. If a ray from the point A is to be focused at B , its path APB , where P is any point on the grating surface, must satisfy the optical path function F , given by

$$F = |AP| + |BP| + \frac{m\lambda w}{d}, \quad (1.11)$$

where

$$(AP)^2 = (x - u)^2 + (y - w)^2 + (z - l)^2 \quad (1.11a)$$

and

$$(BP)^2 = (x' - u)^2 + (y' - w)^2 + (z' - l)^2 \quad (1.11b)$$

The optical path function F represents the permissible path lengths of the various light paths from A to B as the point P wanders over the ruled surface of the grating. The origin of the co-ordinate system is a point on the spherical surface of the grating of radius R , thus all points P on the grating lie on a sphere so that

$$(u - R)^2 + w^2 + l^2 = R^2 \quad (1.12)$$

Solving for the roots of this quadratic equation yields

$$u = R \pm \sqrt{R^2 - (w^2 + l^2)} \quad (1.13)$$

Only the minus sign is significant in this application, since the positive sign of the radical applies to the opposite end of the diameter (not present in this case)

Introducing cylindrical co-ordinates (Figure 1.5),

$$x = r\cos\alpha, \quad x' = r'\cos\beta \quad (1.14)$$

$$y = r\sin\alpha, \quad y' = r'\sin\beta \quad (1.15)$$

where α and β are the angles of incidence and diffraction respectively measured in the xy plane, and the signs of α and β are opposite if A and B lie on different sides of the xz plane (grating normal)

Substitution of cylindrical co-ordinate equations (1.14) and (1.15) and equation (1.13) (u expanded as power series) into expression for $(AP)^2$ and $(BP)^2$ yield the following solutions

$$\begin{aligned} AP &= F_1 + F_2 + F_3 + \\ BP &= F'_1 + F'_2 + F'_3 + \end{aligned}$$

The terms for AP and BP are tabulated separately for clarity (see below). In general the values of F_n and F'_n decreases rapidly with order n . Each term has physical significance with regard to image formation and optical aberrations. Terms greater than F_3 can generally be neglected so that the optical path function can be written as

$$F = F_1 + F'_1 + F_2 + F'_2 + F_3 + F'_3 + \frac{m\lambda w}{d} \quad (1.16)$$

$$\text{where } F_1 = r - w\sin\alpha \quad (1.16a)$$

$$\begin{aligned} F_2 &= \frac{1}{2}w^2 \left(\frac{\cos^2\alpha}{r} - \frac{\cos\alpha}{R} \right) + \frac{1}{2}w^3 \frac{\sin\alpha}{r} \left(\frac{\cos^2\alpha}{r} - \frac{\cos\alpha}{R} \right) \\ &\quad + \frac{1}{2}w^4 \frac{\sin\alpha}{r} \left(\frac{\cos^2\alpha}{r} - \frac{\cos\alpha}{R} \right) \end{aligned} \quad (1.16b)$$

$$F_3 = \frac{1}{2}l^2 \left(\frac{1}{r} - \frac{\cos\alpha}{R} \right) - l \frac{z}{r} + \frac{z^2}{2r} \quad (1.16c)$$

$$F_1 = r' - w \sin \beta \quad (1.16d)$$

$$\begin{aligned} F'_2 &= \frac{w^2}{2} \left(\frac{\cos^2 \beta}{r'} - \frac{\cos \beta}{R} \right) + \frac{w^3}{2} \frac{\sin \beta}{r'} \left(\frac{\cos^2 \beta}{r'} - \frac{\cos \beta}{R} \right) \\ &\quad + \frac{1}{2} w^4 \frac{\sin \beta}{r'} \left(\frac{\cos^2 \beta}{r'} - \frac{\cos \beta}{R} \right) \end{aligned} \quad (1.16e)$$

$$F'_3 = \frac{1}{2} l^2 \left(\frac{1}{r'} - \frac{\cos \beta}{R} \right) - l \frac{z}{r'} + \frac{z^2}{2r'} \quad (1.16f)$$

The decreasing orders of magnitude of the successive expressions is demonstrated from the fact that they contain successively higher inverse powers of R, r and r', which are usually large compared to the grating width w and length l. The terms $(F_1 + F'_1)$ and $(F_2 + F'_2)$ embody the condition for image formation for both plane and concave gratings, while the $(F_3 + F'_3)$ term describes the astigmatism of the grating. Astigmatism results in a point source being imaged as a vertical line, i.e. only partial focusing in the vertical plane of the Rowland circle. The dependence of $F_3 + F'_3$ on α and β implies that the effect of astigmatism is greatest at grazing incidence, decreasing proportionally as one moves to normal incidence operation.

1.3.3 Grating Equation

To get the focusing conditions from any section of grating surface, we invoke Fermat's Principle of Least Time. According to Fermat's principle, the point B is located so that F will be an extremum for any point P on the grating surface, namely

$$\frac{\delta F}{\delta w} = 0 \quad (1.17)$$

$$\frac{\delta F}{\delta l} = 0 \quad (1.18)$$

Thus to obtain a focus from the horizontal section of the grating, the partial derivative of F with respect to w ($\delta F / \delta w$) must be zero. Similarly, the focus from a vertical section of the grating requires that $\delta F / \delta l = 0$. Non-zero values indicate that light is not directed towards B and the image formation is not perfect.

To obtain the grating equation we first isolate and identify the first two terms of equation (1.16)

$$F = F_1 + F'_1 + \frac{m\lambda w}{d}, \quad (1.19)$$

Introducing the terms (1 16a) and (1 16d), the optical path function becomes

$$F = r + r' - w(\sin \alpha + \sin \beta) + \frac{m\lambda w}{d}, \quad (1.20)$$

Applying Fermat's principle ($\delta F / \delta w = 0$) yields the Grating Equation

$$\pm m\lambda = d(\sin \alpha + \sin \beta) \quad (1.21)$$

where the positive sign applies to inside orders and the negative sign applies to outside orders. α and β are opposite when they lie on opposite sides of the grating normal. For the Normal Incidence spectrometer which forms the basis of this thesis, the inside spectrum is observed and hence the grating equation is

$$m\lambda = d(\sin \alpha - \sin \beta) \quad (1.22)$$

From the above equation it can be shown that a grating blazed for 800\AA in first order ($m=1$) will also be blazed for 400\AA in second order ($m=2$) (see section 1.2.6). This is the case for the Acton 1m normal incidence spectrometer, where many spectral lines of carbon were observed up to fourth/fifth order (see Chapter 3).

1.3.4 Dispersion

The dispersion of a grating expresses how the various wavelengths are distributed along the Rowland circle. Angular dispersion specifies the dispersion of the various wavelengths as a function of diffracted angle and is defined as $d\beta/d\lambda$. By differentiating the grating equation (1.22), for a fixed angle of incidence, this quantity is numerically defined as

$$\frac{d\beta}{d\lambda} = \frac{m}{d \cos \beta} \quad (1.23)$$

The Reciprocal Linear Dispersion ($dl/d\lambda$) defines the extent to which a spectral interval is spread out across the focal surface of the spectrometer and is expressed in nm/mm, $\text{\AA}/\text{mm}$ etc. Linear dispersion is associated with an instrument's ability to resolve fine spectral detail. If the reciprocal dispersion is re-written in terms of $\Delta\beta$

$$\frac{\Delta\lambda}{\Delta l} = \frac{\Delta\lambda}{\Delta\beta} \frac{\Delta\beta}{\Delta l} \quad (1.24)$$

and substituting $\Delta l / R$ for $\Delta \beta$ (Samson), eqn (1.24) becomes

$$\frac{\Delta \lambda}{\Delta l} = \frac{\cos \beta}{mR(1/d)} \cdot 10^4 \text{ \AA / mm}, \quad (1.25)$$

where R measured in meters and $(1/d)$ is the number of grooves per mm. From this equation we see that the dispersion increases for higher orders, for larger focal lengths and for increased numbers of ruled lines per mm.

The above dispersion equations in their present form are inadequate for describing the VM-521 spectrometer since they assume a fixed angle of incidence. In most normal incidence monochromators the location of the exit and entrance slits are fixed and the grating rotates through an angle φ , about an axis through the centre of its face (See section 1.3). D_v (Figure 1.6) (referred to as the deviation angle) is the angle between the two arms of the spectrometer and is therefore given by $D_v = \alpha - \beta (= 15^\circ$ in our case).

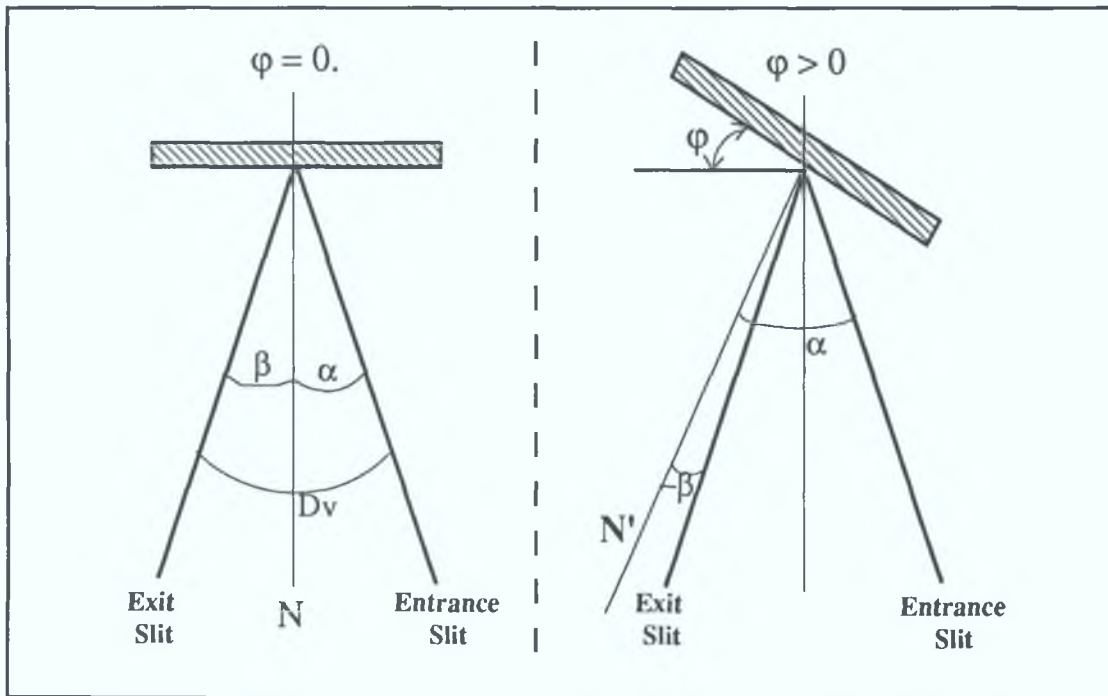


Figure 1.6: For $\varphi=0$, $\alpha=\beta=7.5^\circ$ and for $\varphi>0$, $\beta=\alpha-2\varphi$.

N and N' are the grating normal at $\varphi=0$ and $\varphi>0$.

A dispersion equation ($\delta\lambda_\varphi/\delta l$) has been derived, which expresses the linear dispersion of the various wavelengths along the Rowland circle as a function of grating angle. The grating equation (1.21) is rewritten with α and β replaced with the composition of their angle, i.e. $\alpha = 7.5^\circ + \varphi$, $\beta = 7.5^\circ - \varphi$, where 7.5° is the zero order angle and φ is the rotation angle of the grating.

The grating equation now reads

$$m\lambda = d[\sin 75 \cos \varphi + \cos 75 \sin \varphi - \sin 75 \cos \varphi + \cos 75 \sin \varphi], \quad (126)$$

and by collecting terms

$$m\lambda = 2d \cos\left(\frac{D_v}{2}\right) \sin \varphi. \quad (127)$$

The linear dispersion is rewritten in terms of $\delta\varphi$ and so

$$\frac{\delta\lambda}{\delta l} = \frac{\delta\lambda}{\delta\varphi} \frac{\delta\varphi}{\delta l}, \quad (128)$$

where

$$\frac{\delta\lambda}{\delta\varphi} = \frac{2d \cos 75 \cos \varphi}{m}, \quad (129)$$

$$\frac{\delta\varphi}{\delta l} = \frac{\delta\varphi}{\delta\beta} \frac{\delta\beta}{\delta l} = \frac{1}{2} \frac{\delta\beta}{\delta l} = \frac{1}{2R} \quad (130)$$

Equation (130) is correct since a change in φ of one degree results in a difference of 2° between the incident and diffracted angles

Hence the reciprocal linear dispersion as a function of grating angle becomes

$$\frac{\delta\lambda_\varphi}{\delta l} = \frac{d \cos 75 \cos \varphi}{mR} \quad (131)$$

The computed dispersion (nm/mm) is shown in figure 17

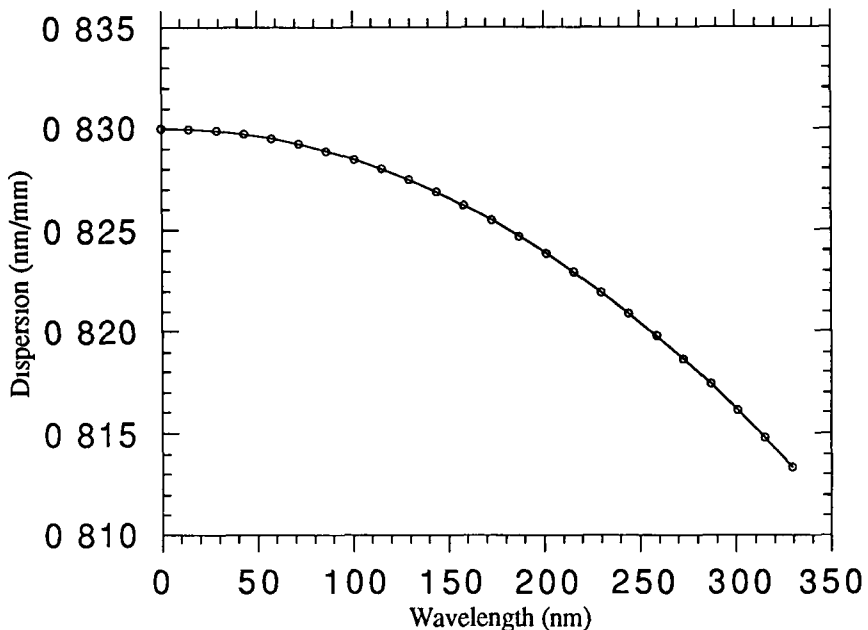


Figure 1.7: Plot of Dispersion Versus Wavelength for Acton 1m

The value of 0.829nm/mm at a wavelength of 80nm is in very good agreement with the measured value of 0.83nm/mm given by the manufacturer

1.3.5 Resolving Power

Dispersion and resolving power are two closely related quantities , dispersion determines the separation of two wavelengths whereas resolving power determines whether this separation is distinguishable When a monochromatic beam is diffracted by a grating, it forms a pattern of principal and secondary maxima The principal maxima are represented by the order number m Secondary maxima intensities decrease as the number of ruled lines N exposed to the incident radiation increases The angular half-width $\Delta\beta$ of the principal maximum is the angular distance between the principal maximum and its first minimum For a plane grating this quantity is given by

$$\Delta\beta = \frac{\lambda}{Nd \cos \beta} \quad (1.32)$$

and this width sets the theoretical limit of the resolving power of the grating

The resolving power P is a theoretical concept and is defined as

$$P = \frac{\lambda}{\Delta\lambda}, \quad (\text{dimensionless}) \quad (1.33)$$

where $\Delta\lambda$ is the minimum resolvable separation between two spectral lines of equal intensity. This minimum separation can be found from Rayleigh's criterion. This criterion however has been modified by Namioka [24] so that it is not required that the maximum of one line to fall on the minimum of the other. However the ratio of minimum intensity of combined structure to that of either maximum must remain at $8/\pi^2$ ($= 0.8106$).

Expressing $\Delta\lambda$ in terms of $\Delta\beta$

$$\Delta\lambda = \Delta\beta \frac{d\lambda}{d\beta} \quad (1.34)$$

and using equations (41) and (42), it can be shown that

$$P = \frac{\lambda}{\Delta\lambda} = mN \quad (1.35)$$

where N is the number of grooves exposed to the incident radiation and m is the order number.

The alternative form chosen by Namioka [24] may also be used

$$P = \frac{Wm}{d} \quad (1.36)$$

where W is the exposed grating width (in m) of the grating

The resolution reaches a maximum R_{opt} at a width $W = W_{opt}$, an expression for which may be derived from analysis of the F_3 terms Namioka [25] of the optical path function

$$W_{opt} = 2.38[R^3\lambda \frac{\cos\alpha\cos\beta}{(\sin^2\alpha\cos\beta + \sin^2\beta\cos\alpha)}]^{1/4} \quad (1.37)$$

This expression determines the width of the grating which should be illuminated in order to optimise the resolving power of the system. A plot of W_{opt} for the Acton 1m is shown in Figure 1.8

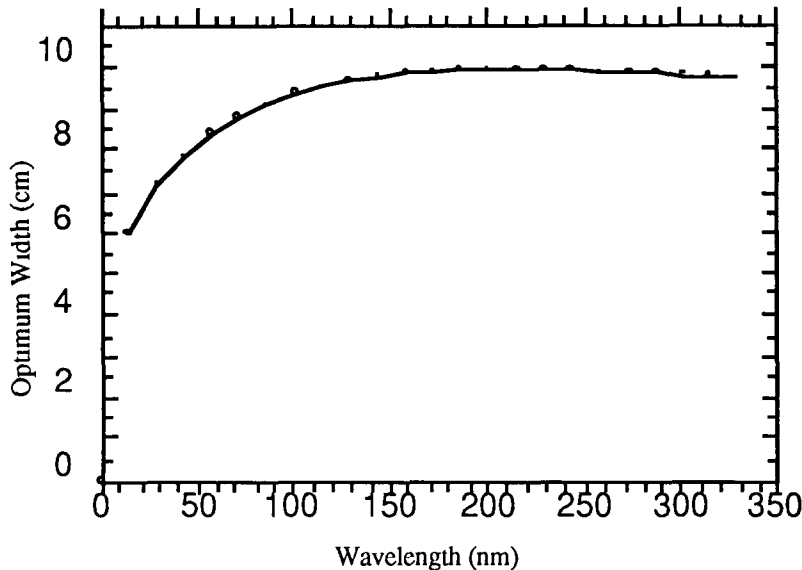


Figure 1.8: Optimum width of grating as function of wavelength for Acton 1m

This optimum resolving power P_{opt} as a function of grating width exposed is shown in the following table

Width of Grating W	Resolving Power	
		P
$W \leq 0.85W_{\text{opt}}$		$W(m/d)$
$W = W_{\text{opt}}$		$0.92W_{\text{opt}}(m/d)$
$W \gg W_{\text{opt}}$		$0.75W_{\text{opt}}(m/d)$

Table 1.3: Resolving Power of Concave grating
as function of Grating Width (Samson[27])

1.3.6 Grating Efficiency

The efficiency of a grating at a given wavelength can be defined as the percentage of incident radiant flux returned by a grating into a given spectral order. R. W. Wood in 1910 constructed the first grating ruled with grooves of controlled shape. Blazed gratings are manufactured to produce maximum efficiency at designated wavelengths. The grating used in the Acton VM-521 is blazed at 80nm in first order. The groove shape controls the amount of radiation concentrated into a given spectral order. The groove separation determines the angular separation of the diffracted beam (equation 1.32). Figure 1.9 shows a cross-section of a typical blazed grating.

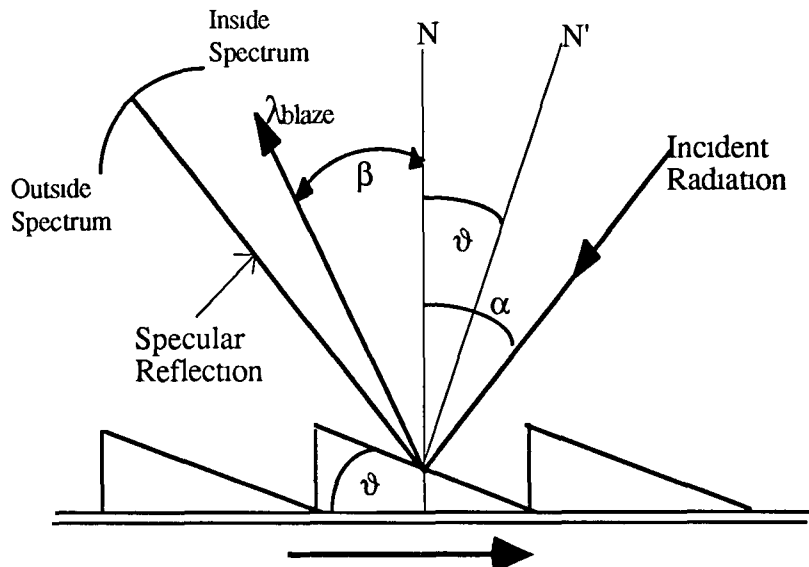


Figure 1.9: Cross section of a blazed grating ϑ is the blaze angle

N is the normal to the main grating surface, while N' denotes the normal to the groove facets. The grooves are cut such that the facets make an angle ϑ with grating surface. Concentrating radiant energy at a particular wavelength is based on the principle that the wavelength is diffracted at the same angle as the specularly reflected beam from the groove facets. Hence

$$\alpha - \vartheta = \beta + \vartheta, \\ \therefore \vartheta = \frac{\alpha - \beta}{2} \quad (1.38)$$

However from figure 1.6 (inside spectrum, α, β on opposite sides of normal),

$$m\lambda = d (\sin \alpha - \sin \beta) \quad (1.39)$$

Eliminating β from (1.38) and (1.39), we obtain the wavelength for which the grating is blazed (as a function of incident angle),

$$m\lambda_{blaze} = d \sin 2\vartheta \cos(\alpha - \vartheta) \quad (1.40)$$

So for an incident angle $\alpha = 10.25^\circ$, a blaze angle $\vartheta = 2.75^\circ$ and an intergroove spacing $d = 8.333 \times 10^{-7}$, the blaze wavelength is $79.23\text{nm} \approx 80\text{nm}$

A grating blazed in the first order ($m=1$) is equally blazed in the higher orders, and the maximum grating efficiency for each of the subsequent higher orders decreases as the spectral order m increases.

1.4 The Normal Incidence Spectrometer Mount

1.4.1 Introduction.

There are many types of concave grating spectrometers available today, each with their own particular advantages and disadvantages. Spectrometers are usually referred to by the size of the grating and the type of mount. The Acton VM-521 1m Normal Incidence spectrometer therefore, employs a grating with a radius of curvature R of 1m and with an angle of incidence close to zero (7.5°). For angles of incidence less than 10° , the radiation is considered to be at normal incidence. At these angles, there is little astigmatism or variation in grating efficiency.

The basic principle of a concave grating spectrometer lies in the focusing properties of the concave diffraction grating. As described in section 1.2, the diffracted images of the source slit are sharply focused onto the exit slit, which is on the Rowland circle. Absolute values of the output wavelengths are determined from the equations

$$m\lambda = 2d\cos\left(\frac{D_v}{2}\right)\sin\varphi \quad (143)$$

$$\frac{d\lambda}{dl} = \frac{d \cos 7.5 \cos \varphi}{mR} \quad (144)$$

where m is the order number, D_v is the Deviation angle = 15° , φ is the grating angle, R is the grating focus, d is the number of grooves per mm

The Normal Incidence configuration was developed independently by a number of groups including Vodar [28], Robin [29] and McPherson Corporation [30].

1.4.2 General Theory

The basic principle of the Normal Incidence Spectrometer is as follows. The concave grating is rotated about a vertical axis, tangent to the centre of the grating. The grating is constrained to move along the bisector of the angle subtended by the entrance and exit slits. Rotation of the grating provides the monochromatic action of the spectrometer, while focusing is maintained by the linear motion of the grating.

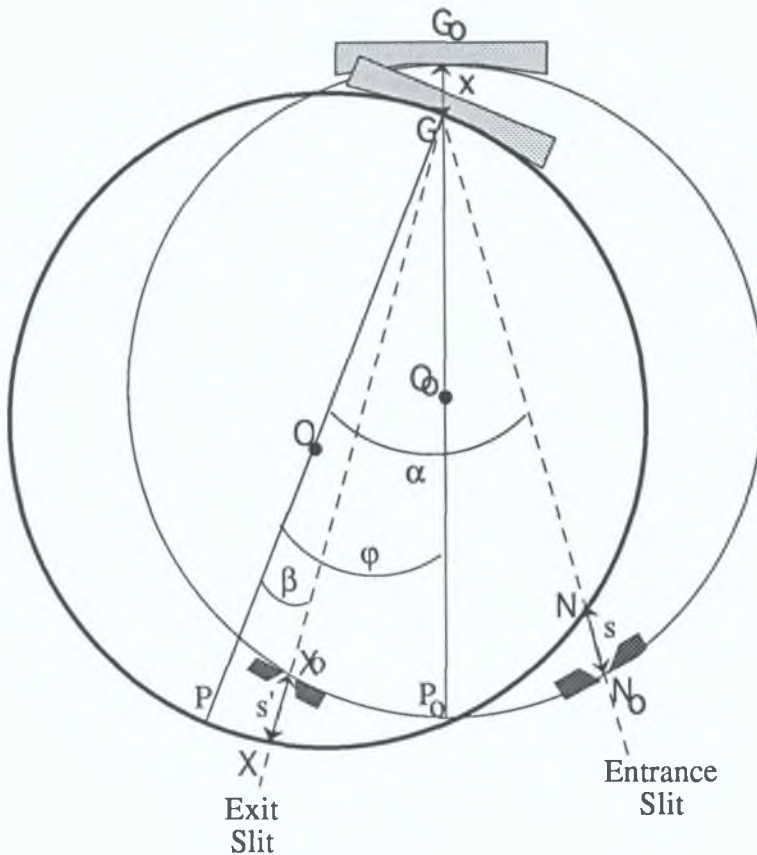


Figure 1.10: Rotation and Translation of the grating along the bisector of the angle subtended by the slits at the grating centre.

Returning to the discussion in section 1.2 , the expression for the grating equation gives no information on the focal conditions for the concave grating, since r and r' do not appear. However since R has a finite value for the grating, the second and higher terms of the function F have appreciable values, and their partial derivatives ($\delta F / \delta w = 0$) must be investigated and subjected to Fermat's condition. Considering the terms F_2 and F'_2 which have the largest values and applying Fermat's condition, $\delta(F_2 + F'_2) / \delta w = 0$ yields an expression which vanishes to zero if

$$\frac{\cos^2 \alpha}{r} - \frac{\cos \alpha}{R} + \frac{\cos^2 \beta}{r'} - \frac{\cos \beta}{R} = 0. \quad (1.45)$$

This expression is the fundamental focal condition of the grating and has solutions (for the case of the Rowland circle) of the form

$$r = R \cos \alpha \text{ and } r' = R \cos \beta. \quad (1.46)$$

These relations are the equations in polar co-ordinates of a circle of diameter R , on which the points r and r' lie. That is the light source and spectral lines are on the circle, to which

the grating is tangent, and which has a diameter equal to the radius of the grating blank. This circle is known as the "Rowland Circle". So r and r' correspond to the entrance and exit slit distances from the centre of the grating.

If the grating is now rotated and displaced so that, the entrance slit distance is decreased a distance s' from the Rowland circle, and if the exit slit is similarly increased by an amount s (figure 1.10) then the above equation becomes (after substitution for r and r')

$$\frac{\cos^2 \alpha}{s+R\cos\alpha} - \frac{\cos\alpha}{R} + \frac{\cos^2 \beta}{R\cos\beta-s'} - \frac{\cos\beta}{R} = 0 \quad (1.47)$$

Solving for s' yields

$$s' = s \left[1 + \frac{s}{R} \left(\frac{\cos\alpha + \cos\beta}{\cos\alpha\cos\beta} \right) \right]^{-1} \quad (1.48)$$

When

$$\frac{s}{R} \left(\frac{\cos\alpha + \cos\beta}{\cos\alpha\cos\beta} \right) \ll 1,$$

for ($R \gg s$) then $s \approx s'$, which is approximately the case for near normal incidence.

The grating G_O , entrance slit N_O , and exit slit X_O are initially all on the Rowland circle so that the focus falls on X_O (see figure 1.10). If the grating is then rotated through an angle ϕ and undergoes a linear motion through a distance x , the optical elements should now be at G, N and X respectively. The entrance focus is now situated a distance s outside the new Rowland circle, while the exit focus is situated a distance s' inside the circle. The distance is found by the construction $GN_O = GX_O$, which is equivalent to

$$R \cos \alpha - s' = R \cos \beta + s \quad (1.49)$$

Let α_O be the angle of incidence in the initial position. Then if the change in angle ϕ subtended by the slits at the grating is small over the spectral range scanned, equation (1.49) becomes, for $s=s'$,

$$s = R \cos \alpha_O \sin \phi \quad (1.50)$$

An approximation for the linear motion x of the grating, is noted from Figure 1.10,

$$G_O G + GP_O = R, \quad (1.51a)$$

and

$$x + RCos\phi = R, \quad (1.51b)$$

which becomes

$$x = R (1 - \cos \varphi) \quad (152)$$

This relationship gives the linear motion of the grating and is valid for φ small (i.e. $s \approx s'$) and if the grating is pivoted about P_0 , the intersection point of the grating normal with the Rowland circle in its initial position. The grating distance x is plotted as a function of grating angle in figure 111a and the grating angle as a function of wavelength is shown in figure 111b.

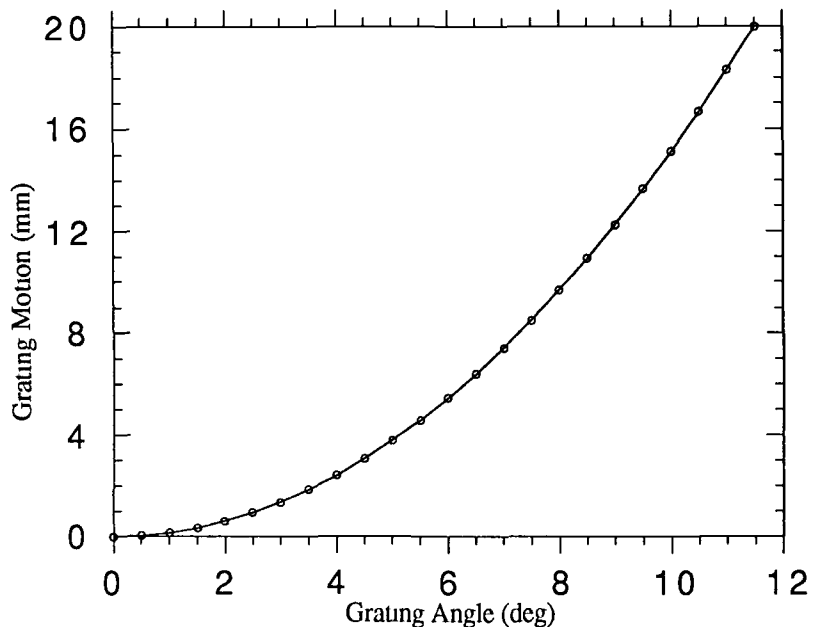


Figure 1.11a: Plot of grating motion (x) vs grating angle (ϕ) in the range 0° - 12°

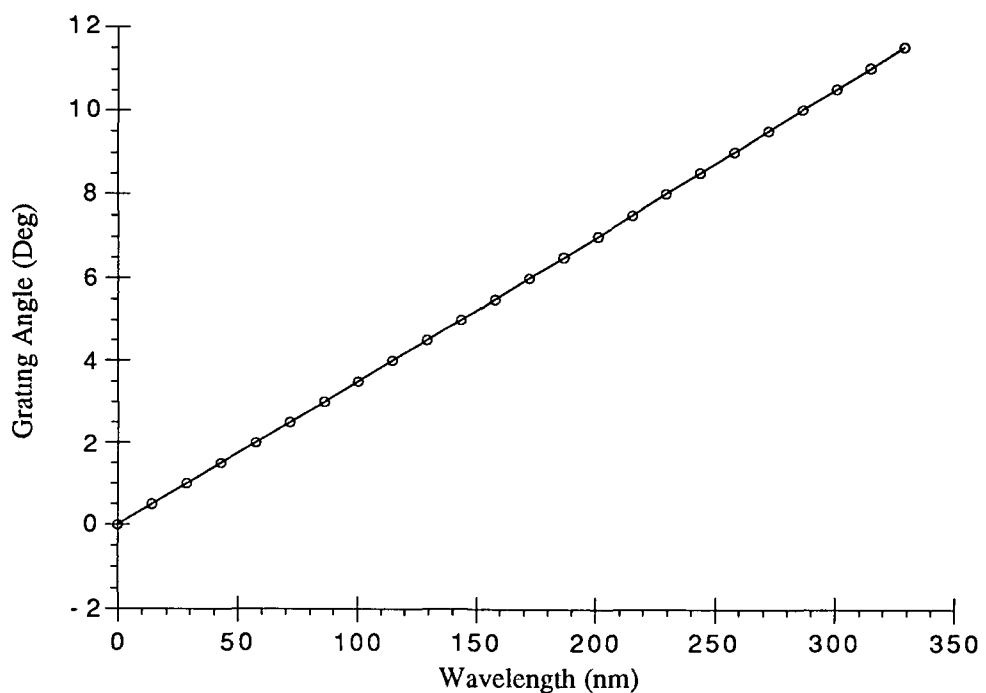


Figure 1.11b: Plot of Grating Angle (ϕ) Vs Wavelength (λ).

Chapter 2

Development and Testing of the Acton 1m Normal Incidence Multi-Channel Spectrometer.

2.0 Introduction

The main aim of this chapter is to describe in detail the individual system components which comprise the Acton 1m normal incidence multichannel spectrometer facility

The system comprises an Acton VM-521 one meter Normal Incidence Spectrometer operating between 30 and 325 nm. A vacuum target chamber is mounted on the entrance arm and an optical detection system is attached to the exit arm of the spectrometer. This optical system comprises of

- Galileo Electro-Optics Corporation VUV-25R Micro-Channel Plate
- EG&G Princeton Applied Research Model 1453A, 1024 Pixel, Silicon Photodiode Array (PDA) Detector
- EG&G Princeton Applied Research Model 1471A, Optical Multi-Channel Analyser (OMA) Detector Interface

This chapter includes

- Description of the Acton Normal Incidence Spectrometer
- Introduction to the Galileo Micro-Channel Plate (MCP)
- Introduction to the EG&G Optical Multi-Channel Analyser (OMA)
- Outline of Nd YAG laser used to produce the plasmas under study
- Target chamber design and vacuum coupling to the Acton VM-521
- Modifications to the exit arm housing on the spectrometer in order to facilitate the mounting the VUV optical multichannel detection system
- Outline of the OmaSoft program used to control the laser plasma experiment

2.1 The Acton 1m Spectrometer.

The Acton Research Corporation (ARC) VM-521 is a 1 meter normal incidence monochromator employing a precision scanning mechanism which provides a user selected wavelength (30 - 325nm) via an electronic controller. The cam-controlled translation motion of the 1200g/mm concave grating changes the output wavelength while maintaining good focus at the exit slit.

It was necessary to replace the original exit arm housing on the instrument in order to mount the multi-channel optical detection system. The housing was replaced with a custom adapter flange which was manufactured in-house. Further modifications allowed for the attachment of the photodiode array readout system via four supporting arms. A specially designed target chamber was coupled to the entrance slit housing of the spectrometer via standard vacuum flanges. A discussion of the elements which make up the Acton VM-521 is now presented.

2.1.1 General specification.

The spectrometer is manufactured from 304 stainless steel plate and is internally welded vacuum tight to a leak rate of 4×10^{-10} cm³ of helium/sec. The entrance and exit arms are mounted with a deviation angle (D_V) of 15 degrees. The spectrometer dimensions are shown in the figure 2.1

2.1.2 Entrance Slit Assembly.

The entrance slit assembly provides bilaterally adjustable slit width and vertical height baffles. The slit width is adjustable from 5 to 3000 microns by a micrometer knob located on the slit housing with an accuracy of 10 microns. An arrangement of standard and custom flanges have been used to mount a target chamber to the entrance slit. The target chamber mounting incorporates a glass capillary array (GCA) which prevents plasma blow-off reaching the entrance slits. (See section 2.5)

2.1.3 Exit Slit Assembly.

The exit slit assembly has been replaced with a custom flange, to mount the multichannel detector system. The custom flange positions the Galileo MCP at the focal point of the concave grating. A full description of the custom flange is provided in section 2.6

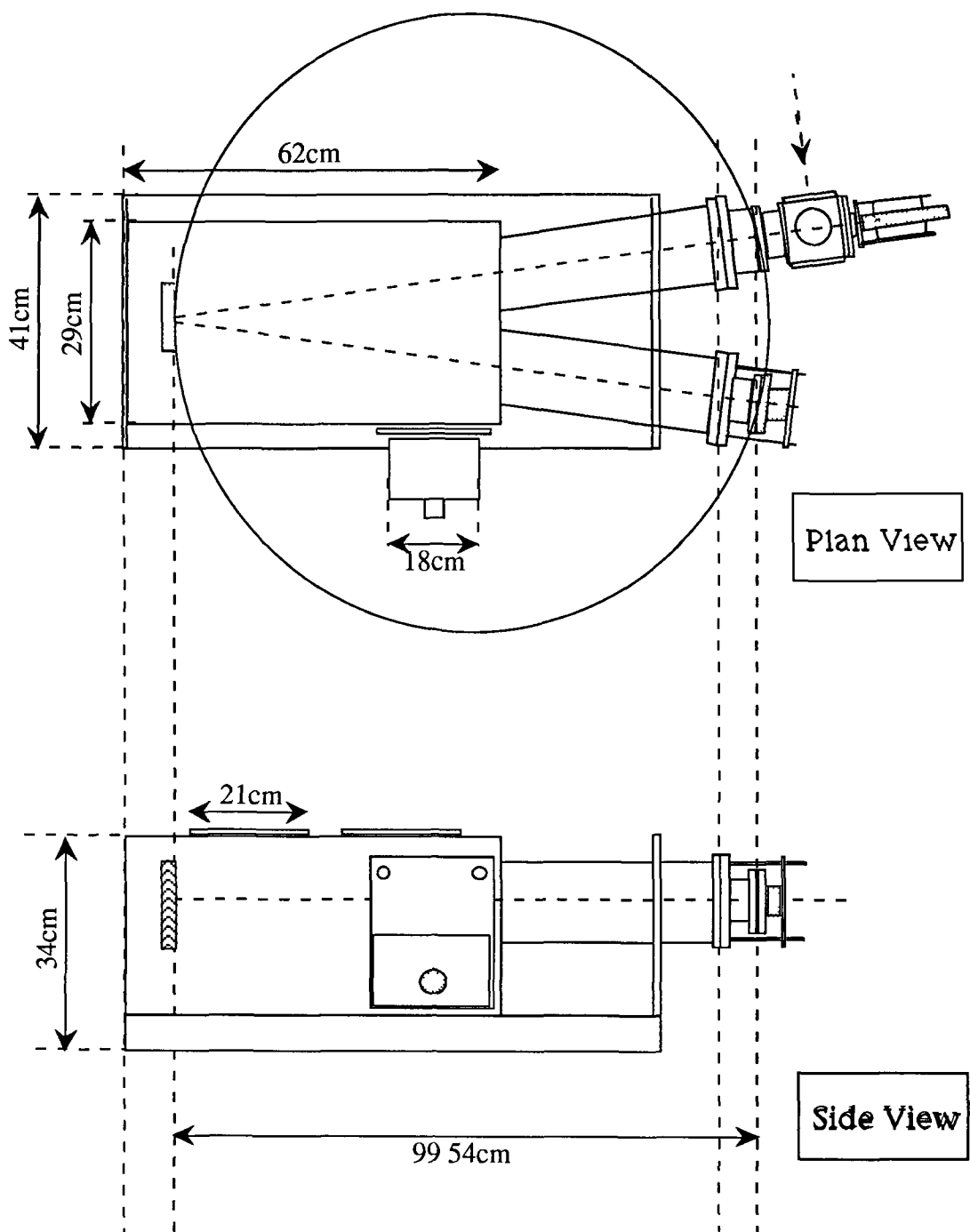


Figure 2.1: Acton VM-521 Schematic

2.1.4 Bausch & Lomb Concave Grating

The 1200 grooves/mm concave grating is coated with Al+MgF₂ for improved VUV efficiency A kinematic mount for the grating holder allows the assembly to be interchanged without re-alignment or adjustment after the initial alignment of the instrument External focusing of the exit slit, at both zero and high wavelengths are made possible by two micrometer screw adjustments The optical characteristics of the grating as specified by the manufacturer are

Blaze Angle	2 75°
Blaze Wavelength.	800Å
Ruled Width	96mm
Ruled Height	56mm

2.1.5 SpectraDrive Controller

The output wavelength is indicated to an accuracy of 0.01nm by both a precision four digit mechanical counter and the SpectraDrive controller readout display The model 748 SpectraDrive controls the wavelength scanning operations of the grating This scanning system provides a maximum scanning speed of 1000 Å/min One revolution of the stepping motor changes the output wavelength by 10 Å with a 1200g/mm grating

2.1.6 Vacuum specifications

An 8" conflat type flange is provided at the base of the instrument for connection to the Balzers 170 l/s Turbo-molecular pump via a zero-length flange adapter A KF-40 type fitting at the instrument base also provides for a cold-cathode gauge head attachment The spectrometer was evacuated to a pressure of $\approx 5 \times 10^{-7}$ mbar during which time all testing and calibration took place This figure was subsequently improved to 5×10^{-8} mbar by replacement of a defective vacuum drive bellows

2.2

The Galileo Channel Electron Multiplier Array (CEMA)

The Galileo CEMA consists of a single stage micro channel plate (MCP) proximity focused by an electric field onto a phosphor deposited on a coherent fibre optic imaging conduit

2.2.1 Introduction to MCP's

An MCP is a compact detector of energetic photons and charged particles. The amplified input signal is typically outputted to a single anode or phosphor screen deposited on a fibre-optic substrate. Originally developed by the US military for image intensification, the Micro-Channel plate has found applications in X-ray & VUV detection, electron-beam fusion studies and nuclear science. The MCP is ideal for these types of applications because of its superior time resolution characteristics, dynamic range, linear response, sensitivity and gain.

An MCP is constructed from a bundle of specially formulated lead glass tubes with solid cores, which are drawn and fused to form an array. This fused array is then sliced into wafers at a bias angle and then polished to an optical finish. The individual wafers are then chemically treated to remove the solid core leaving a uniform porous structure of $10^4\text{-}10^7$ micro-channels. Each microchannel functions as a *channel electron multiplier*, relatively independent of adjacent channels. Through further processing of the microchannel plate walls, a silicon dioxide-rich, secondary electron emissive layer is formed on the electrically semi-conductive layer. Finally, a thin metal electrode is vacuum deposited on both input and output surfaces to electrically connect all channels in parallel.

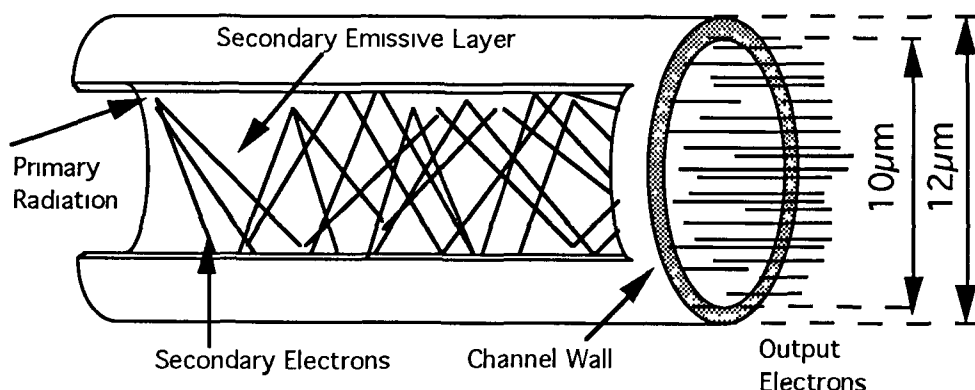


Figure 2.2: Diagram of a single MCP Channel

2.2.2 Mode of operation.

When a photon or charged particle is incident on the input face of a channel, secondary electrons are generated and accelerated down the channel towards the output face. Each time an electron strikes the channel wall, additional secondary electrons are generated. This process continues along the length of the channel yielding up to 10^4 electrons at the output surface. For normal operation, a bias of up to 1000 volts is applied across the MCP faces. The resulting bias current flowing through the semi-conducting layers, supplies the electrons necessary to continue the avalanche multiplication process. The emerging electrons are then accelerated across a vacuum gap by a positive potential of typically +4kV and then proximity focused onto a phosphor coated fibre optic bundle. Acceleration of the electron bunches from the MCP to energies of ~4kV results in further optical gain. The coherent electron image is converted to an optical image which can then be readout by a visible light-sensitive array detector.

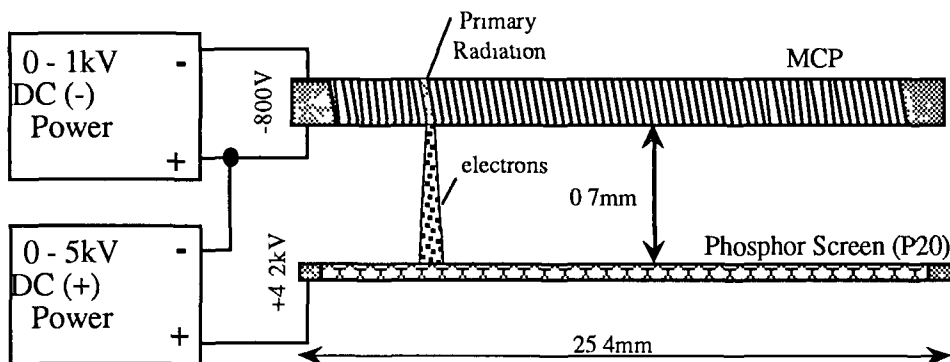


Figure 2.3: Operating schematic of 6025-FM CEMA

2.2.3 Characteristics.

The MCP used with the 1m spectrometer is a Galileo Electro-Optics Corporation 6025-FM. The spatial resolution of this detector given by the manufacturer is 42 lp/mm (Nyquist limit = (0.5 / centre-centre spacing(12 μm)). The active area of the matrix is 4.9 cm², with an open area ratio of 55% and presents approximately 25mm spectral coverage at the exit slit of the spectrometer. The channel axes are biased at an angle of 12° to the surface normal which prevents ion feedback within the channels. Ions are produced by electron collisions with gas molecules desorbed from the channel walls under electron bombardment. In straight channel multipliers these ions drift back to the channel input producing additional secondary electrons at the photocathode and result in a regenerative feedback avalanche effect.

The gain produced by an MCP is given by

$$G = \left(\frac{AV}{2\alpha V_0^{1/2}} \right)^{\frac{4V_0\alpha^2}{V}} \quad (21)$$

where V is the total channel voltage, V_0 is the initial energy of the emitted secondary electron $\sim 1\text{eV}$, α is the length to diameter ratio l/d (typically in the range 40-60), A is a proportionality constant ~ 0.4

For the 6025-FM, the gain specified by the manufacturer is 3.3×10^4 at the maximum operating voltage of 1kV. The vacuum flange mounted detector is fitted with one BSHV vacuum feedthrough rated at 7.5kV and three MHV vacuum feedthroughs rated at 5kV. The MCP operates in the photon/negative particle detection mode (1e negative across MCP face and positive across the gap)

The limiting resolution of the CEMA is dependent on (1) the spread of the electron bunch as it travels from the output face to the phosphor screen and (2) the amount of shear distortion in the fibre-optic conduit caused when the fibre bundles are fused together during manufacture

The dependence of the diameter (d) of the electron-bunch spot size on the phosphor to the CEMA-phosphor voltage (V_{ph}) and gap distance (s) is given approximately by (Cromer et al) [31]

$$d(\mu\text{m}) = \frac{s(\mu\text{m})}{\sqrt{V_{ph}}} \quad (22)$$

Thus, the optimum resolution is achieved by having the smallest value of s while still maintaining a breakdown free gap voltage of $\sim 4\text{kV}$ to provide adequate phosphor gain. Hence for a gap size of 1.2mm (as specified by Galileo) the spot diameter is 19 μm which is less than one PDA pixel width (25 μm). It should be noted that shear stresses in the fibre-optic stub can result in image distortions significantly greater than this [31] and hence provide the greater contribution to image degradation

2.3

The EG&G Optical Multi-Channel Analyser System.

The OMA system comprises of a model 1453A photodiode detector camera head, a model 1471A Detector Interface, a custom written software program called 'OmaSoft' and a PC. A complete system specification is included in Appendix C.

2.3.1 Model 1453A Detector.

The EG&G Model 1453A is an un-intensified detector, based on the 1024 element EG&G Reticon linear photodiode array (PDA) with a wavelength sensitivity range of 300 to 1100nm. The photodiode array package contains 1024 photodiodes, a pair of two-phase MOS shift registers, and a field effect transistor (FET) switch for each diode (See figure 2.4). The individual photodiodes are 25 μ m wide by 2.5mm high and extend over 25mm. A centre to centre spacing of 25 μ m results in a Nyquist spatial frequency of (20 lp/mm).

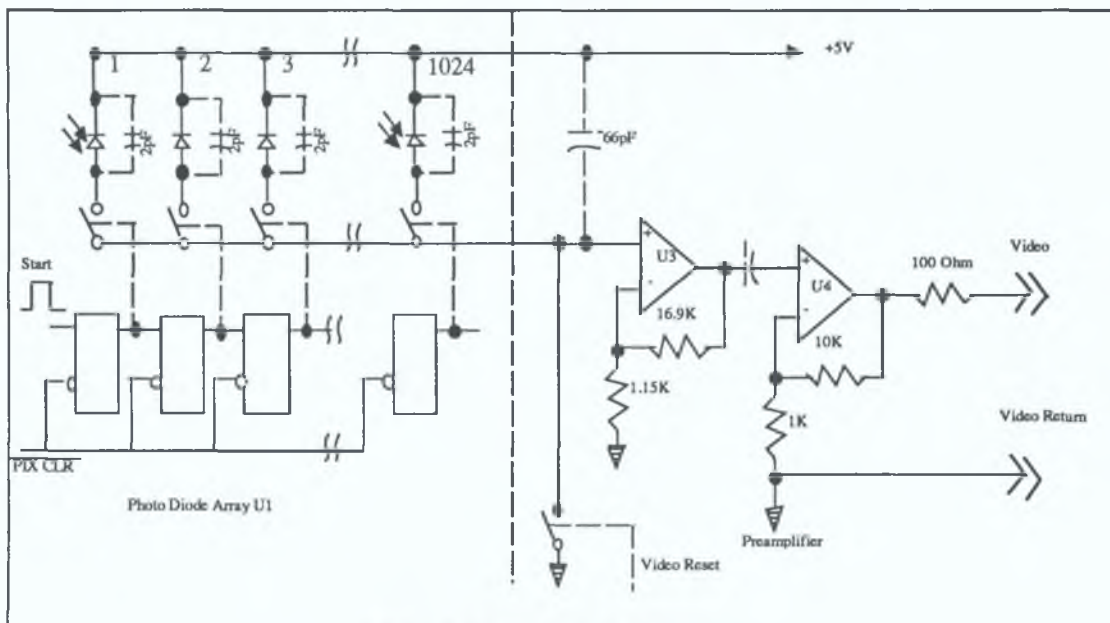


Figure 2.4: PDA Schematic.

The detector incorporates a Peltier cooler for normal operation down to 5°C and if water assisted, this value may be extended downwards to -19°C. It is necessary to provide a dry nitrogen flow to prevent condensation formation on the PDA surface and oxidation of the aluminium heat sink on which the PDA rests. The photodiodes in the array and an associated preamplifier, convert light signals to analog voltages. The analog signal is sent to the 1471A Controller via a 22 pin cable, where it is integrated, sampled and converted to a 15-bit digital data stream.

The 1024 reverse biased photodiodes function as an array of charged capacitors. When light strikes a photodiode, electrons are generated that neutralise holes to discharge the photodiode capacitance and change the voltage across the diode. The Photodiode Array is controlled by CMOS logic, driven by signals from the 1471A Controller. During exposure, the +5V voltage on each diode drops proportionally to the photon flux falling on the diode. During each scan, the shift registers and FET switches in the array package cause the photodiodes to be successively connected to the input of the detector amplifier. Each successive voltage level, defines the integrated photon flux on the address pixel. The resulting signal, following buffering and amplification is sent to the 1471A controller for digitising and data processing.

2.3.2 Model 1471A Detector Controller Interface.

The OMA detector interface is a desktop size device designed to acquire data from a light detector. The detector interface is controlled directly from the OmaSoft software package, which the author developed as part of this thesis. The parameters of the experiment are set directly from the software package including scanning, triggering, temperature control and data acquisition. The OmaSoft program was designed to network two EG&G OMA boxes present in the Laser Plasma Laboratory in DCU. A full discussion of the specification of this software is given in Section 2.6.

The PC communicates with the controller via a standard IEEE-488 GPIB Parallel interface, which allows for high speed memory loads and dumps. The 25 pin D-type connector on the rear of the controller is used to connect to the 1453A detector, via a 6004-0060 cable.

There are five BNC connections present on the rear panel of the 1471 OMA controller. For the purposes of the present experiments only the 'Trigger Output' and 'Sample and Hold Output (S/H)' are used. The '*Trigger Output*' comprises of a TTL pulse, 30 μ s (1 Pixel time) wide with a rising edge occurring 3 pixels after the last analog-to-digital conversion of the detector scan. The availability of this pulse is controlled by the data acquisition mode used by OmaSoft program (See Section 2.6). The '*Sample and Hold Output (S/H OUT)*' is a real-time PDA video signal and is coupled to a Hewlett-Packard HP54502A oscilloscope thereby allowing a spectrum to be viewed on a laser shot to laser shot basis.

2.3.3 OMA Operation and Specifications

The OMA box receives sets of special instructions from the PC OmaSoft package via a GPIB (General Purpose Interface Bus) network. The OMA parameters are sent as a set

of the special instructions from the PC, which the 1471 OMA interface interprets and executes On boot-up the OmaSoft program automatically sets the default parameters (number of scans, exposure time, temperature etc) in the OMA box. These parameters can be adjusted within a pre-defined range, from the OmaSoft program

The Nd YAG laser firing sequence is controlled via a TTL master pulse sent from the EG&G OMA box This pulse is passed through a digital delay generator, which generates a 12Volt, 28μsec output pulse Only one trigger pulse is required to fire the laser and the OMA box automatically generates a master trigger pulse whenever an experiment is run

When a ‘Single Experiment’ is run from the OmaSoft program a single master pulse is sent to the Nd YAG laser controller which fires a laser pulse of ~ 15ns duration At the same time, the 1453A detector integrates (scans) the incident photon flux for 30ms The analog signal is read from the detector by the OMA box, where it is then digitised (15-bit) and stored, in one of the six available memories The video output signal from the 1471 controller, as shown on the HP 54502A oscilloscope, can also be viewed directly on the PC monitor, for closer pixel by pixel examination

It is possible to repeatedly fire the laser and integrate each scan several times (Accumulate Mode) before storing it in the 1471A controller box thereby improving the overall signal to noise ratio of the image

When a satisfactory spectrum has been obtained, the 1024 pixel values stored in the OMA box memory may be transferred and saved to the PC’s hard drive This is done directly from the OmaSoft program The data is stored in ASCII file format in the current working directory of the PC

The OmaSoft program allows the user to maintain, full control over the data acquisition parameters A discussion of the main parameters, defined in the OMA box are now presented

- Exposure Time
- Number Of Scans
- Delay Between Scans
- Number of Memories Used
- Current Memory
- Data Acquisition Mode
- Detector Temperature

- **Exposure Time (ET).**

The exposure time is the total time between each successive read of the detector elements (or pixels). The minimum Base Exposure Time, for the 1453A detector is 30ms. The total Exposure Time must be set to an integer multiple of 30ms, otherwise the OMA processor will automatically select the next lower acceptable value. The Base Exposure Time is divided into 3 sections Scan Time, Overhead Time, and Variable Time.

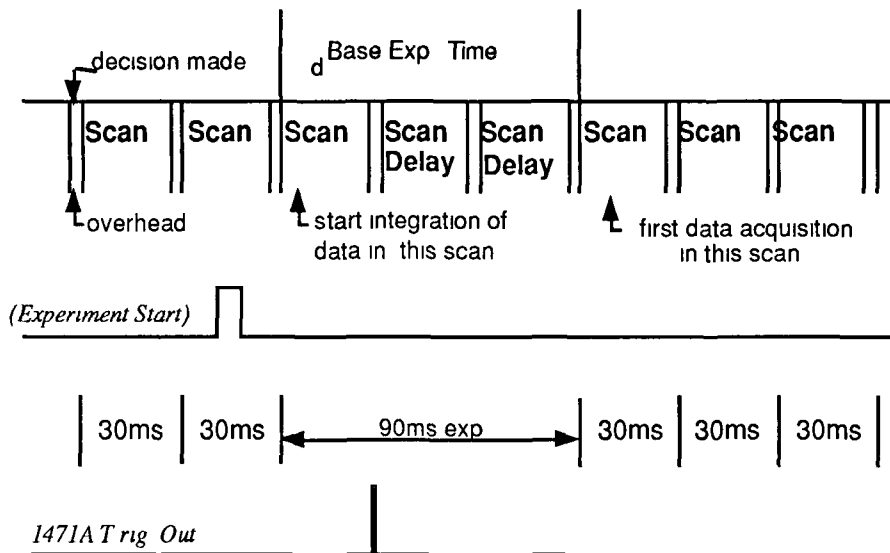


Figure 2.5: Timing Diagram of the 1453A PDA

- **Scan Time** is the interval during which pixels are read/reset and data is transferred from the OMA controller to the computer. For the 1471A detector interface running in Normal Mode, the scan (integration) time is 28 μ s/pixel
- **Overhead Time** is of a fixed duration for a particular hardware configuration, during which time, the OMA's Motorola 68000 processor makes decisions regarding the next detector scan (See Figure 2.5)
- **Variable Integration Time** follows the Overhead Time. This is the signal integration time that varies with the user entered exposure value. The longer the exposure time, the longer the photon flux is integrated and the better the signal-to-noise ratio that will be obtained (See example above for a 90ms exposure time)

In the example above a 90ms exposure time has been set in Normal Sync mode. Scanning takes place continuously and hence transparently to the user prior to the start of an experiment in order to prevent dark current build-up on the detector head. Each scan begins as soon as the preceding Overhead Time is completed.

The following is a description of the events that occur for the above example

- An experiment is said to begin when the RUN command is sent to the 1471A from the PC OmaSoft program
- The scan in progress runs to completion, the experiment is started and decisions are made on what to do next based on the Data Acquisition mode. (4 as used in this experiment)
- Another scan takes place, followed by the Overhead Time. This is the first post-start Scan. As soon as the first pixel is read/reset, integration continues until the pixel is read again. A Trigger Out Pulse is sent at the end of the first Scan
- A delay scan follows the start scan to achieve the set Exposure Time of 90ms
- The next real scan follows the delay scan Overhead Time and data is acquired from the 1453A

Dark currents are also integrated during exposure and therefore directly limit the maximum practical exposure time. If an integration continues for long enough it will eventually saturate the detector. The Exposure Time parameter is set, by sending the command "ET 0.03" to the OMA box which would set an exposure time of 0.03 seconds.

- **No of Scans (I)**

This parameter sets the number of scans to be read into the memory by the detector. Each scan is added to the current memory. This scan counter parameter is set by sending the "I #" command to the OMA box where # indicates the number of scans to be summed. The default value for this parameter is 1.

- **Delay Between Scans (K).**

This parameter is used to provide a time interval between one scan and another. During this time the pixels are read and reset, but no data is taken. These type of scans are called IGNORE scans. Because all detector elements are read and reset during ignore scans, very long delays can be introduced without concern for detector saturation, due to dark current build-up. The OMA parameter K accepts an integer value, the actual time delay obtained is 0.03 sec multiplied by the integer value. The default value for this parameter

is 0 This is useful when triggering lasers at repetition rates of $< 1/30 \times 10^{-3}$ Hz = 33Hz
For example 33 ignore scans imply the OMA controller will trigger a laser at 1 Hz

- **Number of Memories Used**

This parameter sets the active number of available memories which the user can store spectral data in. The 1471A detector interface has 512K of on-board RAM. Each memory is designated a portion of the detector interface RAM, with each memory identified by an integer number between 1 and 6. Only one active memory can be set for acquiring data, however the five additional memories can be used to store previous data information. Any memory can be added, subtracted, divided or moved to another memory. Memory One is the default memory of the OMA box and all data will be automatically stored in it. The maximum number of memories to be used is set using the MAX MEM command. The default value for this parameter (with 1024 Pixels and in Double Precision Mode) is 6.

- **Current Memory (MEM)**

The currently active memory is changed by using the MEM command. The valid range of inputs for this command is between 1 and 6. There is no advantage/disadvantage to using any of the memories except for convenience purposes. The default value for this parameter is 1.

- **Data Acquisition Mode (DA)**

There are 17 different DA modes stored in the ROM of the OMA box. Each mode has its own particular characteristic. All DA modes may be used with the OmaSoft program. However the mode most useful for pulsed laser spectroscopy is DA 4. When the 'RUN' command is sent to the 1471A to activate the data acquisition mode, all memories are automatically set to zero. The following is an outline of what happens in DA mode 4, with I = 5 and K=10

DP 1	Set Data Precision = Double
DO I	Repeat for I number of Scans
TOUT	Send Trigger Out
ADD	Add I scans into current mem
DO K	Repeat K ignore scans
IGN	Ignore Scan
LOOP	K Loop to 10
LOOP	I Loop to 5
STOP	End

Effect:

- 1 A Scan is performed, with a Trigger Out signal sent at the beginning of the exposure time
2. The data from the scan in step 1 is ADDED into Memory 1
3. The next 10 steps are ignored
- 4 Steps 1 through 3 above are repeated four more times
(The data from the un-ignored scans are ADDED into Memory 1)

The net result is that five successive spectral scans are averaged with a delay of 10 x Exposure time between each scan

- **Detector Temperature (DT)**

This parameter sets the temperature of the Model 1453A detector head. A Peltier cooling system tries to bring the system to that temperature and then lock to it. If successful, the 'COOLER LOCKED' indicator on the front of the 1471A will light. The range of valid detector temperatures is between -19°C to 25°C. The temperature is set via the 'Edit Parameter Config' menu option in the OmaSoft program. For the 5°C temperature used as standard in the DCU laboratory, no circulation of cooling liquid through the detector head is required. For temperatures lower than this, liquid assisted cooling of the Peltier device would be required.

2.4 The Nd:YAG Laser System

The laser used throughout this work was a Spectron Laser Systems, Q-Switched Nd YAG SL800 laser featuring a two stage oscillator/amplifier system

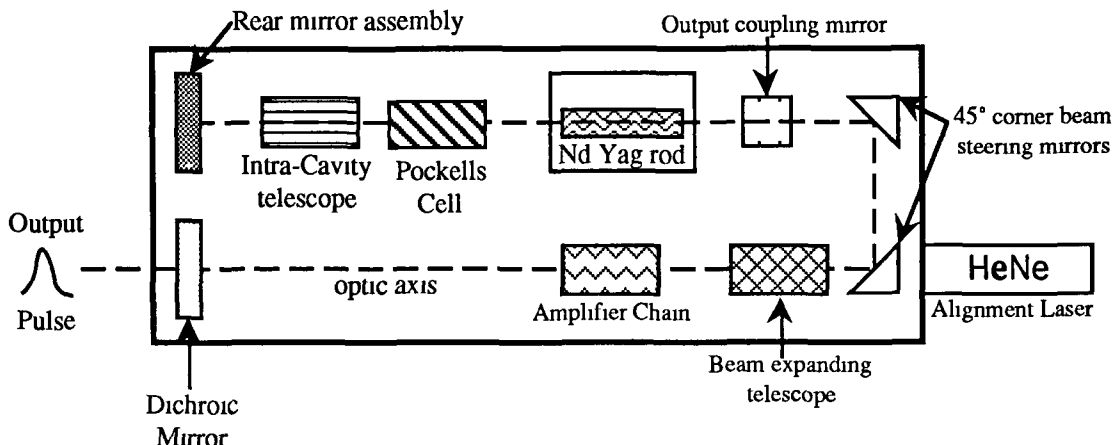


Figure 2.6: Schematic diagram of the Nd YAG laser head

The active medium is a crystal rod of yttrium-aluminium-garnate(YAG, $\text{Y}_2\text{Al}_5\text{O}_{12}$) doped with neodymium (Nd^{3+}) ions. The crystal is optically pumped by radiation emitted from powerful discharge flashlamps to obtain a population inversion. Optical shuttering (using a Pockels cell) inhibits normal lasing action of the system for a pre-defined time after the pumping pulse has started in order that an optimal population inversion is achieved. On opening the shutter this stored energy is suddenly released (termed Q-switching) resulting in the laser radiation being delivered in a giant, single optical pulse at 1064nm (fundamental frequency). This giant pulse typically contains 1 joule of energy in 15-20ns (FWHM). The laser pulse is focused through a glass window port on the target chamber and onto the target surface. This is done via a f/5, 10cm focal plano-convex lens mounted on an X-Y translation stage outside the target chamber. The focused area of the laser beam is diffraction limited but lens aberrations and mode structure of the beam can increase the spot size to 2-100 times the diffraction limit. The spot size radius ω is estimated from the following equation

$$\omega \approx \frac{\lambda f}{\pi x \vartheta} \quad (23)$$

where λ is the wavelength of the laser light, f is the focal length of the lens, x is the laser aperture to lens distance and ϑ is the divergence of the Gaussian laser beam. For the Nd YAG laser beam, $\lambda = 1064\text{nm}$, $\vartheta = 2\text{mrad}$, $x = 7\text{m}$ and using a 10cm focal length lens, the theoretical spot diameter (2ω) is $\approx 0.3\text{mm}$. This discrepancy can be accounted for considering the Nd YAG is multimode and that the lens is not aberration free. The

illuminated target surface area is approximately $\pi(5 \times 10^{-5})^2 \approx 10^{-8} \text{ m}^2$. A laser pulse of 1J delivered over 15-20ns is equivalent to an average power of 40MW. If the focal area of the beam is 10^{-8} m^2 , then the corresponding laser power density is $\approx 4 \times 10^{15} \text{ W m}^{-2}$.

2.5

Modifications to Acton VM-521 Spectrometer.

The ARC VM-521 instrument is a high vacuum system with a leak rate of $< 10^{-10}$ cc/min. For vacuum operation of the system it was necessary to design and construct

- A vacuum target chamber and coupling system
- A CEMA to VM-521 vacuum coupling flange
- A Turbomolecular pumping rig to VM-521 adapter flange

A description of each of these elements is now presented

2.5.1 The Target Chamber and Mounting design

The target chamber consists of a cube of aluminium of side length 127mm through which 5 mutually perpendicular holes of diameter 71mm were machined normal to each of the adjacent faces respectively. This presents the user with 5 user ports and a solid base. The solid base allows the cube to be independently supported and hence reduces any strain on the entrance arm of the spectrometer. Each face has four M4 tapped holes on all except the base, which facilitates the attachment of the 5 vacuum flanges

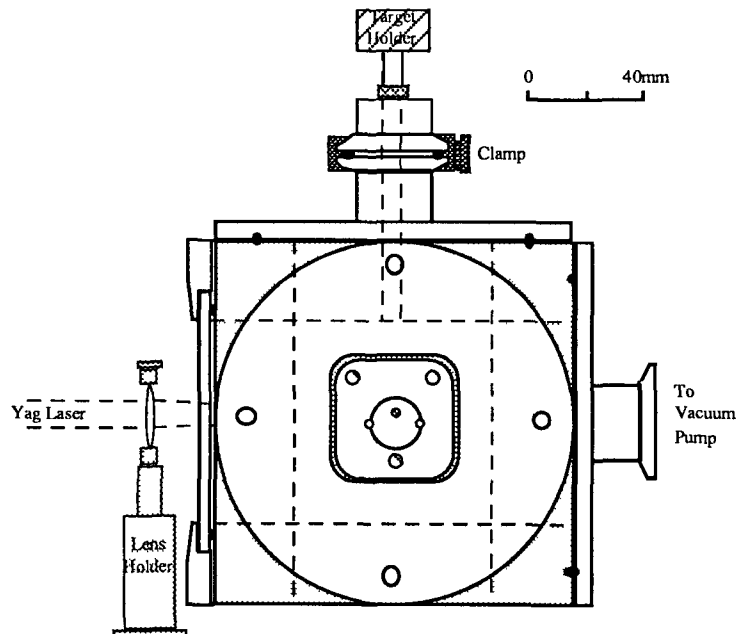


Figure 2.7: Side View of Target Chamber Assembly

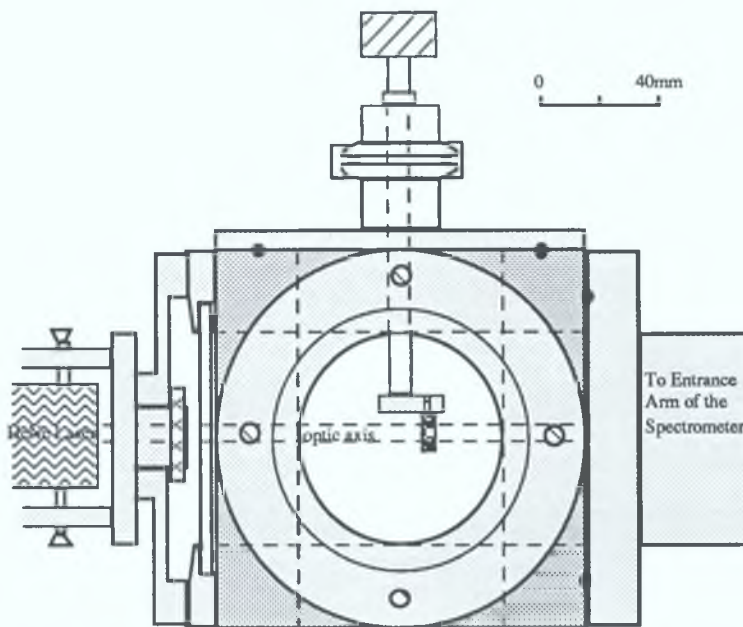


Figure 2.8: Front View of Target Assembly.

The laser pulses were admitted to the target chamber by means of a 6mm thick glass window secured to the front of the cube by a circular aluminium locking ring of diameter 127mm. The effective window diameter matched the chamber bore of 71mm. An O-ring gasket seal comprises of two bearing rings which hold the Buna-N O-ring in place. Four M4 bolts secured the window port to the cube which compressed the O-ring against the smooth cube surface. A similar window port on the left side of the cube had an aluminium laser-craddle mounted onto it by means of four M4 bolts. The HeNe laser mounted in this cradle was used for alignment along the optic axis of the spectrometer. The laser cradle was attached to a stainless steel plate by means of a hollow threaded rod and mating nut. Once the alignment laser was located in the frame it could be positioned laterally and vertically by means of four bolts and supporting springs.

Two stainless steel DN40 adapter flanges were constructed to (1) connect a DiffStak™ vacuum pumping system to the target chamber cube and (2) mount the target holder onto the cube. The adapter flanges were constructed by welding a Caburn K150-1 DN40 tubulated flange to a matched bore stainless steel plate. A standard O-ring groove was machined on the reverse side of the plate. Four M4 bolts secure the flange to the cube which compresses the O-ring to the cube face.

The DN40 adapter flange used to mount the target holder was located on the top of the cube. The target material is positioned in the cube using a Balzers sliding shaft Wilson seal component. The target material (M6 bored) is secured to the end of the sliding shaft by means of an M6 bolt. The target holder provides vertical and rotational positioning of

the target material along the optic axis, defined by the alignment laser. By mounting the target material offset from the target holder sealed rod, an eccentric motion of the target was achieved thereby allowing the target to be moved laterally with respect to the optic axis of the VM-521.

The cube was mounted on the spectrometer using a *custom designed flange adapter*. This adapter flange mates the 5" American standard entrance arm flange to the standard cube flange. A glass capillary array (GCA) was incorporated into the flange to establish a pressure differential between the target chamber and the spectrometer while still transmitting VUV radiation. GCA's have become commercially available at reasonable cost due to the advances made in manufacturing MCP's. GCA's consist of glass capillaries of very small diameters (pore size 10 -> 50 μm available) packed in arrays yielding large spatial apertures. Soda lime glass is used as the basic standard matrix material due to its mechanical strength and chemical stability. GCA's are manufactured with an open area ratio of 50% or greater. Light transmission and gas flow characteristics are both largely dependent on the length to diameter ratio ($\alpha = L/D$). The GCA used in this system was manufactured by Galileo Electro-Optics Corporation and has a diameter of 25mm, pore size of 50 μm and thickness of 4mm (i.e. $\alpha = 80$).

The main body of the *custom designed flange* adapter was machined from aluminium and has an overall length of 100mm and a diameter of 127mm ($\approx 5"$). An O-ring groove and four M4 holes were machined into the cube side of the adapter flange. The adapter flange was attached to the spectrometer via six American standard bolts. A vacuum seal was provided by the O-ring fitted to the face of the mating flange of the spectrometer. The GCA is set off-centre in an adjustable mounting plate which allows for slight angular alignment of the GCA with respect to the optic axis of the VM-521. The GCA is masked off from the direct plasma plume by an aluminium disk with a 3mm diameter hole set off centre but on the optic axis of the spectrometer. The GCA can be rotated around the optic axis so that a clean surface can be used each time it became contaminated with plasma blow-off. The GCA is positioned by three M4 bolts and the O-ring seal and is held to the plate by two bolts on either side of the diameter.

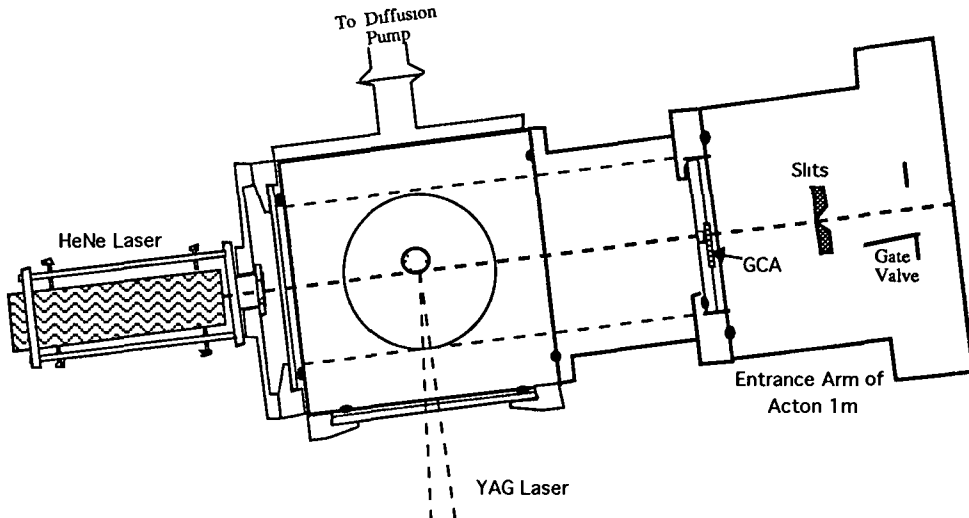


Figure 2.9: Plan view of the Entrance Arm housing on Acton 1m
 (Target holder and DN40 flange omitted for clarity)

Before attaching the entrance arm adapter flange to the Acton 1m it was necessary to align the GCA channels parallel to the optic axis using the HeNe alignment laser. This was accomplished by examining the speckle pattern formed on a white background some distance from the output face of the GCA. The plate position was optimised (adjustment of the three M4 bolts) so that the sharpest possible image was formed on the background. When this position was found, the GCA was not subsequently tampered with.

2.5.2 The Optical Detector Coupling Design

In order to mount the optical detector to the exit arm on the Acton 1m spectrometer, it was necessary to remove the exit slit housing. Determination of the exact location of the slit jaws was required before removing the assembly from the spectrometer. This measurement is critical, since it yields a point on the focal curve of the concave grating. Having measured this distance from the mounting face of the exit arm, an exit arm adapter was designed and constructed in-house to mount the MCP.

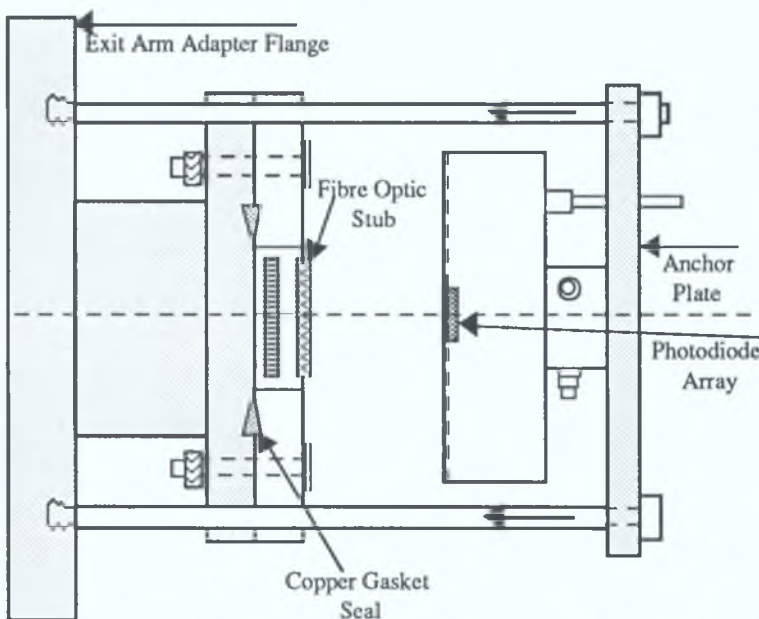


Figure 2.10: PDA Mounting Assembly ; Side View.

The adapter mated the 4.5" CF114 MCP flange to the 6" mounting flange on the exit arm of the spectrometer so that the centre of the MCP input face lay exactly tangential to the Rowland circle of the VM-521.

The exit arm adapter also has provision for butt-coupling the EG&G 1453A Photodiode Array to the MCP fibre-optic stub by incorporating 4 supporting rods and an anchor plate. The anchor plate is a square aluminium plate of side length 130mm and thickness 9.3mm. The PDA is mounted on the anchor plate at the alignment slots via two M4 screws. The anchor plate is fitted with 8mm through holes at each corner which slot onto the four supporting rods protruding from the stainless steel face of the adapter flange. The anchor plate (fitted with the PDA) is positioned along the four rods and located with the face of the PDA touching the MCP fibre-optic stub. An assembly of bolts and springs at the end of the rods secure the anchor plate and prevent excessive pressure being applied to the MCP-PDA faces. The PDA detector head is oriented vertical to the MCP fibre-optic plate using the alignment slots in the anchor plate and a spirit level. The anchor plate also

incorporates a 5mm hole to facilitate connection of gas port tubing, and a rectangular piece cut from the base of the plate for connection of a 22 pin OMA cable to the 1463A detector

The adapter flange comprised of a Caburn CF114-63 tubulated flange welded to a 6" centre bored (66.7mm) stainless steel blank. An O-ring groove and six blind M6 holes were machined into the reverse side of the stainless steel blank to facilitate the attachment of the adapter to the exit arm flange with a vacuum seal. A further four M8 holes were drilled into the front side of the blank to accommodate the four rods of the PDA cradle frame. The MCP was mounted to the CF114 face of the adapter flange by six M8 bolts and a copper gasket seal. It was necessary to reduce the height of the M8 bolts to less than 2mm because they prevented the PDA butt-coupling to the MCP face without obstruction.

2.5.3 The Vacuum System

The spectrometer side of the system is pumped by a Balzers TSH 242 turbomolecular pumping unit, which comprises of a TPH 240 170 l/s turbomolecular pump and a DUO 016B rotary vane backing pump. The unit is managed via a TCS 303 pumping control unit and a TCP 121 electronic drive unit. The turbomolecular pump is mounted on the 8" Conflat flange provided at the base of the Acton 1m spectrometer via a zero-length CF150-100 flange adapter.

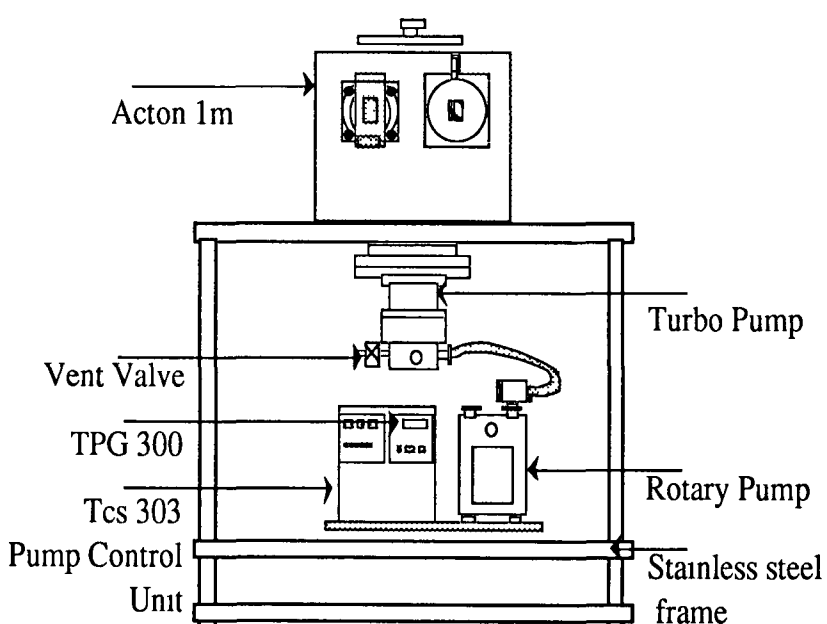


Figure 2.11: Turbomolecular Pumping Setup of Acton 1m

The TPH 240 is backed by the DUO 016B rotary pump to which it is connected via a DN25 flexible coupling. This flexible coupling isolates the vibrating rotary pump from the spectrometer body. The system can provide a vacuum $< 5 \times 10^{-8}$ mbar quite easily after several days pumping. Most of the connections and flanges were sealed by Buna-N O-rings which were lightly smeared with Apiezon type M vacuum grease to prevent degradation of the O-rings under repeated compression and expansion cycles as the system is evacuated and vented.

The system is filled with dry nitrogen gas each time it is vented to atmospheric pressure. It is good vacuum practice to vent with dry nitrogen gas as this greatly reduces the pump-down time of the system. This nitrogen gas forms a protective gas layer on all exposed surfaces within the vacuum system, such that hydrocarbons cannot bond directly to these surfaces and will be rapidly removed when the system is put under vacuum again.

A foreline trap is mounted above the DUO 016B to reduce vapour backstreaming and to filter out most of the liquid oil contamination coming up the line from the rotary pump when power is removed. A foreline valve is mounted between the trap and the Turbo exhaust port. This valve is closed whenever the Turbo is to be vented and prevents backing pump oil and vapour getting to the Turbo and spectrometer.

The target chamber side of the system is pumped by a combination of a Leybold-Heraeus diffusion pump (330 l/s), fitted with a nitrogen trap and backed by an Edwards SpeediVac rotary vane pump.

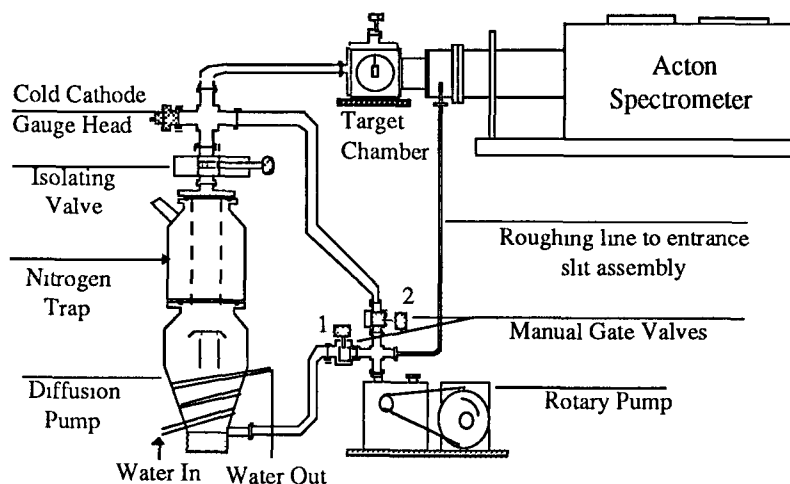


Figure 2.12: Target Chamber and Diffusion Pump setup

The diffusion pump is connected to the target chamber via a CF100-DN40 reducing piece, a DN40 Isolating valve and a DN40 flexible coupling. The flexible coupling is attached to a DN40 flange port on the cube via a combination of standard Buna-N O-

rings, centering rings and hinged clamp assemblies. The nitrogen trap above the diffusion pump prevents oil vapour from the pump getting into the vacuum system.

A manual gate valve is included between the target chamber and the entrance arm of the spectrometer, so that the target chamber may be vented independently of the spectrometer. This allows targets to be replaced without disturbing the spectrometer pressure and thus reducing the turnaround time of the experiment. The GCA incorporated into the design of the target chamber mounting flange facilitates a pressure differential between the chamber and the spectrometer. This eliminates the necessity for exact equalisation of the pressures in the chamber and spectrometer. The ultimate pressure of the spectrometer is driven by the UHV requirements of the MCP detector. The MCP must not be operated at pressures greater than 2×10^{-6} mbar. The pressure in the target chamber however can be much higher than this. The GCA has the added advantage of preventing plasma blowoff reaching the spectrometer slits / housing and thus contaminating the surfaces.

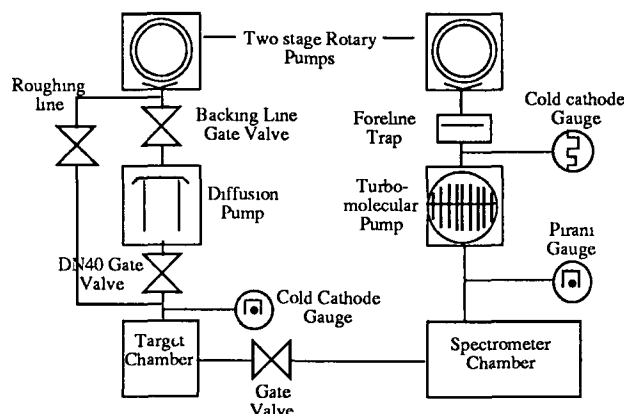


Figure 2.13: Schematic of Vacuum System (ISO Symbols)

The vacuum pressures are recorded with a Balzers IKR 020 cold cathode gauge head, and a Balzers TPR 010 Pirani gauge head, which are both read by a Balzers TPG 300 controller. The IKR 020 is used to measure high vacuum (HV) pressures between 10^{-3} - 10^{-9} mbar, while the TPR 010 is used as a pressure sensor in the medium vacuum (MV) range of 100 - 10^{-3} mbar. A KF-40 type port at the base of the spectrometer provides for the connection of the IKR 020. Since it is not possible to take pressure measurements at the MCP face inside the spectrometer it was estimated that a pressure of $< 5 \times 10^{-7}$ mbar at the base of the spectrometer, guaranteed a minimum pressure of $< 1 \times 10^{-6}$ mbar at the exit arm which is required for operation of the MCP.

2.6 The PC OmaSoft Package.

2.6.1 Introduction

The menu driven software program "OmaSoft" controls the entire operation of the Laser Plasma experiment at the DCU Laboratory

When the program is executed an introduction screen appears followed by a screen showing three Oma configurations available to the user The options are

- 1) 1m Acton OMA
- 2) 2 2m McPherson OMA
- 3) Both 1m & 2 2m OMA's

The user chooses which system(s) to make active for the Laser Plasma experiment by pressing 1,2 or 3 The menu environment comprising of 8 menu bar items is started after the current Oma configuration is chosen The menu bar items include

Setup Files Run Math Plot Terminal Parameters Scan

Each of these menu items is accessed by pressing the first letter of the menubar item on the keyboard or, by using the left and right arrow keys to highlight the required menubar item and then pressing Enter

2.6.2 SETUP Menu

The 'Setup' menu item controls the configuration of the OMA controller boxes It contains the following options

- *GPIB/OMA Initialisation*
- *View OMA Configuration*
- *Change OMA Configuration*
- *Quit Oma Program*

It is possible to change the system(s) currently active by selecting the *GPIB/OMA Initialisation* option This option allows the user to re-select which of three system setups they want When selected the user is returned to the menu environment with the new system configuration now active The OMAparameters as described in section 2.2 3 can be viewed and altered using the *View OMA Configuration* and *Change OMA Configuration* submenu items respectively In each case a dialogue box showing the current parameters is displayed The parameter is selected using the up/down arrows keys and edited by then typing the new value (within the allowed range)

2.6.3 FILES Menu

The files menu controls the storing and handling procedures of the spectral data in the Oma Controller(s) It contains the following options

- *Save To File*
- *Save Range*
- *View File*
- *Directory*
- *Change Directory*
- *Delete File*

Spectra (stored in any of the six memories in the OMA controller) can be downloaded to the current directory on the PC, using the *Save To File* or *Save Range* option The current directory is chosen using the *Change Directory* menu item The *Save Range* menu item differs from the *Save To File* menu item in that you can save a specified number of data points rather than the complete 1024 points (e.g. 300 - 700) The *View File* allows you to view the contents of a previously saved data file stored in ASCII file format The *Directory* menu item shows the contents of the current directory The *Delete File* menu item allows you to delete a user specified file from the current directory

2.6.4 RUN Menu

The Run menu controls when user-defined or standard experiments are started

An experiment for the case of the Acton 1m comprises of

- 1) Sending Firing command to 1471A Controller from PC
- 2) Trigger Out sent from 1471A to delay generator (TTL - CMOS conversion)
- 3) CMOS Trigger Pulse sent to Nd YAG Laser Controller, Laser Fired
- 4) Data Acquisition and storage in 1471A Controller memory as defined by the OMA parameters

The four options available to the user in this menu are

- *Live*
- *Single Shot Accumulate*
- *Single Shot*
- *Run Experiment*

The *Live* menu item is primarily used when setting up the plasma alignment on the spectrometer It provides a real-time graphical display on the PC of what is being read by the 1453A PDA detector The screen is updated every base exposure time of the PDA.

The *Single Shot Accumulate* option allows the user to store individual spectra in any one of the six available memories in the 1471A. Each time a laser plasma is formed, a dialogue box shows the average pixel value read by the PDA. Based on this information and on the inter-laser jitter (in the case of the dual laser plasma experiment), the current spectrum can be moved to a memory assigned with this jitter/average pixel count.

The *Single Shot* menu item runs an experiment using default OMA parameters ($I = 1$, $K=0$, $ET = 0.03$). This has the effect of firing the laser once and integrating the 1453A PDA for 30ms. A dialogue box shows the average pixel count for each scan.

The *Run Experiment* option runs an experiment using the currently set OMA parameters as entered by the user.

2.6.5 MATH Menu

The Math menu provides some mathematical handling routines for use with the spectrographic data files. The menu items are available are

- *Log Io/Iabs*
- *Iabs/Io*
- *Average Std/Dev*
- *Add Data*
- *Subtract Data*
- *Integrate Data*

The *Log Io/Iabs* is used to obtain an absorption spectrum from backlighting and target plasma data files. *Iabs/Io* is used to find the transmittance of the backlighting plasma. *Average Std/Dev* shows the average pixel value and standard deviation of the data stored in the currently active memory. The *Add Data* menu item takes two files, adds the data points in one to the corresponding data points in the second and outputs the resulting data to a third file specified by the user. *Subtract Data* takes two files, subtracts the first set of data points from the second, then saves the resultant data to a user entered filename. The *Integrate* option sums all the data points in a specified file and displays this value in a dialogue box.

2.6.6 PLOT Menu

This menu controls the viewing of data files or 1471A memories in graphical format on the PC screen. The available options are

- *Plot Data File*
- *Plot Memory*

The *Plot Data File* menu item allows you to select a previously saved data file and plot the contents in a graph on the PC. This plot can then be viewed pixel-to-pixel. The *Plot Memory* option lets you view the contents of data stored in any one of the six memories of the 1471A OMA controller.

2.6.7 TERMINAL Menu

The Terminal menu lets the user perform direct handling of the OMA controller. The options available are

- *Oma Numbers*
- *Wipe A Memory*
- *Wipe All Memories*

The *Oma Numbers* option lets you view the identification number of the OMA controllers currently active. The *Wipe A Memory* item lets you reset the contents of any memory (to zero) stored in the OMA controller(s). The *Wipe All Memories* option resets all the memories in the OMA controller(s).

2.6.8 PARAMETERS Menu

The Parameters menu is used to set the experimental parameters in the OMA controller. It consists of

- *Exposure Time*
- *Scans*
- *Scan Delay*
- *Memory*
- *DA Mode*
- *Detector Temp*

The adjustment of the OMA parameters can also be accomplished in the SETUP menu (Change Oma Configuration option), however when only one parameter is to be set , it may be more convenient to use this method The required parameter is chosen from *Exposure Time*, *Scans*, *Scan Delay*, *DA Mode* and *Detector Temp* using the up/down arrows and then pressing Enter Once a new parameter value is entered, it has an immediate effect on the OMA controller The parameters have the same meaning as described in section 2.2.3

2.6.9 SCAN Menu

This menu controls the output wavelength presented by the Acton VM-521 spectrometer An allowed wavelength is between the range 0 and 325nm The options available are

- *Goto Lambda*
- *Scan Rate*
- *Scan From*
- *Scan To*
- *Scan Delay*
- *Scan Status*
- *Start Scan*

The desired wavelength is entered using the *Goto Lambda* option and the PC communicates this (via the RS232 port) to the SpectraDrive stepper motor controller The SpectraDrive controller sets the one meter concave grating to the appropriate angle to obtain the chosen wavelength The remainder of the menu items are used when the grating is to be scanned from a specified starting to a finishing wavelength and at a specified rate At the present time this facility is not required by the laser plasma setup, but is included in the software in the interest of completeness

2.7

Plasma Radiation - Spectrometer Coupling Considerations

2.7.1 Basic System modelling

The optical coupling of the VUV plasma radiation from the target chamber to the concave grating is examined here. As seen from section 1.2.4, the resolving power P of the grating reaches a maximum at an illuminated width W_{opt} (which we calculated to be = 96mm in section 1.3.5) of the concave grating. The theoretical resolving power of the grating is

$$P = \frac{Wm}{d} \quad (2.4)$$

where W is the exposed width of the grating (in metres), m is the order number ($=1,2,3\dots$) and d is the intergroove spacing (in metres)

Since the intergroove spacing and order number are independent of the optical coupling, we need to find the exposed width of the grating to get some indication of the maximum resolving power of our system. We assume a plasma diameter of 0.1mm, located a distance 180mm from the entrance slit of the Acton 1m. The 25mm diameter GCA is situated a distance 22mm in front of the slit jaws, having a pore size of 50μm and a thickness of 4mm. The area of the GCA exposed to the VUV radiation is a circle of diameter 3mm (by design). The experimental slit width used in this thesis was 50μm.

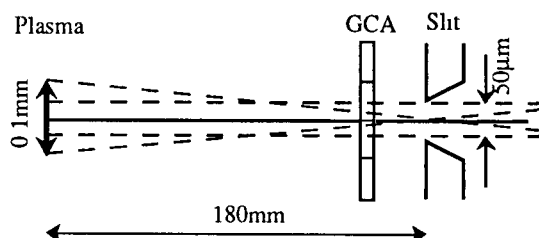


Figure 2.14: Ray Diagram of GCA Acceptance Angles

A schematic of this set-up is shown in figure 2.14. Only radiation passing parallel or nearly parallel to the optic axis will actually reach the grating.

The most important element in the optical coupling arrangement is the GCA, which sets the maximum angle of divergence and thus the maximum illuminated width of the grating. If we consider that the GCA pore diameter is 50μm and its overall length is 4mm then the maximum angle possible through the channel is

$$\tan^{-1}(50\mu\text{m} / 4\text{mm}) = 0^\circ 42' 58'' \quad (2.5)$$

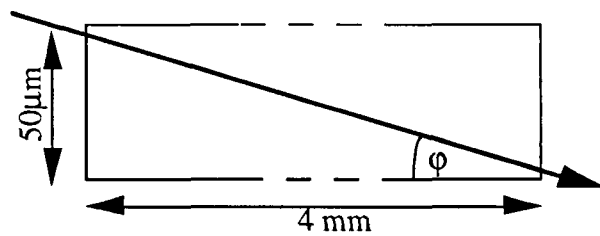


Figure 2.15: Maximum Acceptance Angle

So angles of incidence less than or equal to $0^\circ 43'$ are transmitted by the GCA. It further follows that of the 3mm diameter of exposed GCA, only a 0.55mm diameter circle of VUV radiation will be transmitted to the grating centred around the optic axis. From the slit jaws, the VUV radiation spreads out at an angle of $0^\circ 42'$ with respect to the optic axis, so that for a slit to grating distance of 995.4mm ($\approx 1\text{m}$), the exposed width is

$$\tan(0^\circ 42' 58'') * 995.4\text{mm} = 25\text{mm} \quad (2.6)$$

This width corresponds approximately to 25% of the total width of the grating (96mm). From equation 2.4 above the resolving power, at an illuminated grating width of 25mm is 30,000. Clearly this figure will be reduced by considerations of optical aberrations etc. The measured value quoted by the manufacturer is $\approx 5,500$ at 800Å.

2.8 Experimental Procedure

Having modified and aligned the 1m facility as described in section 2.4 above, the procedure used to record XUV spectra is now given

2.8.1 Experimental Preparation

The polyethylene target used in this experiment comprised of a solid rod of diameter 10mm and cut to a height of 60mm. A tapped M6 hole was machined into one end of the rod in order to bolt the target rod to the target chuck housing. The rod was handled with gloves and cleaned using a solution of isopropyl alcohol. Once attached to the end of the sliding shaft chuck, the assembly is placed in the target chamber and pumped down to a pressure of at least 10^{-2} mbar using a two-stage rotary pump. The target surface is positioned in the chamber so as to lie on the spectrometer optic axis as defined by the alignment laser. The alignment laser is incident such that an angle of 45° is present between it and the surface normal of the target rod.

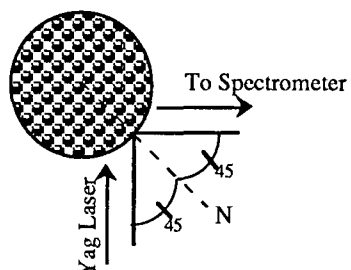


Figure 2.16: Incident and Observed angles at 45° to surface normal

A Diffstak diffusion pump is used to bring the target chamber pressure down to $< 10^{-5}$ mbar. With water circulating through the diffusion pump, the target chamber isolation valve closed and the backing line operational, the oil heater is switched on. A nitrogen trap above the diffusion pump is filled with liquid nitrogen. After 15 mins the target chamber isolation valve is opened and the target chamber is brought down to an operational pressure of $\sim 5 \times 10^{-6}$ mbar. All flanges and fittings are checked and tightened if necessary to ensure no leaks are present. A leak in the system will manifest itself by a longer than usual pump down time. Backfilling the target chamber with dry nitrogen gas each time it is vented to atmospheric pressure greatly reduces the pump down time of a regularly used system.

A maximum dry nitrogen flow of ≈ 2.5 L/min is provided to the EG&G 1453A detector head. This prevents condensation formation on the PDA surface which can cause

permanent damage to the detector. At this point the 1471A EG&G Controller box is turned on. Front panel indicators show the status of the detector. The 5°C experimental detector temperature is reached quite readily by the Peltier cooler so that no additional water-cooling is required for the 1453A.

The Bertan high voltage power supplies required to bias both the MCP and MCP-Phosphor gap are turned on and voltage is applied in stages to the CEMA inputs. Applying voltages too quickly results in arcing across the MCP/Phosphor gap which can lead to permanent damage to the MCP. A maximum voltage of -850V is applied to the V₁ input (channel), and a maximum voltage of +4.2kV is applied to the V_a input (screen) of the MCP according to the following procedure:

Time(min)	V _a	V ₁
0-5	2kV	-250V
5-10	2kV	-500V
10-15	4.2kV	-600V
15-20	4.2kV	-800V

Table 2.1: Application of Voltages to the EG&G CEMA

It is important to apply the voltages gradually in ever decreasing step sizes as the operating voltages are reached. It should be noted that the V₁ input determines the gain of the MCP, whereas the V_a input determines the resolution obtained from the MCP. A McPherson MCP arc sensing module will detect an arc in either the channel or screen bias and terminates the voltage connection to the CEMA inputs via an interlock cable to the Bertan power supplies. When this happens a front panel indicator will light, and the voltages on the power supplies must be set back to zero. A reset button on the MCP arc sensing module permits the re-application of voltages to the inputs again.

The Spectron YAG laser is turned on with water circulation on. The control panel is set to internal triggering mode with a repetition rate of 1Hz. This has the effect of warming up the laser flashlamps and provides both an improved beam quality and energy. After some minutes the laser pulse energy, profile, and quality may be recorded. An energy monitor connected to a HP oscilloscope is used to measure the pulse energy. The calibration for this energy monitor is 1J = 160mV. The energy of the laser pulse may be adjusted from the YAG controller panel. The operational oscillator and amplifier voltages are 900 and 1000V respectively. The laser energy is recorded at the laser head and at the focusing optics of the target chamber. The beam quality is recorded using a

section of blackened high contrast photographic paper. Again, this is recorded at the laser head and at the focusing optics. The laser pulse duration and profile is measured using a fast photo-diode (BPX-65) circuit connected via a BNC cable to a HP 400MHz oscilloscope. Typically the laser provides 800mJ at 1064nm in a 15ns FWHM pulse.

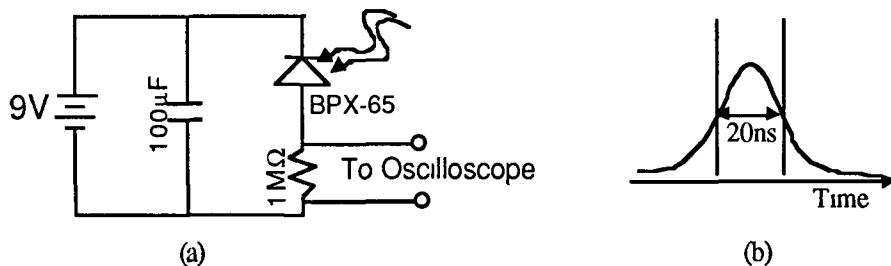


Figure 2.17: (a) Circuit used to measure beam profile,
(b) Typical profile obtained from Nd Yag Laser

The SpectraDrive controller on the Acton 1m is turned on and automatically initialises itself to the 0 Å (Zero order) wavelength setting

The pressure in the target chamber is read from a cold cathode gauge situated between the target chamber and the diffusion pump. If the pressure is equal to or below 10^{-5} mbar, the entrance arm valve on the spectrometer may be opened, since the CGA should be capable of holding off the higher pressure on the target chamber side. The pressure in the main body of the spectrometer may settle above its normal reading (valve closed), however as long as the chamber pressure is maintained below 1×10^{-6} mbar, this is acceptable.

The 'Trig Out' output from the 1471A controller box is connected to a delay generator using a 50Ω co-axial cable. The delay generator serves as a TTL/CMOS converter and is not used in this case for delaying the laser pulse.

The software program 'OmaSoft' is loaded and executed from the controlling PC. On boot-up the user selects the spectrometer system to be used. Option number one allows the Acton 1m to be run independently of the McPherson grazing incidence OMA system. Since the default detector temperature is 25°C, it is necessary to change the parameter setting to 5°C using the 'Change Oma Config' option in the Setup menu of the OmaSoft package. When the 1453A detector reaches the set temperature, the cooler locked indicator lights on the front panel of the 1471A Controller box. The desired wavelength setting (in Å) of the 1m grating is entered using the 'Set Wavelength' option from the Scan Menu. When the SpectraDrive controller reaches the desired wavelength, a dialogue box appears in the OmaSoft program confirming this.

The laser plasma experiment is now ready to accumulate data and the YAG laser interlocks are turned 'ON'

With the system now operational, it is necessary to optimise the position of the plasma in the target chamber. Using the 'Single Shot' option in the Run Menu a single laser pulse is fired. The average pixel value of this scan is displayed in a dialogue box. The video signal is displayed on a HP oscilloscope taken from the Sample and Hold (S/H OUT) connector on the rear panel of the 1471A, via a 50Ω BNC cable, with an amplitude range of 0-10V. The same video signal may also be viewed on the PC screen using the 'Run Live' option in the RUN Menu. This method has the added advantage of being able to examine a smaller range of pixels than the 1024 pixels offered by the S/H output. For higher ion stages the core of the plasma is moved closer to the optic axis. For lower ion stages the core is moved further away from the optic axis.

At this point it may occur that a particular spectrum may not fully utilise the dynamic range of the PDA. For a spectrum which saturates the array (i.e. pixel value greater than 32,767) it is necessary to lower the gain of the MCP (e.g. -50V) until the signal is wholly contained within the limits of the PDA. For a spectrum which barely fills the PDA, the MCP gain would be increased until adequate use was made of the full dynamic range.

Chapter 3

Results and Analysis

3.0 Introduction

This chapter presents results and analysis on carbon and tungsten laser plasma spectra recorded with the Acton VM-521 1m Normal Incidence Multi-channel spectrometer. These data will be used to illustrate the performance of the multichannel spectrometer in terms of

- Noise levels in the EG&G photodiode array
- Single -vs- Multi-laser shot averaged spectra.
- Spectral orders - relative intensities of spectral lines in higher orders.
- Comparison of carbon spectra from Acton 1m and McPherson 2.2m vacuum spectrometers in the 300Å - 500Å 'overlap' region.
- Spectral resolution enhancement using deconvolution techniques.
- Complete carbon and tungsten spectra in the 350Å - 2000Å wavelength region.

3.1 Noise Levels in the EG&G PhotoDiode Array

3.1.1 Introduction

It is important to have a knowledge of the noise characteristics of the photodiode array in order to estimate the noise present in an experimental spectrum. The dark current (i_d) and hence dark noise level is directly related to the operating temperature of the PDA. As the temperature of the PDA is reduced, the number of thermally generated electron/hole pairs decreases with a con-committant decrease in i_d and the noise on i_d . An operating temperature of 5°C was typically used during the experimental stage of the work reported in this thesis. Temperature control was achieved by means of a Peltier cooler coupled to the PDA.

3.1.2 Noise Characteristics.

Noise in PDA's has been discussed in some detail by Simpson [32] and the main points of his analysis are summarised here. Silicon PDA's suffer from so-called fixed pattern noise 'FPN' which is caused by a combination of dark current and coupling of clock phases onto the video lines. This FPN is reproducible if the array temperature and readout rate are kept constant from frame to frame and thus may be removed by subtracting a dark

scan from a scan containing the optical information of interest Random noise in PDA's is generally due to the following sources

- 1 Photon (Shot) noise on the incident light
- 2 Shot noise on the dark current
- 2 Noise due to the preamplifier
- 4 The reset noise of the pixels of the array ('KTC' noise)

The first noise component is an unavoidable natural source which follows Poisson statistics The last three sources of noise are relevant to the design of a good amplifier The dark current shot noise in electrons is given by

$$n_d = \sqrt{(\iota_d t_f / q_e)} \quad (3.1)$$

where ι_d is the dark current, t_f the time between readouts and q_e the electronic charge If we take $\iota_d = 10\text{pA}$, $t_f = 30\text{ms}$ and $q=1.602 \times 10^{-19}$ then $n_d = 1368 \approx 1\text{e}^-/\text{pixel}$

The noise due to the preamplifier is

$$n_d = (C / q_e) [4kTB(k_o / gm)]^{1/2} \quad (3.2a)$$

where k is the Boltzmann constant, B is the Bandwidth, T is the absolute temperature, and k_o/gm is the channel resistance of the input FET and C is the capacitance at the amplifier input which is composed of

$$C = C_v + C_{amp} + C_s \quad (3.2b)$$

where C_v is the video line capacitance of the photodiode array, C_{amp} is the preamplifier input capacitance, and C_s is any stray capacitance to the amplifier input mode For $B=10\text{MHz}$, $KT=1/40\text{eV}$, $C=10\text{pF}$ then $n_d \approx 250$ over 1024 pixels

The pixel reset noise is given by

$$n_r = (1 / q_e)(kTC_p)^{1/2} \quad (3.3)$$

where C_p is the pixel (diode) capacitance The pixel noise is larger than this however due to the multiple readout switching structure of the PDA and the lowest total reset noise available to an off-chip amplifier is

$$n_r = (1/q_e)[kT(2C_p + 2C_{vc})]^{1/2} \quad (3.4)$$

where C_p is the pixel diode capacitance and C_{vc} is the video line to clock capacitance.

Applying equation (3.4) to the 1024 element S series array used in this thesis , with $C_p = 2\text{pF}$ and $C_{vc} = 1.2\text{pF}$ yields at 20°C , $n_r \approx 1000$ and at -5°C , $n_r \approx 950$. This noise contribution tends to be two or more orders of magnitude greater than any other noise source.

3.1.3 Analysis of the Noise in System.

In order to obtain data regarding the dark noise levels it was necessary to remove the PDA from the exit arm of the Acton spectrometer and place in a light tight environment. The PDA temperature was set to 5°C to simulate typical experimental conditions and the PDA scanned for varying exposure times (30, 60, 120, 240, 480, 960 ms). A plot of the pixel value vs. pixel number is presented in figure 3.1 and the average dark pixel value at each of these exposure times is shown in figure 3.2a. The value of the dark pixel value is 700 counts at an exposure time of 960ms is comparable with the manufacturers value of 910 counts at 800 msec (5°C).

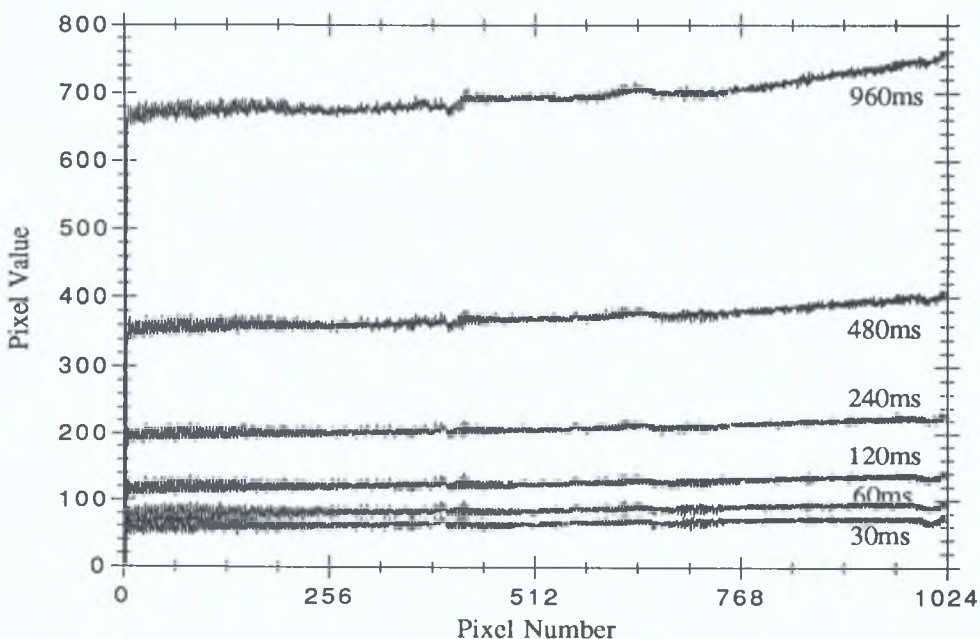


Figure 3.1: Plot of the noise pixel values for varying exposure times.

The reader should note that the saturation count value for the PDA is 32,768 and hence the dark current level at a detector temperature of 5°C is less than 3% of this value at an exposure time of 1 second (960 ms).

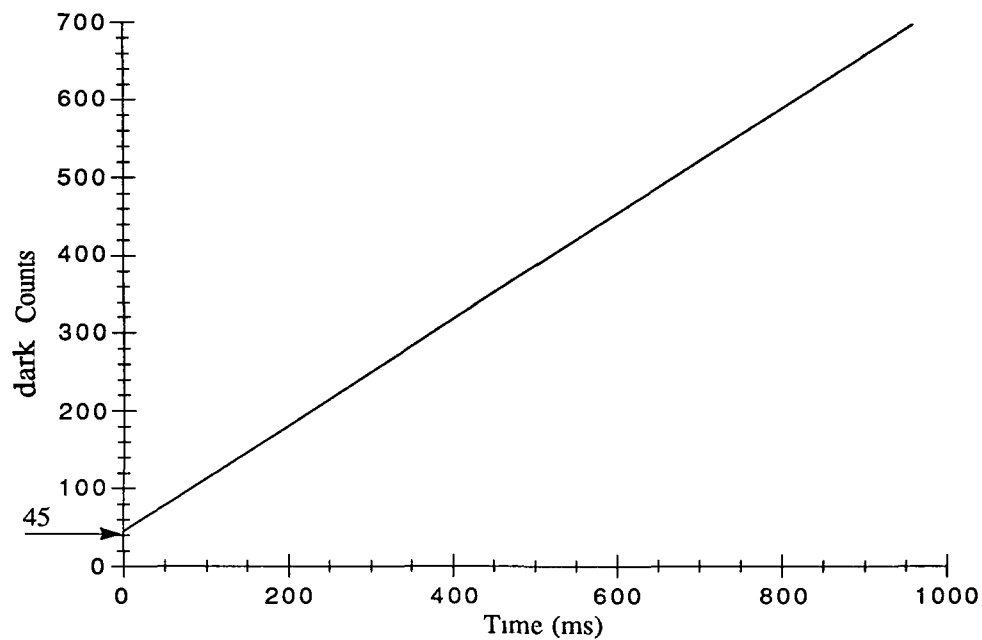


Figure 3.2a: Plot of the average pixel count per exposure time

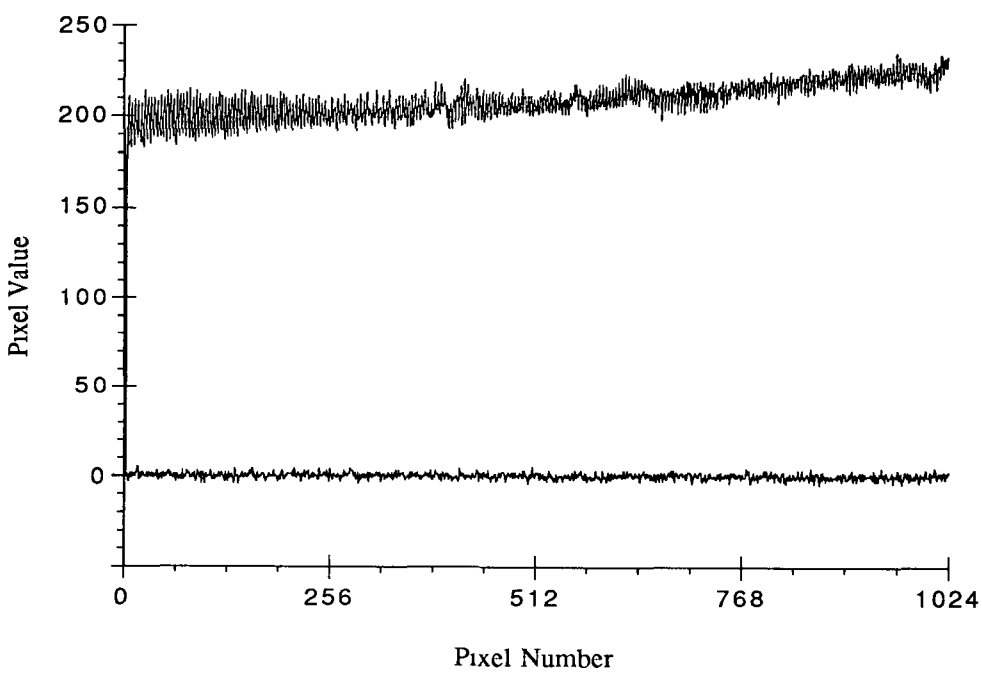


Figure 3.2b: Plot showing noise at exposure time of 240ms
and base level noise of two subtracted, 240ms scans

As expected the average pixel value increases linearly with increasing exposure time. The intercept value of 45 counts indicates a DC offset output from the video amplifier. Although this value is less than 0.2% of saturation counts, it could lead to errors in photoabsorption experiments for low values of absorbed intensity I . It is also important for measuring emission spectra where the signal could be mistaken for a low level continuum. The procedure was repeated for the same exposure times and the two corresponding exposure time scans were subtracted to provide an indicator of the random noise level present in the scan. This level centres around zero at all exposure times and indicates an almost complete dominance by FPN, since subtraction of the two yields an almost flat signal. This feature is shown in figure 3.2b.

The variation of pixel noise as a function of number of scans averaged (1, 2, 4, 9, 16, 25, 64, 100) was obtained at a fixed exposure time of 280ms and an operating temperature of 5°C. A plot of these data is shown in figure 3.3. The plot shows a nearly perfect correlation across all the scans which again indicates an almost complete dominance by FPN.

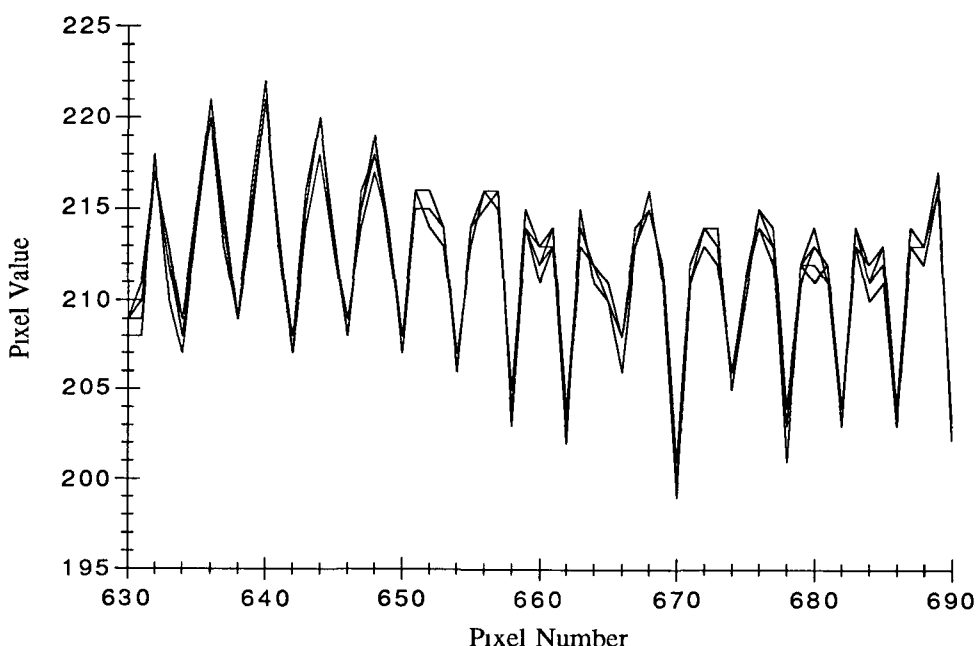


Figure 3.3: Plot of Noise Vs Number of Scans at ET=280ms and T=5C

3.2 Single Vs Multi-Laser Shot Averaged Spectra.

3.2.1 Introduction

A number of emission spectra of carbon laser produced plasmas are presented in figures 3.4a, 3.4b, 3.4c. These figures show single shot spectra of carbon at the 450Å, 1200Å, 1950Å wavelength regions. The spectra were all taken under the same experimental conditions. In all cases the spectral region covered by the 25mm extent of the PDA was 215Å. At longer wavelengths the spectra are dominated by higher orders of CII, III and CIV lines.

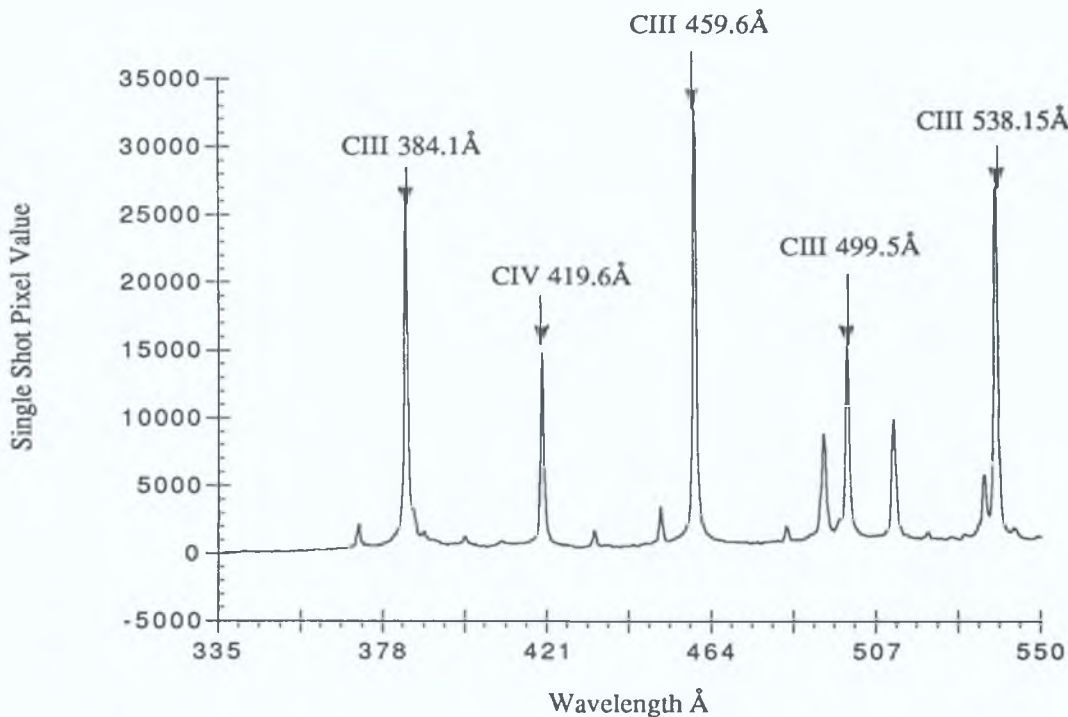


Figure 3.4a:PDA Output Spectrum of carbon LPP using the Acton 1m set at 450Å

3.2.2 Analysis of Spectra Obtained

Figure 3.4a shows a region where the spectrum is most intense with the y-axis almost reaching the saturation count value of 32768 and contains lines of predominantly CIII in first order. The noise visible on this plot is small with very little random modulation at the base line. Figure 3.4b indicates a poorer SNR due to the lower pixel values in the spectrum. The spectrum contains lines of CIV, CIII and CII in first and second order. The Lyman- α line of Hydrogen (1215.67Å) is present in this spectrum.

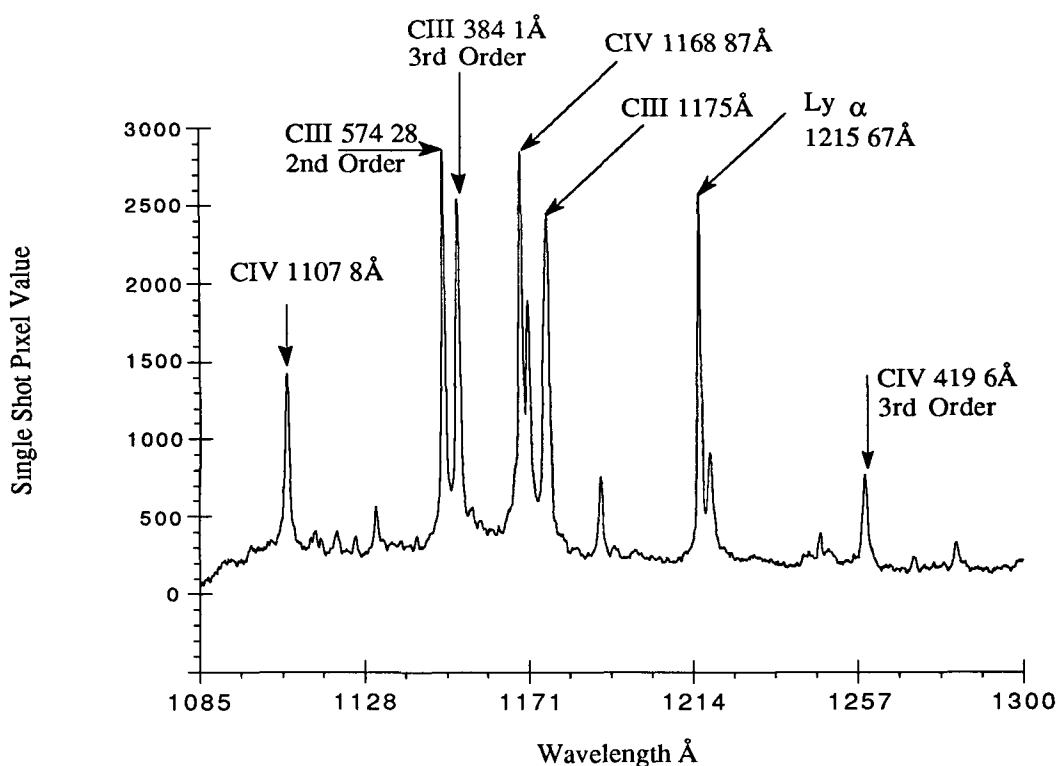


Figure 3.4b:PDA Output Spectrum of carbon LPP using the Acton 1m set at 1200 \AA

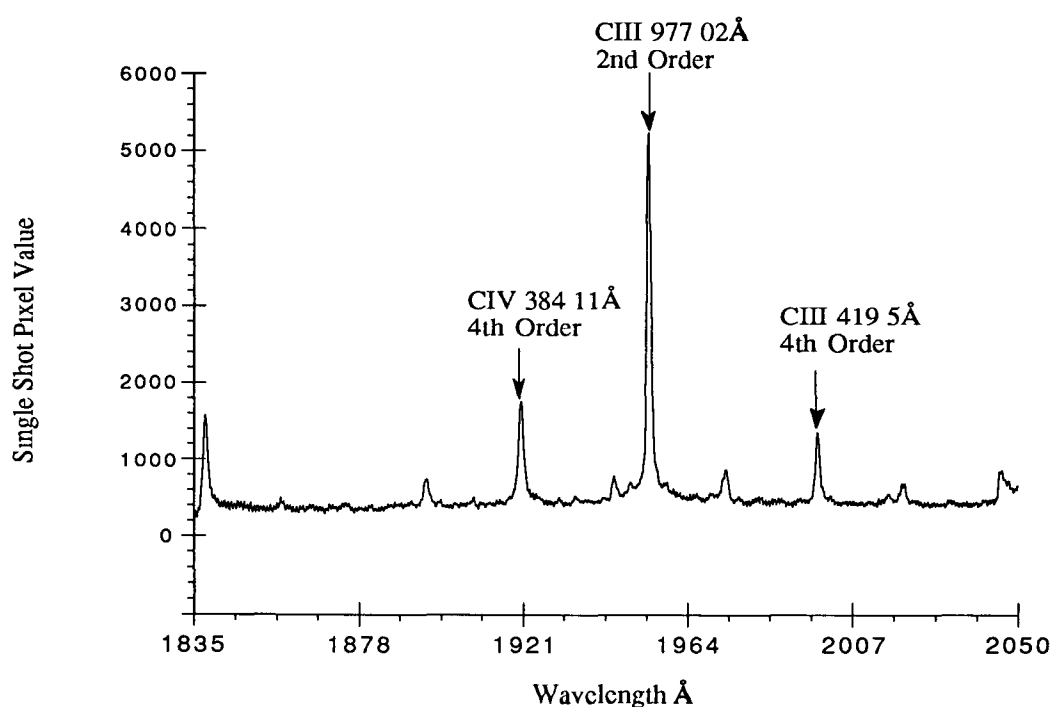


Figure 3.4c: PDA Output Spectrum of carbon LPP using the Acton 1m set at 1950 \AA

Figure 3 4c is dominated by the CIII line at 977 02Å with weaker lines of CIV, CIII and CII in third and fourth order

The strongest observed carbon plasma emission lines taken from the Acton VM-521 are tabulated for the CII, CIII and CIV species in tables 3 1, 3 2 and 3.3 The identification of these lines is obtained from Kelly's tables [33] I have given the wavelengths a relative intensity value in line with Kelly's typical practice, i.e. the highest relative intensity spectral line in the complete spectrum is equivalent to 1000 and other lines in the spectrum are referenced to this Comparison of relative intensity values show some discrepancies which are attributed to experimental differences in

- 1 Plasma Conditions
- 2 Lack of consistency in assignment of intensities in the papers cited by Kelly for compilation of carbon spectra below 2000Å
- 3 Different sources used to record spectra cited in Kelly's tables
- 4 Response curve of detection equipment
- 5 Spectrometer characteristics/efficiencies

The strongest observed line in the carbon emission spectra occurred for the 2s2p->2s3d transition of CIII at 459 6Å The response curve of the complete system shows an efficiency peak around the wavelength range of 400-600Å The maximum efficiency of the 1200 g/mm grating peaks around 800Å, however the discrepancy may be attributed to the plasma conditions (temperature, densities, etc) existing during the scan period of the PDA and also the detection efficiency of the MCP/PDA combination From the above considerations it would appear that the dominant ion stage is C²⁺ Referring to figure 2 of Colombant and Tonon [42] we can estimate a plasma electron temperature in the range 10-30eV assuming Collisional-Radiative equilibrium pertains to the plasma.

Wavelength (Angstroms)	Rel Int.	Int 1m	Transitions	Terms	$J \rightarrow J'$
594 8000	600	250	2s ² 2p-4d	² P- ² D	1/2-3/2
595 2019	700				3/2-5/2
595 0245	70				3/2-3/2
651 211	150	150	2s2p ² -2s2p3d	⁴ P- ⁴ D	1/2-3/2
651 234	150				1/2-1/2
651 269	400				3/2-5/2
651 304	300				3/2-3/2
651 345	800				5/2-7/2
651 389	150				5/2-5/2
687 0526	800	550	2s ² 2p-3d	² P ^o - ² D	1/2-3/2
687 3453	1000				3/2-5/2
687 3521	110				3/2-3/2
799 660	500	180	2s2p ² -2s2p3d	² D- ² F	5/2-7/2
799 928	25				5/2-5/2
799 944	350				3/2-5/2
806 384	500	150	2s2p ² -2s2p3s	⁴ P- ⁴ P	3/2-5/2
806 533	200				1/2-3/2
806 568	500				5/2-5/2
806 676	250				3/2-3/2
806 686	150				1/2-1/2
806 830	300				3/2-1/2
806 860	300				5/2-3/2
858 0918	500	200	2s ² 2p-3s	² P- ² S	1/2-1/2
858 5590	900				3/2-1/2
903 6235	600	150	2s ² 2p-2s2p ²	² P- ² P	1/2-3/2
903 9616	800				1/2-1/2
904 1416	1000				3/2-3/2
904 4801	600				3/2-1/2
1036 3367	800	100	2s ² 2p-2s2p	² P- ² S	1/2-1/2
1037 0182	1000				3/2-1/2

Table 3.1: Strongest Observed carbon II Lines in the Spectra obtained from Acton 1m

Wavelength (Angstroms)	Int. (kelly)	Int. 1m	Transition	Terms	J + J
459 462	900	1000	2s2p-2s3d	3P-3D	0-1
459 521	950		"		1-2
459 633	1000		"		2-3
460 0487	800		2s2p-2p3p	1P-1P	1-1
493 341	500	250	2p ² -2p3d	3P-3P	0-1
493.364	500		"		1-0
493 396	500		"		1-1
493 464	500		"		1-2
493 519	500		"		2-1
493 587	700		"		2-2
499 425	700	450	2p ² -2p3d	3P-3D	0-1
499.462	800		"		1-2
499 530	900		"		2-3
499 583	700		"		2-2
511 5225	1000	300	2p ² -2p3d	1D-1F	2-3
535 2885	850	200	2p ² -2p3d	1D- 1D	
538 0801	900	850	2s2p-2s3s	3P-3S	0-1
538 1487	950		"		1-1
538 3120	1000		"		2-1
574 2089	1000	750	2s2p-2s3p	3P-1D	1-2
585 261	600	550	2p ² -2p3s	3P-3P	1-2
585 417	800				2-2
585 496	500				1-1
585 608	600				1-0
585 666	600				2-1
977 020	1000	350	2s ² -2s2p	1S-1P	0-1

1174 933	800	100	2s2p-2p ²	3P-3P	1-2
1175 263	700		"		0-1
1175 590	600		"		1-1
1175 711	1000		"		2-2
1175 987	700		"		1-0
1176 370	800		"		2-1

Table 3.2: Strongest Observed carbon III lines from 1m Acton

Wavelength (Angstroms)	Int. Rel.	Int. 1m	Transition	Terms	$j - j'$
384 032	800	800	1s ² 2p-1s ² 3d	² P- ² D	¹ / ₂ - ³ / ₂
384 178	850		1s ² 2p-1s ² 3d	² P- ² D	³ / ₂ - ⁵ / ₂
419 525	650	450	1s ² 2p-1s ² 3s	² P- ² S	¹ / ₂ - ¹ / ₂
419 714	700				³ / ₂ - ¹ / ₂

Table 3.3: Strongest Observed carbon IV emission lines in spectra from Acton 1m

3.3 Spectral Orders in the carbon Emission Plasma.

3.3.1 Introduction

According to the theory of the concave diffraction grating, each primary diffracted wavelength is also present at a number of higher wavelength positions. These positions are located at an integer multiple (called the order number) of the primary wavelength (first order). For example a first order wavelength of 459.6 Å will also be visible at 919.2 Å, 1378.8 Å etc. The reciprocal linear dispersion increases with increasing order number (m) and this improves the resolving power of the spectrometer with respect to the first order performance. However the grating efficiency decreases with order number (m) and thus the intensity of these higher order lines may be significantly reduced.

3.3.2 Spectral Order Analysis

The efficiency of the grating used in this thesis is a maximum at 800 Å (blaze wavelength) in first order. This work has identified lines up to fifth order. A number of lines are presented in table 3.4 which traces their relative intensity up to fifth order. The more gradual fall-off in intensity of the higher orders of the CIV line may be due to the fact that 384 Å is almost co-incident with $\lambda_B / 2$.

Wavelength (Angstroms)	Intensity (Kelly)	Intensity m=1	Intensity m=2	Intensity m=3	Intensity m=4	Intensity m=5
CIII						
459.462	900	1000	200	25	-	-
459.521	950					
459.633	1000					
460.049	800					
CIV						
384.032	800	800	550	75	50	15
384.178	850					

Table 3.4: Unresolved carbon Emission lines observed up to fifth order from Acton 1m normal incidence multichannel spectrometer

Figure 3 5a and Figure 3 5b show first and second order lines of two CIII lines at 493 4Å and 499 4Å In Figure 3 5a the pixel separation of the two lines is 29 which corresponds to a wavelength difference of 6 02Å, which is in close agreement with the physical wavelength difference of 6 0Å

In second order, Figure 3 5b the two lines are separated by 57 pixels (i.e. $1/(m=2)$ times the dispersion/pixel) which corresponds to 5 93Å The CIII line at 492 65Å which was unresolved in first order is now resolved in second order and the intensity of the lines in first and second order are reduced by a factor of approximately 7.

The *pixel* halfwidth in both first and second order of these two lines are identical which means that the FWHM is halved between first and second order and thus the resolution of the second order lines is doubled In figure 3 5a the 493 4Å has a FWHM of 1 25Å ($6 \times 0.2075\text{Å}$) and the 499 4Å line has a FWHM of 1 04Å

It is obvious from this analysis that the lines have been instrumentally broadened during measurement From the analysis of the carbon spectra from the Acton VM521, it is estimated that a Gaussian profile similar to that of the CIII line at 499 4Å with a FWHM of 5 pixels best approximates the instrument function This is justified by the fact that at successively higher orders the FWHM does not reduce below 5 pixels even though the dispersion is halving with each higher order This value is in quite good agreement with the normal incidence 512 channel spectrometer used in [34] where for a 2400g/mm and 2m focal length the instrument function has a surprisingly poor width of 1 2Å

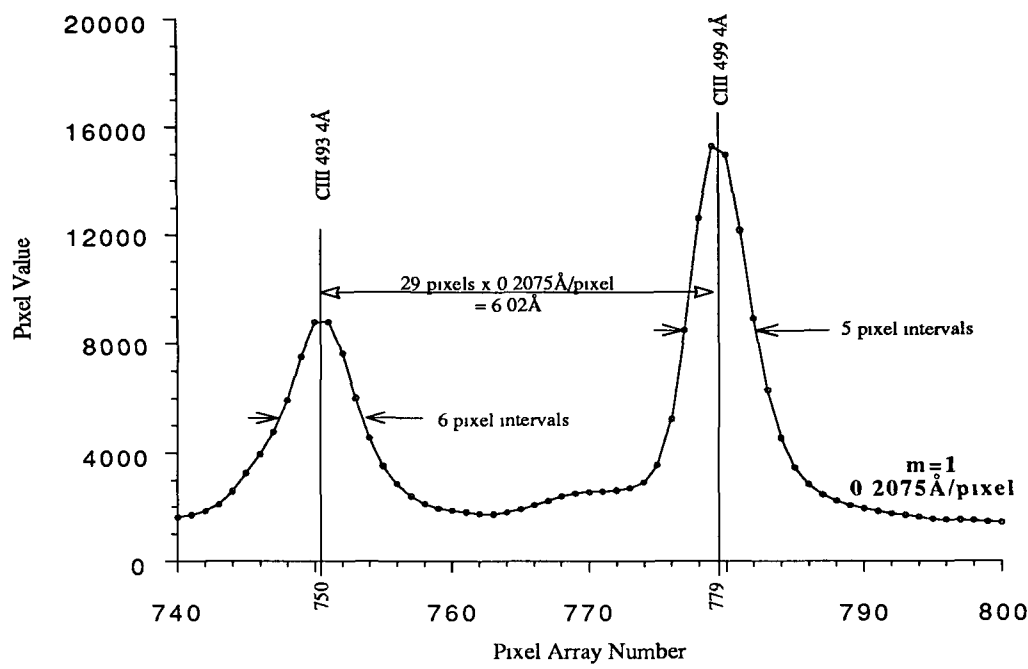


Figure 3.5a: Two lines of CIII at 493 and 499Å in first order

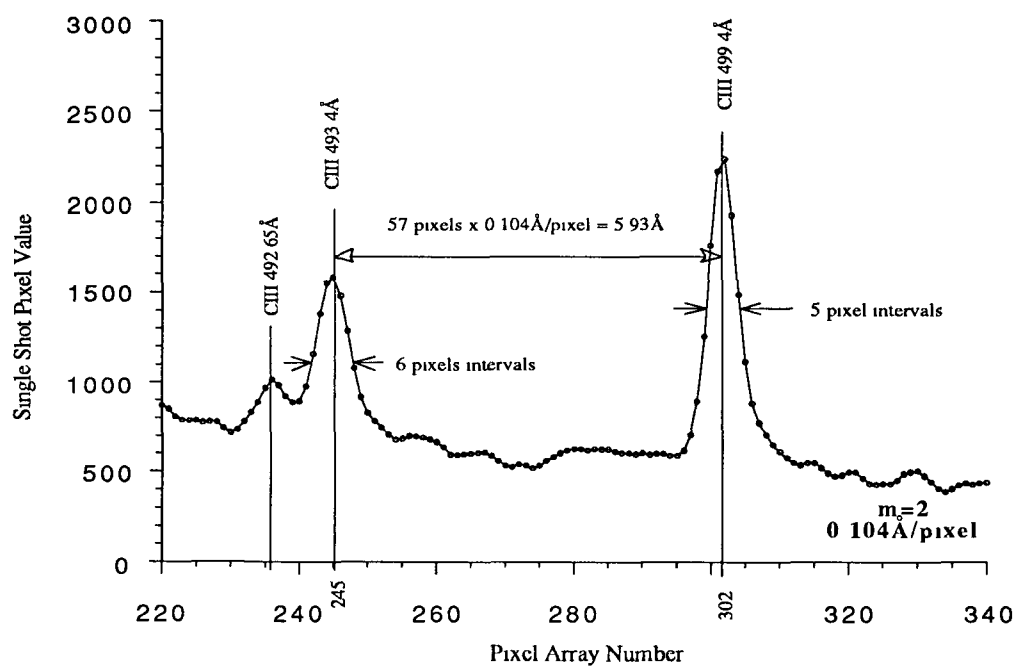


Figure 3.5b: Two lines of CIII at 493 and 499Å in Second order

3.4 Comparison of carbon Spectra from Acton 1m and McPherson 2.2m Vacuum Spectrometers.

3.4.1 Introduction

In order to compare the current performance of the Acton VM-521 VUV multichannel spectrometer with an existing McPherson 2.2m grazing incidence UV (XUV) spectrometer spectra of laser produced carbon plasmas were recorded within the 350Å-450Å overlap region

3.4.2 Spectral Wavelength Coverage

The McPherson grazing incidence spectrometer covers the wavelength range from 40-500Å, while the Acton normal incidence has a corresponding range of 300-3250Å. Figure 3.6 presents a comparison of the carbon spectra from both instruments. The carbon lines at 384.1Å, 419.6Å and 459.6Å are exactly co-incident between spectra

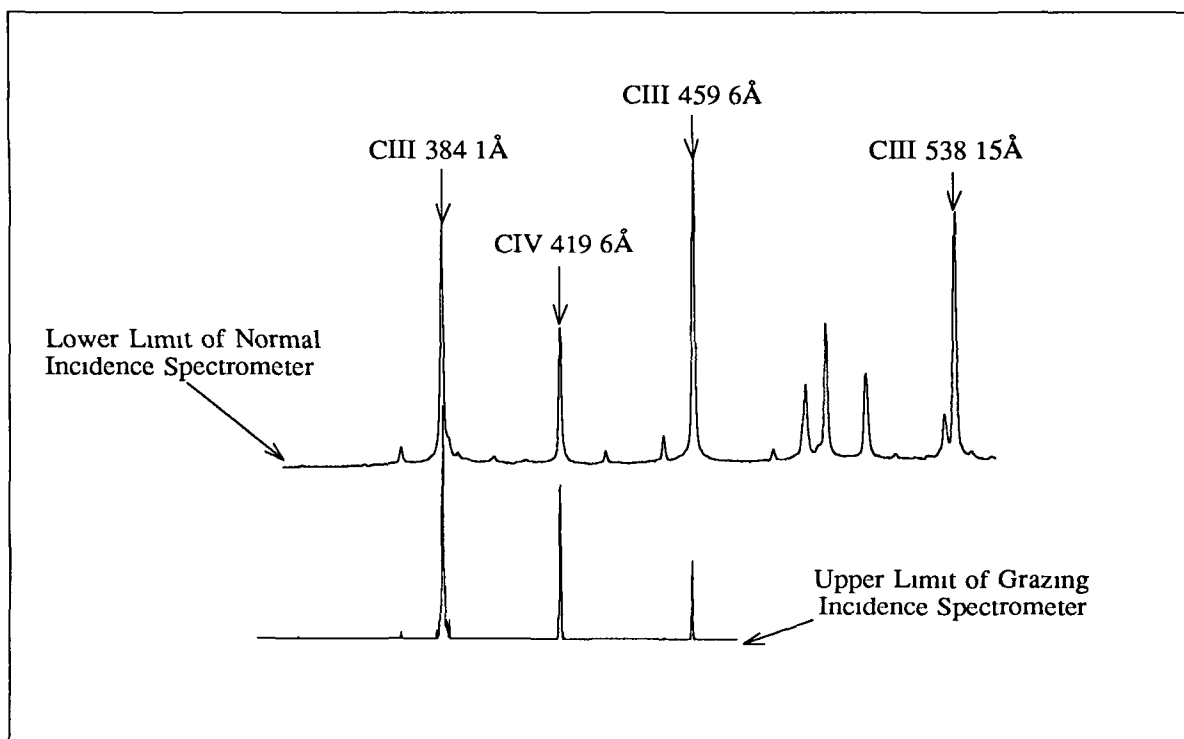


Figure 3.6: Overlap in Wavelength Ranges between Acton 1m and McPherson 2.2m

The 2.2m grazing incidence instrument has a higher dispersion and narrower instrument function (3 pixels) than the Acton 1m instrument. It is also less sensitive to higher orders. However the Acton instrument is clearly a superior light gathering instrument with a con-comitant effect on signal to noise ratio in the spectra shown

3.4.3 Resolution Performance.

The CIV line at 419.53Å was measured in grazing incidence and compared to the same line as measured by the Acton normal incidence spectrometer. Figure 3.7 and 3.8 show the line taken from both sources in up to third order in the case of the Acton spectra. The FWHM of this line in grazing incidence is 0.41Å and is significantly narrower than the first order line from the Acton which is measured at 1.26Å. This is due to the higher dispersion of the McPherson spectrometer (0.046Å/pixel) than that of the Acton (0.2075Å/pixel in first order). In third order the Acton approaches a resolution comparable to that of the McPherson (0.069Å/pixel) with a FWHM of 0.48Å. The Acton spectra however show an intensity advantage over the McPherson and is comparable even in third order. Hence use of the Acton 1m normal incidence in higher orders is an efficient means of obtaining moderate to high resolution spectra when required.

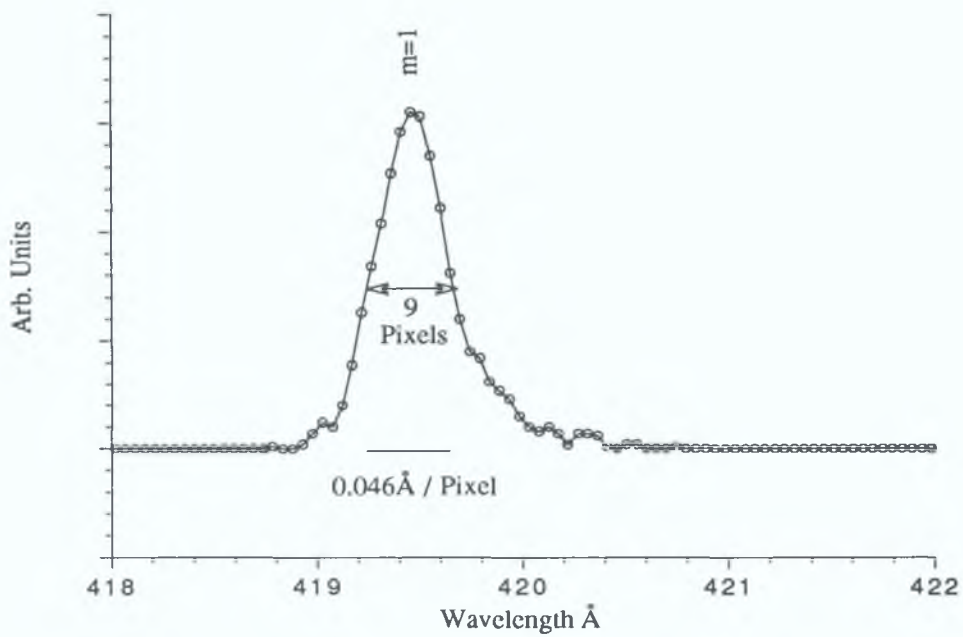


Figure 3.7: CIV line taken from Polyethylene spectrum
using McPherson 2.2m Spectrometer

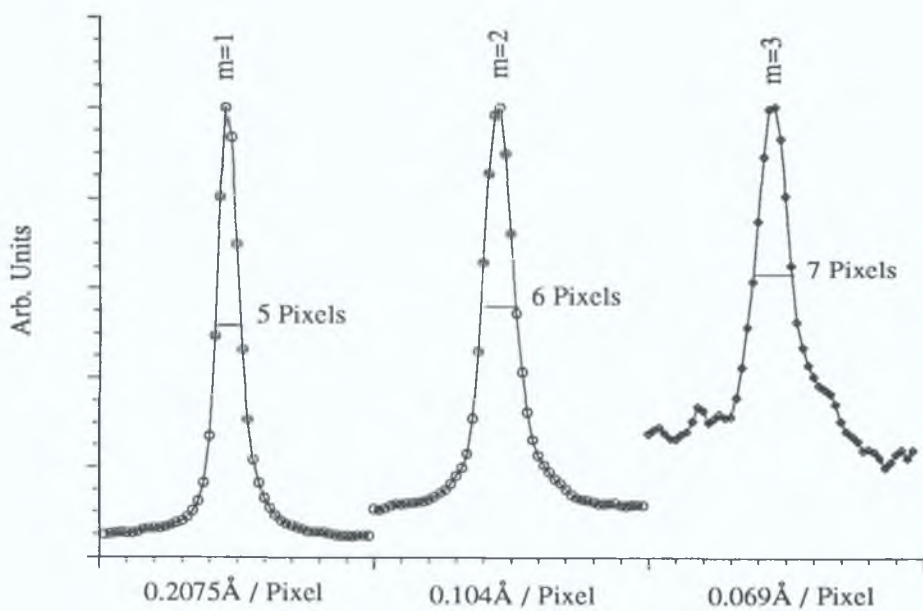


Figure 3.8: CIV line taken from Polyethylene spectrum in first, second and third order
using the Acton 1m Spectrometer.

3.5 Spectral Resolution Enhancement using Deconvolution Techniques.

3.5.1 Introduction.

The discussion provided in the preceding sections reveals that the spectra recorded with the Acton VM-521 normal incidence spectrometer are blurred during measurement. This blurring results in overlapping spectral lines and thus reduced resolution. The Acton spectrometer blurring is quantified by recording a delta function (single narrow peak line from a known emission spectrum). This recorded line is called the Instrument Function of the spectrometer and characterises how each line in a spectrum will be distorted.

It is possible to reconstruct a better resolved spectrum using a deconvolution method to cancel at least in part, the blurring caused by the instrument function of the Acton spectrometer. The effect of the instrument function is described mathematically as the convolution of the true spectrum $O(x)$ with the instrument function $S(x)$. The deconvolution method may be stated as follows: there is a data set $\{y_1, y_2 \dots y_n\}$ composed of a set of peaks and some noise recorded by the Acton normal incidence multichannel spectrometer, which is equivalent to

$$y_i = (O \otimes S)_i + n_i \quad (3.5)$$

where $\{s_1, s_2 \dots s_n\}$ describes the shapes of the peaks, $\{o_1, o_2 \dots o_n\}$ is a more highly resolved spectrum, \otimes denotes convolution and n_i are the noise fluctuations in the system. The Instrument function s represents different physical processes in different systems. The more highly resolved spectrum is often regarded as a set of delta functions which are positioned at the band centres and which have heights proportional to the areas of the respective bands. The mathematical problem therefore is to find the set $\{o_1, o_2 \dots o_n\}$.

3.5.2 Maximum Likelihood - vs - Fourier Deconvolution.

Maximum Likelihood and Fourier deconvolution restoration are two different methods of solving the same problem. Fourier deconvolution estimates a more highly resolved spectrum in this way: Ignore the noise present in the system and solve the equation:

$$y_i = (O \otimes S)_i \quad (3.6)$$

The solution is obtained in the Fourier domain by dividing the Fourier transform of the data $\{y_1, y_2 \dots y_n\}$, by the transform of the instrument function peak shape $\{s_1, s_2 \dots s_n\}$. The

resulting inverse transform of the quotient is the estimate of $\{o_1, o_2, \dots, o_n\}$. This is equivalent to

$$o'(x) = F[O(v)]^{-1} = F\left[\frac{Y(v)}{S(v)}\right]^{-1} \quad (37)$$

where $O(v)$, $Y(v)$ and $S(v)$ are the Fourier transforms of the data sets $\{o_1, o_2, \dots, o_n\}$, $\{y_1, y_2, \dots, y_n\}$, and $\{s_1, s_2, \dots, s_n\}$, $F[\cdot]^{-1}$ is the inverse Fourier transform and $o'(x)$ is the more highly resolved spectrum [43]

This method ignores the noise which is present in the spectrum and which dominates at large Fourier frequencies. Further this noise is now amplified in the solution $\{o'_1, o'_2, \dots, o'_n\}$. Without filtering the high frequency components of $O(v)$ the inverse transform produces ringing and negative intensities in $\{o'_1, o'_2, \dots, o'_n\}$. Fourier deconvolution becomes the art of finding the most pleasing filter (Gaussian, triangular, square, etc.) which gives the best resolution and with the minimum of noise and image distortion. The disadvantage of this deconvolution technique is that depending on the filter and filter parameters used, different results are obtained for the same set of initial data and the validity of the result may be suspect [35].

The Maximum Likelihood method differs from Fourier deconvolution because it acknowledges the fact that the data have noise present and that many inverse solutions are possible within the noise limits. Maximum Likelihood works by constructing a probability function which assigns a probability to every physical outcome of a particular experiment. The object spectrum which has the highest probability of giving us the observed data set is then chosen. The most probable spectrum is bound by a set of system constraints, which includes everything the system experimenter knows about the system such as

- 1) The instrument function of the spectrometer
- 2) The Signal-to-Noise ratio
- 3) Type of noise present (Gaussian, Poisson)
- 4) Total energy is always conserved
- 5) Spectrum Line Location Probabilities

The equations needed for spectral restoration using the Maximum Likelihood technique are as follows

For Gaussian noise , the probability that y_i is observed for input o_i is

$$p(y_1, \dots, y_n | o_1, \dots, o_n) = \prod_{i=1}^n \frac{1}{\sqrt{(2\pi)\sigma_i}} \exp\left[-\frac{(y_i - (o \otimes s)_i)^2}{2\sigma_i^2}\right] \quad (3.8)$$

For Poisson noise the corresponding expression is

$$p(y_1, \dots, y_n | o_1, \dots, o_n) = \prod_{i=1}^n \frac{(o \otimes s)_i^{y_i} e^{-(o \otimes s)_i}}{y_i!} \quad (3.9)$$

The Maximum likelihood method says that p must be maximised This maximisation is done under our set of constraints, an important one of which is our knowledge of the peakshapes We assume that the object function $\{o_1, o_2, \dots, o_n\}$ is composed of many individual peaks of known shape s and that it is positive everywhere

The Maximum Likelihood method has the following advantages over the Fourier Deconvolution method

- It provides the maximum amount of resolution enhancement possible, consistent with the given noise in the data
- It preserves the areas of the peaks
- It does not give negative intensities
- It is objective All observers will obtain the same result under the same set of constraints (instrument function, noise statistics)

3.5.3 Instrument Function.

The instrument function for the Acton 1m normal incidence spectrometer has been referred to in section 3.3.2 It can be estimated from the following observations The pixel FWHM of any observed spectral line is not less than five pixels wide The CIV line at 419.53 Å does not reduce below five pixels at successively higher orders even though the dispersion is improving with each higher order This indicates that the line is intrinsically broadened by the measuring instrument and this line represents the maximum resolving power in first order Further since the line is 5 pixels FWHM, the Nyquist minimum spatial sampling frequency criterion (i.e. $f_{\text{samp}} > 1 / (2 \times \text{pixel widths})$) is more than satisfied Since this is a relatively isolated line in the spectrum we may use

this as the basis of our instrument function. The Maximum Likelihood software package SSRes (contained in SpectraCalc™) is capable of taking this range of points and curve fitting the instrument function. The curve is approximately Gaussian. This fitted curve is now used as the data range {s₁,s₂,...s_n} in our maximum likelihood ‘restoration’ process. Figure 3.9 shows the original CIV line taken from the spectrum which was used to generate the fitted Gaussian instrument function.

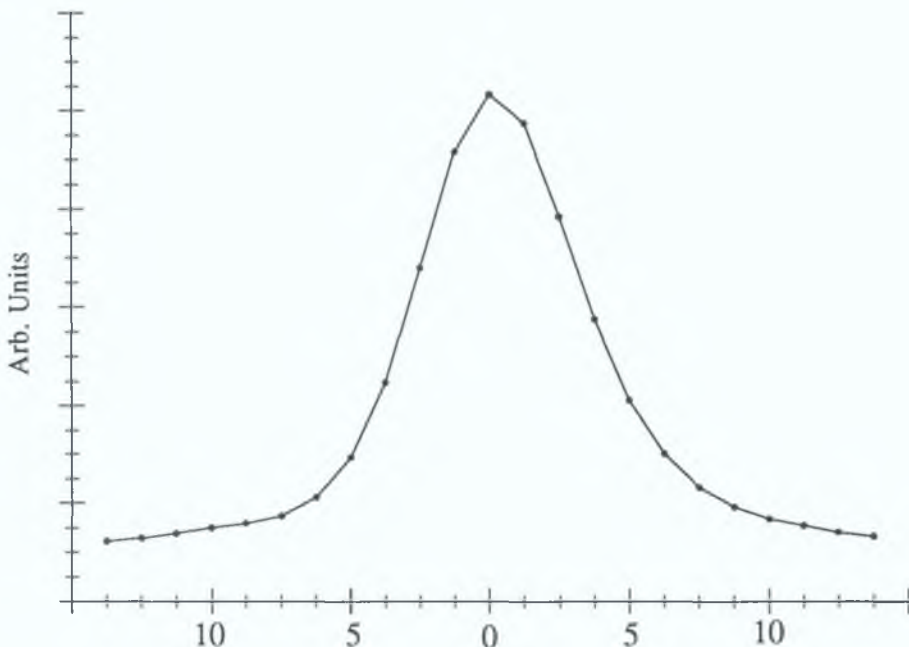


Figure 3.9: Instrument Function of Acton VM-521 Normal Incidence Spectrometer.

3.5.4 Deconvolved carbon Spectra.

Resolution enhancement was performed on a carbon plasma scan centred around the 770Å region. The SNR value of the spectrum was estimated by dividing the average pixel value in the scan by the average noise value for an integration time of 30ms (figure 3.2). It should be noted that under illumination the true SNR will be somewhat poorer. The resolution before deconvolution was > 500 as evidenced by the two CV lines at 748.43Å and 749.66Å which are just barely resolved. Figure 3.10 shows the resultant resolution enhancement after 10 iterations using the Maximum Likelihood program. The resolution of the new spectrum is > 1000, which is within the expectations of the Maximum Likelihood program (improvement factor of 2-3). Clearly this technique which can also be used together with the resolution improvement of higher order lines is

a very useful tool in increasing the resolution of a spectral data set. However, a low density low temperature narrow line light source (e.g., ECR) would be required to provide a more ideal delta function input to obtain a 'good' estimate of the instrument.

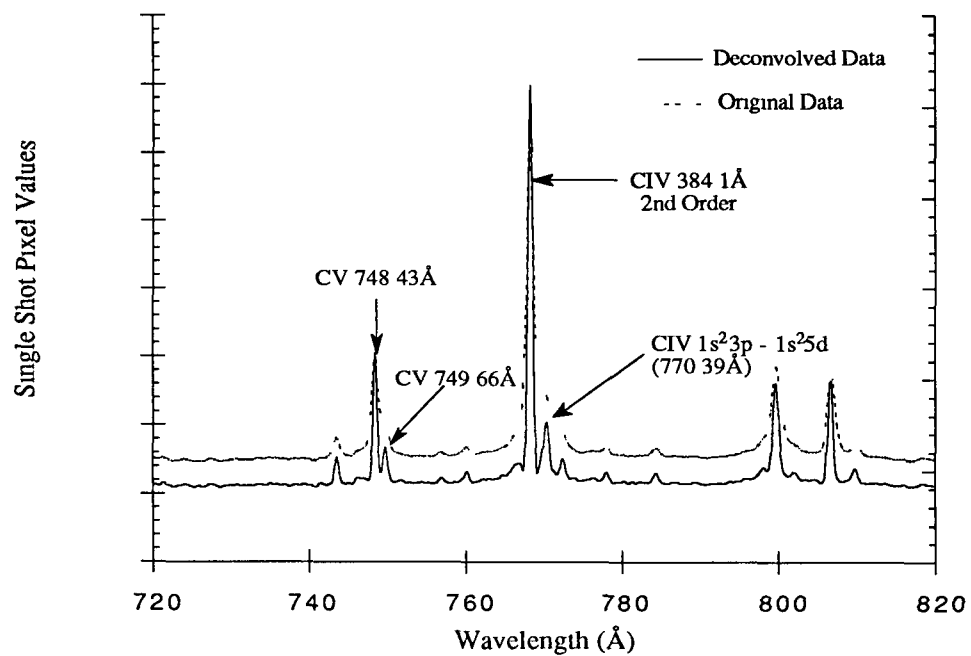


Figure 3.10: Deconvolved carbon Spectra using Maximum Likelihood Technique

3.6 Complete Carbon and Tungsten Spectra.

3.6.1 Introduction

A complete set of spectral data has been obtained for carbon and tungsten. Each data set has been further overlapped and pasted to a larger spectral data set which includes all the data values in the range 300-2000Å for carbon and 300-1200Å for tungsten. Above 1200Å the tungsten spectrum is essentially a featureless continuum.

3.6.2 Spectral Analysis.

In figures 3.11 and 3.12 the spectrum of a line dominated carbon plasma and a predominately continuum like tungsten plasma in the wavelength ranges 300 to 2000Å and 300 to 1200Å respectively are shown. Both spectra demonstrate the wavelength extent of the instrument and also its peak response in the 500 to 800Å range. Although blazed for 800Å, the plasma brightness below 800 Å results in an apparent shift of peak response. Note also the sharp fall off in the grating response as evidenced by the drop in intensity of the tungsten spectrum below 400 Å where the plasma is brighter still. The tungsten spectrum is (somewhat unexpectedly) overlaid by strong lines in the 400 to 750 Å range which have not yet been identified. Note also the lower peak counts (under exactly the same plasma conditions) of the tungsten versus carbon spectrum as the absorbed laser energy is spread over broadband VUV / VUV radiative emission.

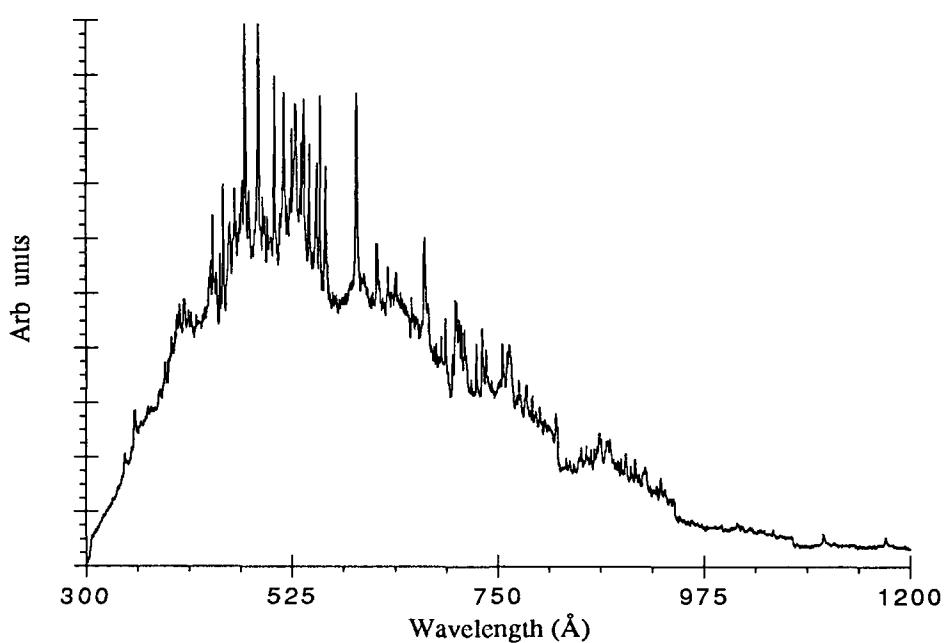


Figure 3.11: Tungsten Spectra over range 300-1350Å

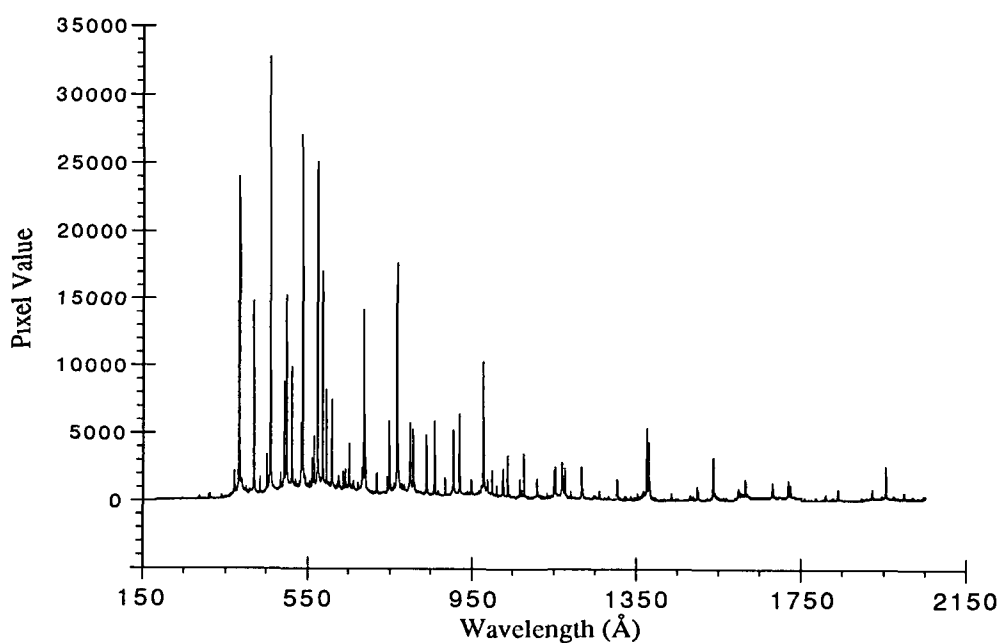


Figure 3.12: carbon Spectra over range 300 - 2000Å

Chapter 4

Conclusions

3

3

3

4.0 Summary Conclusions

The development of a vacuum-UV MultiChannel Spectrometer for laser plasma spectroscopy has been described. The spectrometer has been modified for the attachment of a VUV OMA system and target chamber. A software package to control the experiment has also been developed as part of this thesis. The normal incidence spectrometer has been shown to have the following main characteristics.

1. Single shot sensitivity
2. An operating wavelength of $> 300\text{\AA}$ to $< 3000\text{\AA}$.
3. A single CEMA capture range of approximately 200\AA with a 1200 g/mm^{-1} grating.
4. A resolution better than 1.5\AA before deconvolution.
5. A CEMA/PDA scan repetition rate of up to 30Hz.

It has been demonstrated that a resolution improvement of 2-3 may be obtained using deconvolution. However the sensitivity of the reconstructed line profiles to the instrument function shape requires caution in the use of any restored spectra for any analysis other than determination of line positions.

4.2 Future Work Considerations

A number of improvements still remain to be made and are summarised here. The instrument suffers from high reflectivity in higher orders and hence will require the use of thin film solid filters alleviating order sorting problems. A special vacuum isolating chamber will be required to protect such filters from plasma blow off. A normal incidence coupling optic could be used to increase the plasma light gathering power of the instrument and hence improve the OMA system SNR. As of now it is not possible to use such an optic to fill the grating to the optimum width of approximately 9.5 cm, (Section 1.3.5) due to the presence of a GCA for differential pressure maintenance (Section 2.5.1). However a vacuum seal based on an O ring slit seal (O' Sullivan [51]) would alleviate this problem.

Early measurements of VUV continuum emission [4] show that the duration increases with wavelength. In fact in the VUV, the duration of the continuum can be up to 100's of nanoseconds. Further, in dual laser plasma photoabsorption experiments,

many sample plasmas (of even singly and doubly ionised species) will emit in the VUV spectral range. Hence, in order to obtain good time resolution and also reject at least part of the front plasma emission, it will be necessary to gate the MCP on the CEMA. This should not be a problem as the manufacturers quotes a 5ns minimum gate width time.

A great deal of work remains to be done on the area of determination of instrument functions for the complete setup of the one meter normal incidence OMA system. Initial exposure with multi-line low pressure rare gas light sources are an obvious starting point. ECR light sources are known to produce narrow intense emission lines which could prove an ideal if somewhat expensive option.

A resolution of approximately 0.5 Å (~2.5 pixels FWHM) can only be obtained after deconvolution. Despite efforts at optimisation of the ARC 1m normal incidence spectrometer optics, a FWHM of only 5 pixels has been obtained. This degradation in resolution cannot confidently be associated entirely with the CEMA/OMA system itself, although extensive efforts at refocussing of the 1m instrument has failed to improve this figure.

Finally, it is proposed that the instrument be coupled with the McPherson 2.2m grazing incidence multi-channel spectrometer onto a single target chamber to form a complete single shot laser plasma spectroscopic system covering the 3 to 300 eV photon energy range.

References

- [1] Carroll P K and Kennedy E T , Contemp Phys , **22** , 1, 61-96, (1981)
- [2] Radziemski Leon J , Laser-Induced Plasmas and Applications, Marcel Dekker Inc (1989)
- [3] Costello J, Mosnier JP, Kennedy ET, Carroll PK and O'Sullivan G, Physica Scripta ,**T34**, 77-92, (1991)
- [4] Carroll P K , Kennedy ET and O'Sullivan G, Applied Optics, **19** (1980)
- [5] Carroll PK and O'Sullivan G, SPIE, **1503**, 415-427, (1991)
- [6] O'Sullivan G, J Phys B, **16** , 3291-3304, (1983)
- [7] O'Sullivan G, Carroll PK, McIlrath TJ and Ginter ML, Applied Optics, **20** , 3043-3046, (1981)
- [8] Eldmann K, Key MH and Sigel R, Journal of Applied Physics, **47**, 2403 - 2413, (1976)
- [9] Dewhurst R J, Khan MA and Pert GJ, J Phys B , **8** , 2301-2310, (1975)
- [10] Bridges JM, Cromer CL and McIlrath TJ, Applied Optics, **25**, 2208-2214, (1986)
- [11] Heckenamp CH, Heinzmann U, Schonhense G, Burgess DD, Thorne AP and Wheaton JEG, J Phys D , **14** , L203-L206, (1981)
- [12] Breton C and Papoulier R, J Opt Soc Am, **63**, 1225-1232, (1973)
- [13] Irons F E, McWhirter RWP and Peacock NJ , J Phys B, **5**, 1975-1987, (1972)
- [14] Irons F E and Peacock NJ, J Phys B, **7**, 2084-99, (1974)
- [15] McClung FJ and Hellwarth J, J Appl Phys, **33** , 828-829, (1962)
- [16] Linlor WI, Appl Phys Lett, **3** , 210-11, (1963)

- [17] Isenor NR, Can J Phys , **42** , 1413-16, (1964)
- [18] Bazov NG, Boika VA, Dement'ev VA, Krokhin ON and Sklizkov GV, Sov Phys JETP, **24** , 659-66, (1967)
- [19] Bazov NG, Boika VA, Grubkov VA, Zakharov SM, Krokhin ON and Sklizkov GV, Sov Phys JETP, **34** , 81-4, (1972)
- [20] Koopman DW, Phys Fluid, **14**, 1707-16, (1971)
- [21] Boland BC, Irons FE, McWhirter RWP, J. Phys B, **1**, 1180-91, (1968)
- [22] Boland BC and Irons FE, VIII Int Conf on phenomena in ionized gases, 452, (1967)
- [23] Griffin WG and Schulter J, Phys Lett , **26A**, 241-242, (1968)
- [24] Namioka T, J Opt Soc Am, **49** , (1959)
- [25] Namioka T, J Opt. Soc Am, **51** , 4-16, (1961)
- [26] Beutler H G, J Opt Soc Am ,**35**, 311-350, (1945)
- [27] Samson J A R, '*Vacuum UltraViolet Spectroscopy*', Wiley (1967)
- [28] Vodar B, Revue D'Optique, **21**, 97 - 113, (1942)
- [29] Robin S, Journal de Physique, **10** , 531-532, (1953)
- [30] McPherson Corporation, 1m Monochromator Model 225
- [31] Cromer CL, Bridges JM, Roberts JR and Lucatarto TB, Appl Optics, **24**, 2996-3001, (1985)
- [32] Simpson RW, Rev. SCI. Instruments, **50**, 730-735,(1979)
- [33] Kelly RL, J. of Phys & Chem Reference Data, Vol 16,(1987)

- [34] Jannitti E, Mazzoni M, Nicolosi P, Tondello G and Yongchang W, *J Opt Soc Am*, **2**, 1078-1084, (1985)
- [35] Doyle B, BSc Thesis , DCU, 1993 (unpublished)
- [36] Pouey M and Romand J, *Revue D'Optique*, **44**, 445-458, (1965)
- [37] Orth FB, Ueda K, McIlrath TJ and Ginter ML, *Applied Optics*, **25**, 2215-2217, (1986)
- [38] Wilza J, *Nucl. Inst and Meths*, **162**, 587-, (1979)
- [39] Galanti M and Peacock NJ, *J Phys B*, **8**, 2427-2447, (1975)
- [40] Jacques C , Knystautas EJ and Drouin R, *Can J Phys* , **58** , 1093-1098, (1980)
- [41] Feldman U, Brown CJ, Doschek GA and Moore CE, rosenburg FD, *J Opt Soc Am* , **66**, 853-859, (1976)
- [42] Colombant D and Tonon G F, *J Appl Phys* , **44** , 3524-3537, (1973)
- [43] Michaelian KH and Friesen WI, *Appl Spect* , **42**, 1538-1542,(1988)
- [44] Hopkins R, DCU MSc Thesis, DCU, 1992
- [45] Costello JT, Ph D Thesis, DCU, 1986
- [46] Kiernan L, Ph D Thesis,DCU, 1995
- [47] Howes MJ and Morgan DV, *Charged Coupled Devices and Systems*, Wiley , (1980)
- [48] J-Y Optical Systems, *The Optics of Spectroscopy, Instruments S A Ltd*, (1988)
- [49] Tousey R, *Applied Optics*, **1**,679-692, (1980)
- [50] Acton Research Corporation, Model VM-521, Operation manual.
- [51] O'Sullivan G, Ph D Thesis, NUI, (1980).

[52] Hughes TP, Plasmas and Laser Light, Adam Hilger Ltd, (1975)

[53] Bekefi G, Principles of Laser Plasmas, Wiley, (1976)

Acknowledgements

I wish to take this opportunity to extend my sincerest thanks to Dr. John Costello for his enthusiasm, foresight and guidance throughout my research I very much appreciate the time spent at weekends on the completion of this research thesis

I would like to thank Prof Eugene Kennedy and Dr Jean-Paul Mosnier for their advice and discussions To the postgrads in DCU especially those in the Laser Plasma Group who have contributed in some way to this thesis, I am very grateful I would especially like to thank William Whitty, Andy Gray and Oonagh Meighan for the craic over the past two years and for the lunchtime soccer and basketball games in the sports complex

I would like to thank Des Lavelle and Tom Connelly in the workshop for their expert machining, design consultation and general assistance (and games of soccer) I am indebted to the other technical and office staff in DCU such as Al Devine for among other things, optical scanning of figures 1 1-1 3 used in this thesis I also acknowledge the financial support from Dublin Corporation and Forbairt - The Science and Technology Agency.

I would like to thank my family who have encouraged me throughout my years in university, especially towards the end Finally I wish to extend my immeasurable thanks to Breege for her constant support and encouragement

Appendices

Appendix A

Normal Incidence Spectrometer

Technical specifications for the Acton Spectrometer and Grating.

• Model	VM-521	
• Focal Length	0.9954 m (1m)	
• Optical System	Normal Incidence (15°)	
• Horizontal Aperture Ratio	f/10.4 with 96mm wide grating	
• Grating	Manufacturer Type Grooves / mm Concave Radius Coating Blaze Angle Blaze Wavelength Ruled Width Ruled Height	Bausch & Lomb Concave Reflective 1200 995.4mm Iridium 2.75° 80nm (First Order) 96mm 56mm
• Wavelength Range (1200g/mm grating)	30 - 325 nm	
• Resolution Capability	0.014 nm	
• Reciprocal Linear Dispersion	0.83 nm/mm	
• Nominal Wavelength Coverage (with Camera Attachment)	21nm	
• Wavelength Accuracy	+/- 0.05 nm	
• Wavelength Reproducibility	+/- 0.005 nm	
• Scanning Mechanism	Sine drive mechanism with precision lead screw external to the vacuum system	
• Focusing	Cam controlled translation motion with micrometer adjustments external to vacuum system for focus adjustments	

Appendix B

Galileo MicroChannel Plate

Characteristics and Specifications of the 6025-FM MCP

•	Plate O D	(mm)	32.74
•	Plate Thickness	(mm)	0.43
•	Active Area	(cm ²)	4.9
•	Electrode Material		Inconal
•	Pore Size	(μm)	10
•	C-C Spacing	(μm)	12
•	Open Area Ratio		55%
•	Bias Angle	(Deg)	12
•	Solid Glass Border		Yes
•	Minimum Electron Gain		3.3 x 10 ⁴
•	Bias Current	(μAmp/Plate)	4 x 10 ⁻¹⁶
•	Maximum Dark Noise	(Amps)	5e ⁻¹² @ 1000V
•	Max Linear Output Density	(μA/cm ²)	10% Bias Current Density
•	Fibre Optic Phosphor		P20
•	Coating		MgF ₂
•	Bakeable	(°C)	350
•	VUV Wavelength Range (Detection Efficiency > 10%)	(Å)	200 - 1800

Appendix C

EG&G Detector System

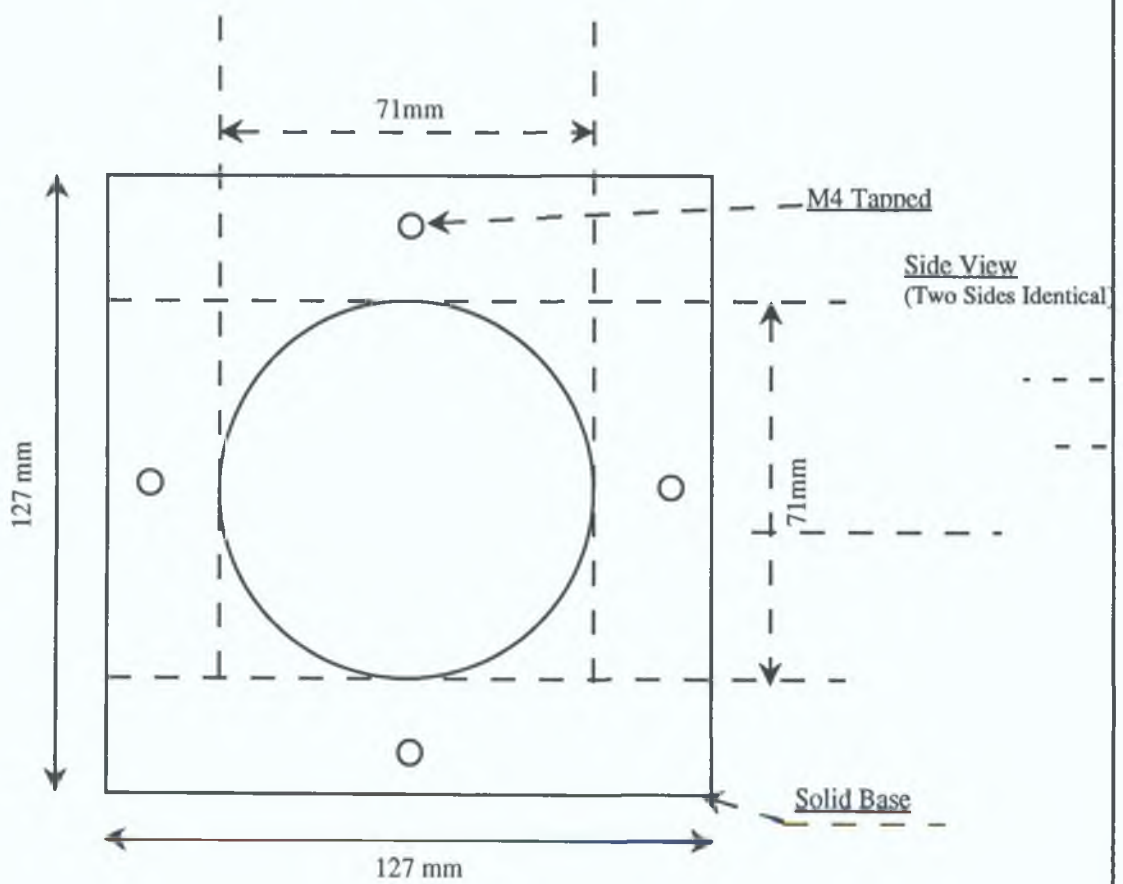
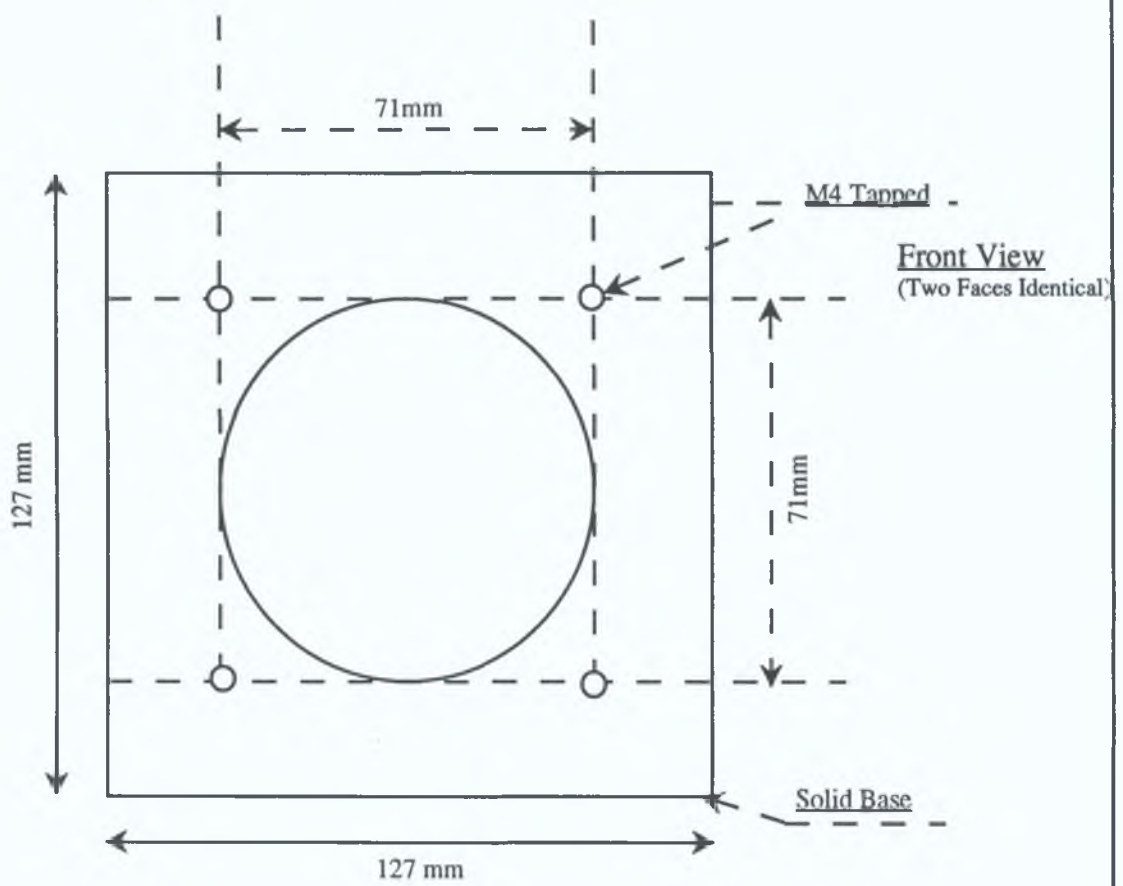
Characteristics of the 1453A silicon Detector and 1471A Detector Interface

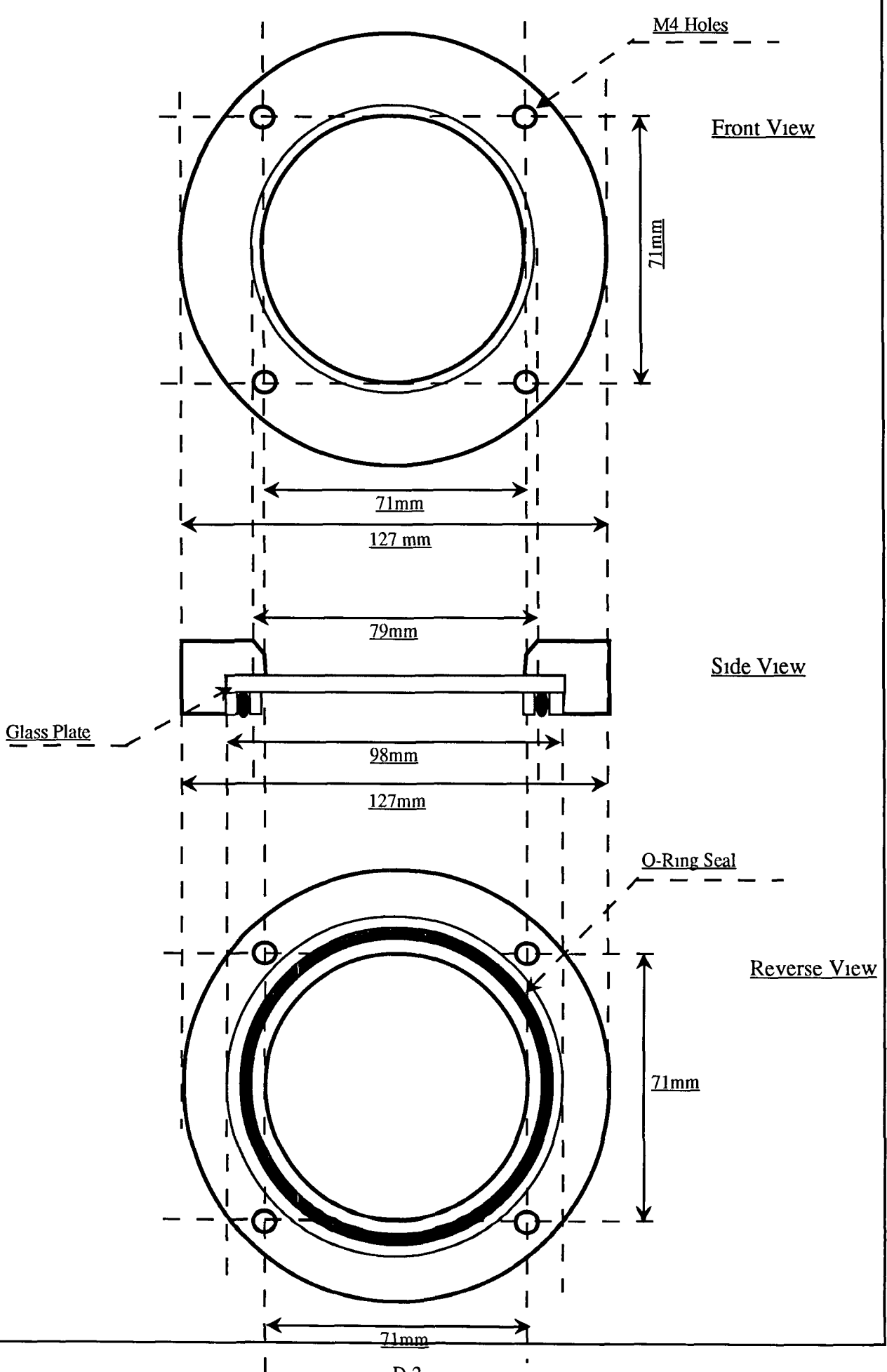
• Detector Type	Silicon Photodiode array (S1 behind fused silica face plate)
• Wavelength Range.	< 180nm to 1100nm
• Quantum Efficiency	70 % at 650nm
• Gain(Photoelectrons/Count)	1350
• Sensitivity(Photons/Count)	1960 at 550nm
• Deviation from Linear Response	< 1%
• Dynamic Range (15-bit)	1 - 32768
• Uniformity of sensitivity	± 5%
• Geometric Distortion	< 1 channel
• Line Width	2 channels FWHM
• Array Length	25mm
• Pixel Number and Size	1024 pixels (25µm c-c) 25 6mm x 2 5mm
• Dark Currents in Counts	910 (800ms at 5 C) 120 (1 Sec at -20 C)
• System Noise (counts/scan ^{1/2})	< 1 5
• Temperature Range	-40 C to 18 C
• Gas Requirements	Must be flushed with dry nitrogen before and during operation

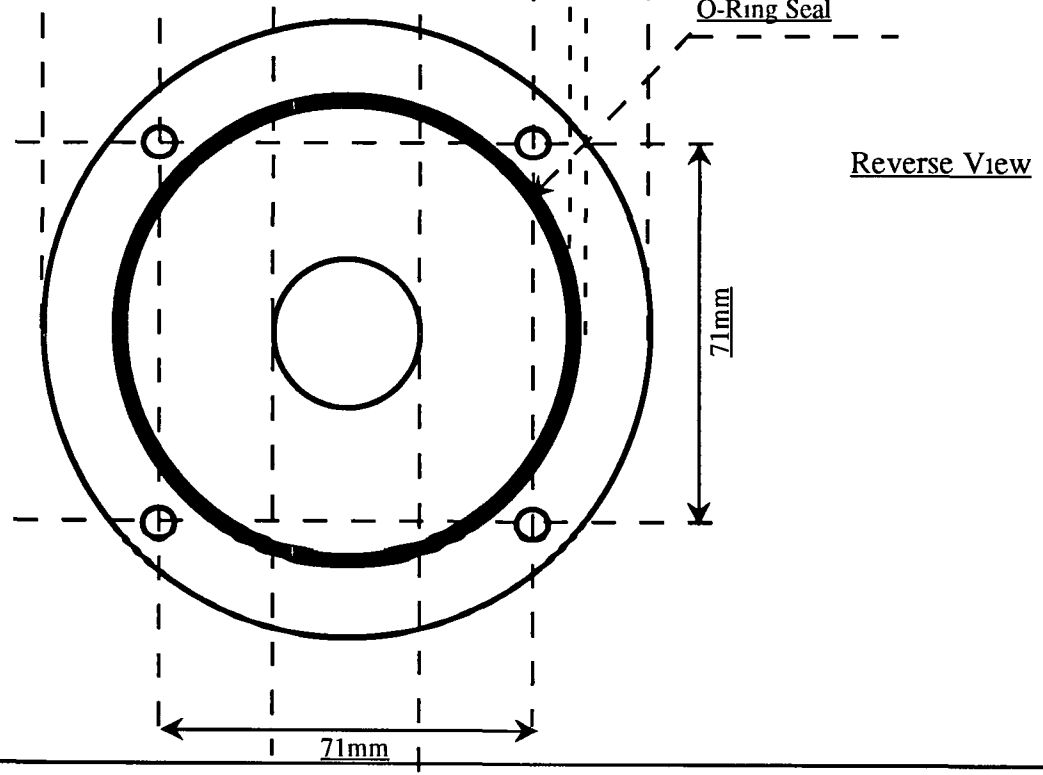
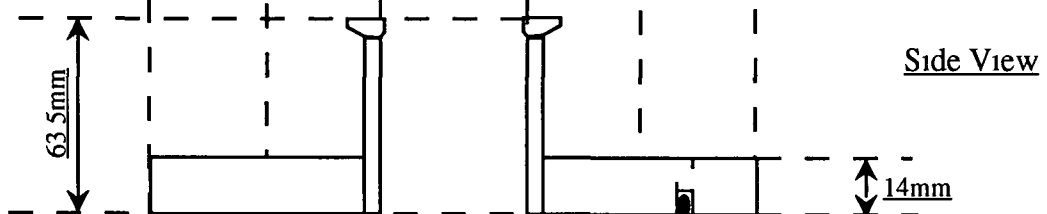
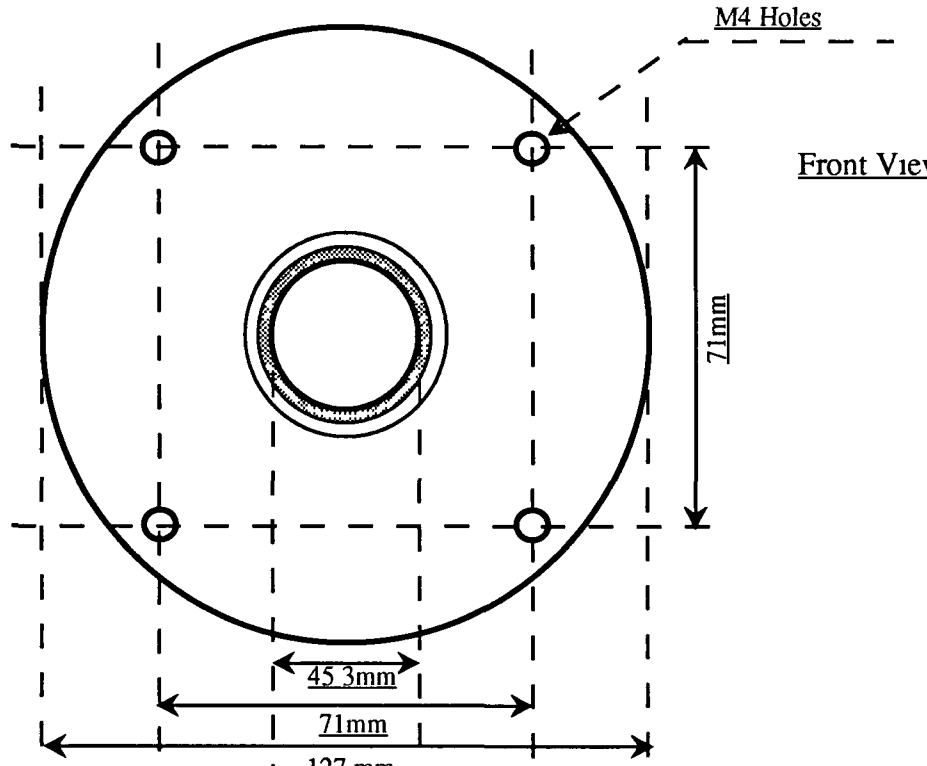
Appendix D

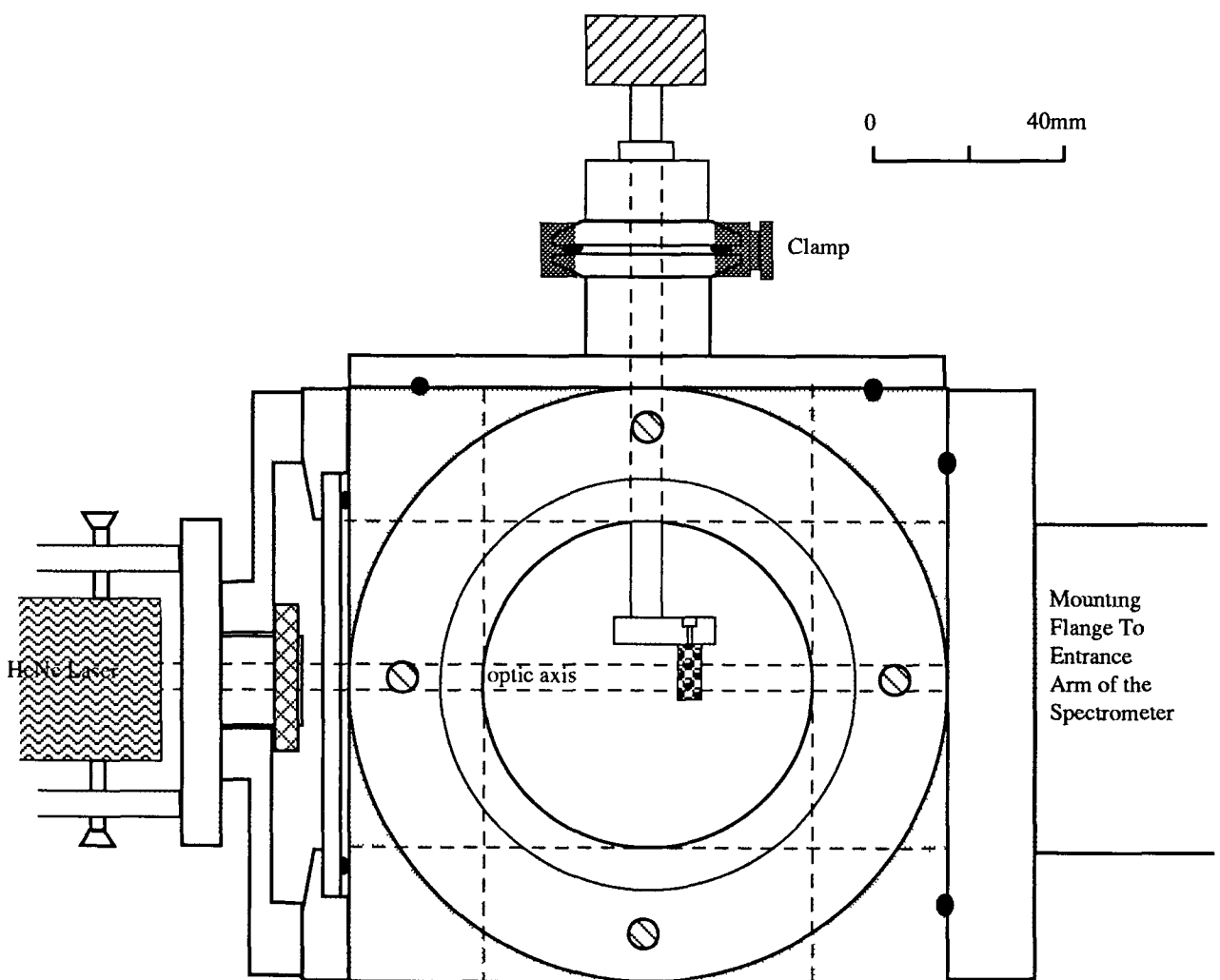
Technical Drawings

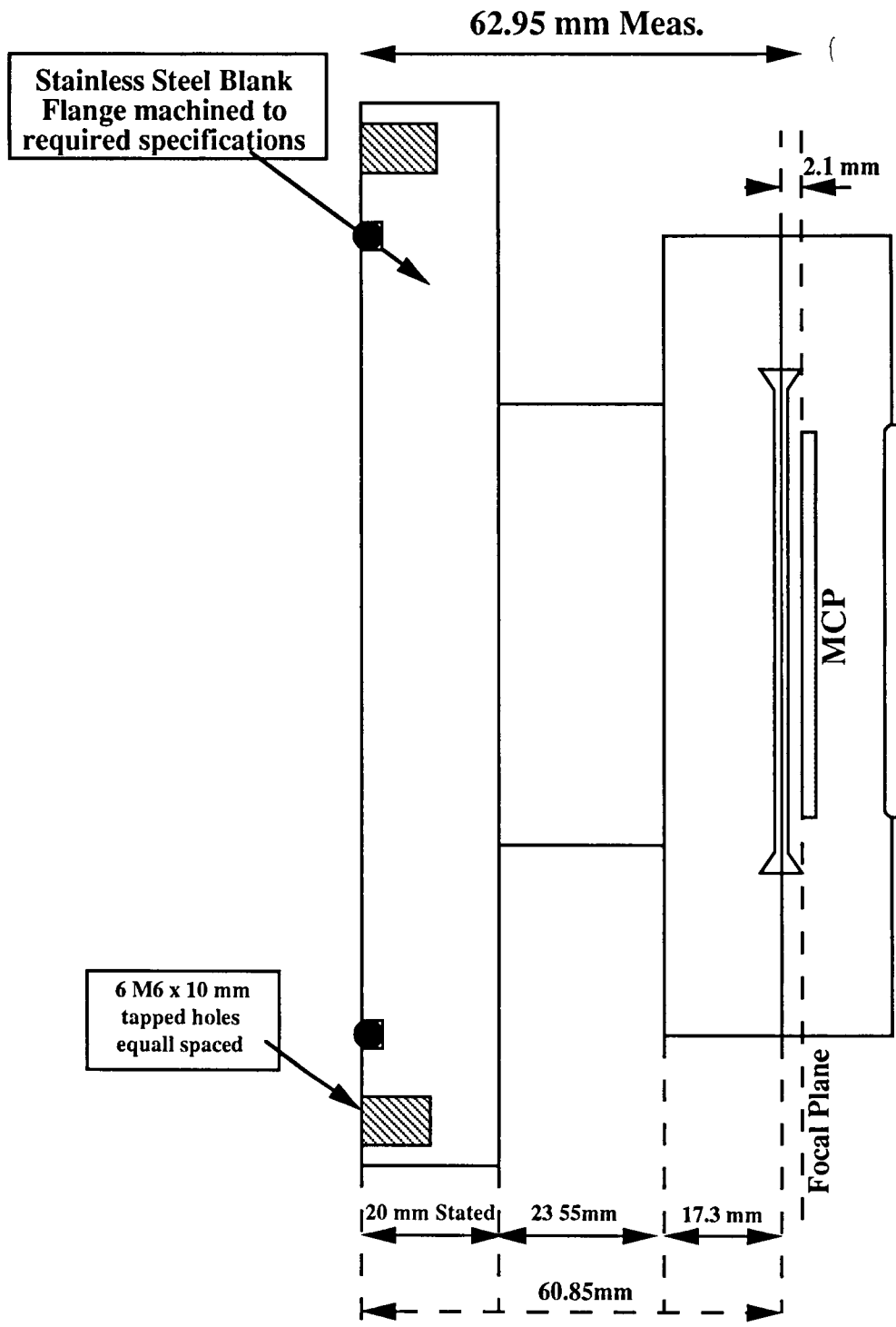
- D-1 Target Chamber Cube
- D-2 Target Chamber Window Flange Assembly
- D-3 Target Chamber DN40 Flange Adapter
- D-4 Front View of Target Chamber Assembly
- D-5 MCP to Exit Arm of Spectrometer Mounting Flange
- D-6 Alignment Laser Mounting Cradle
- D-7 MCP Housing Schematic
- D-8 Exit Arm Detector Mounting Assembly
- D-9 Anchor Plate
- D-10 Diffusion Pump Experimental Setup

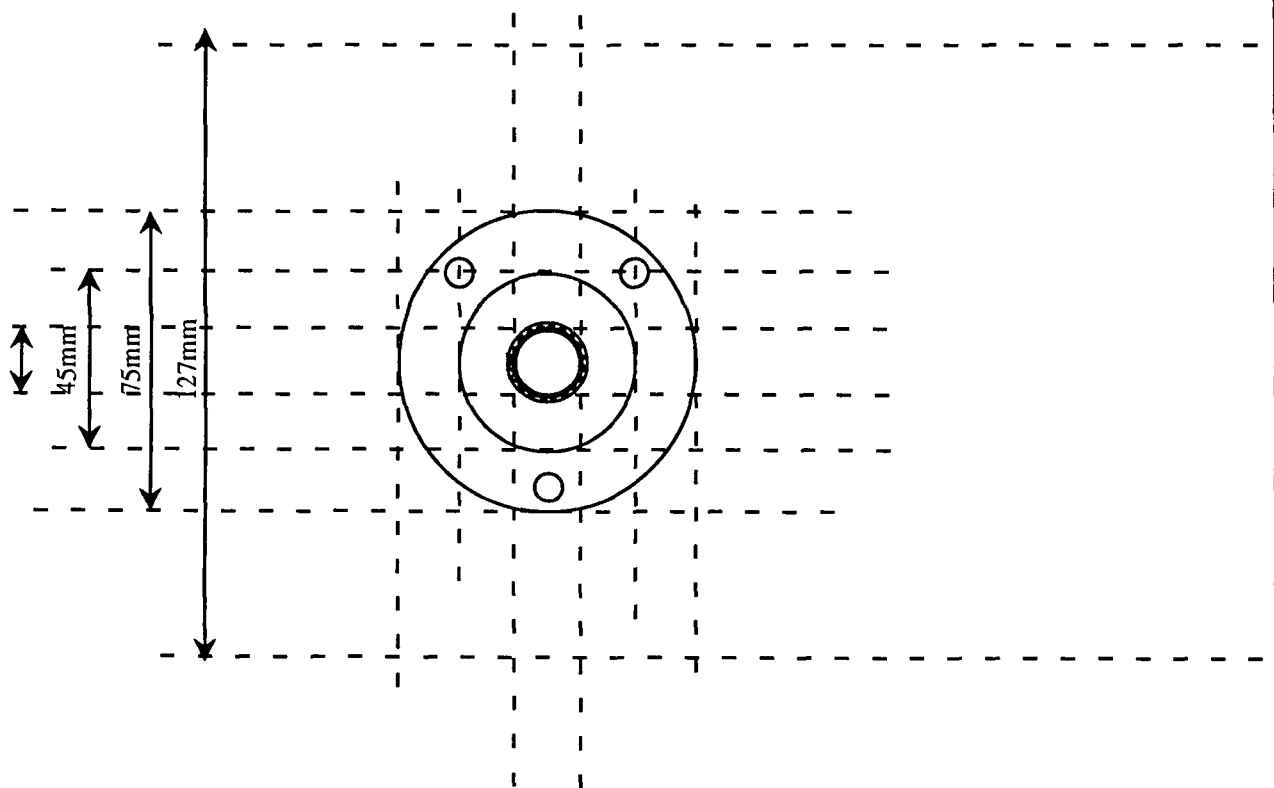
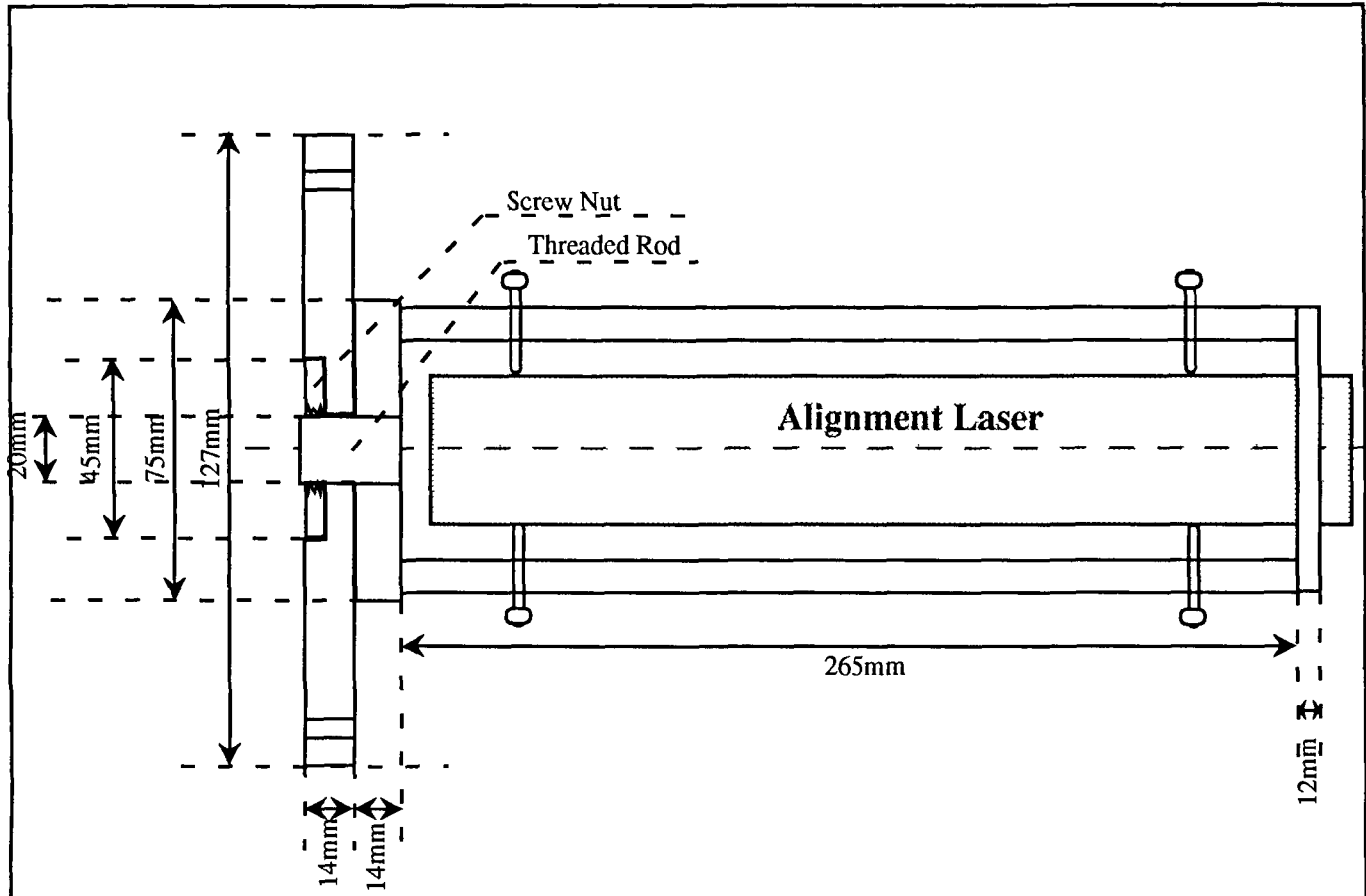












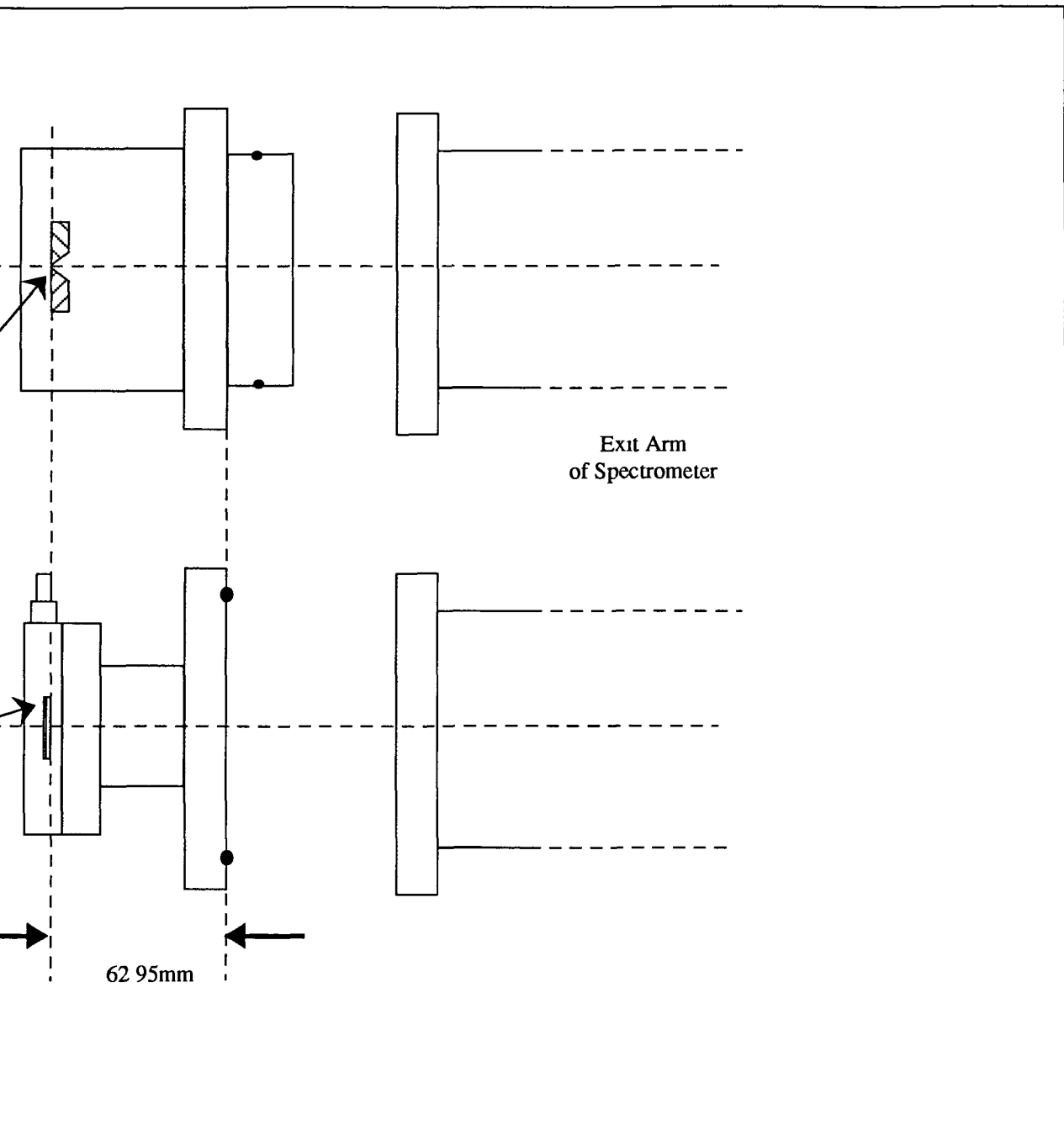
Existing Slit
Housing

Focal point of exit arm

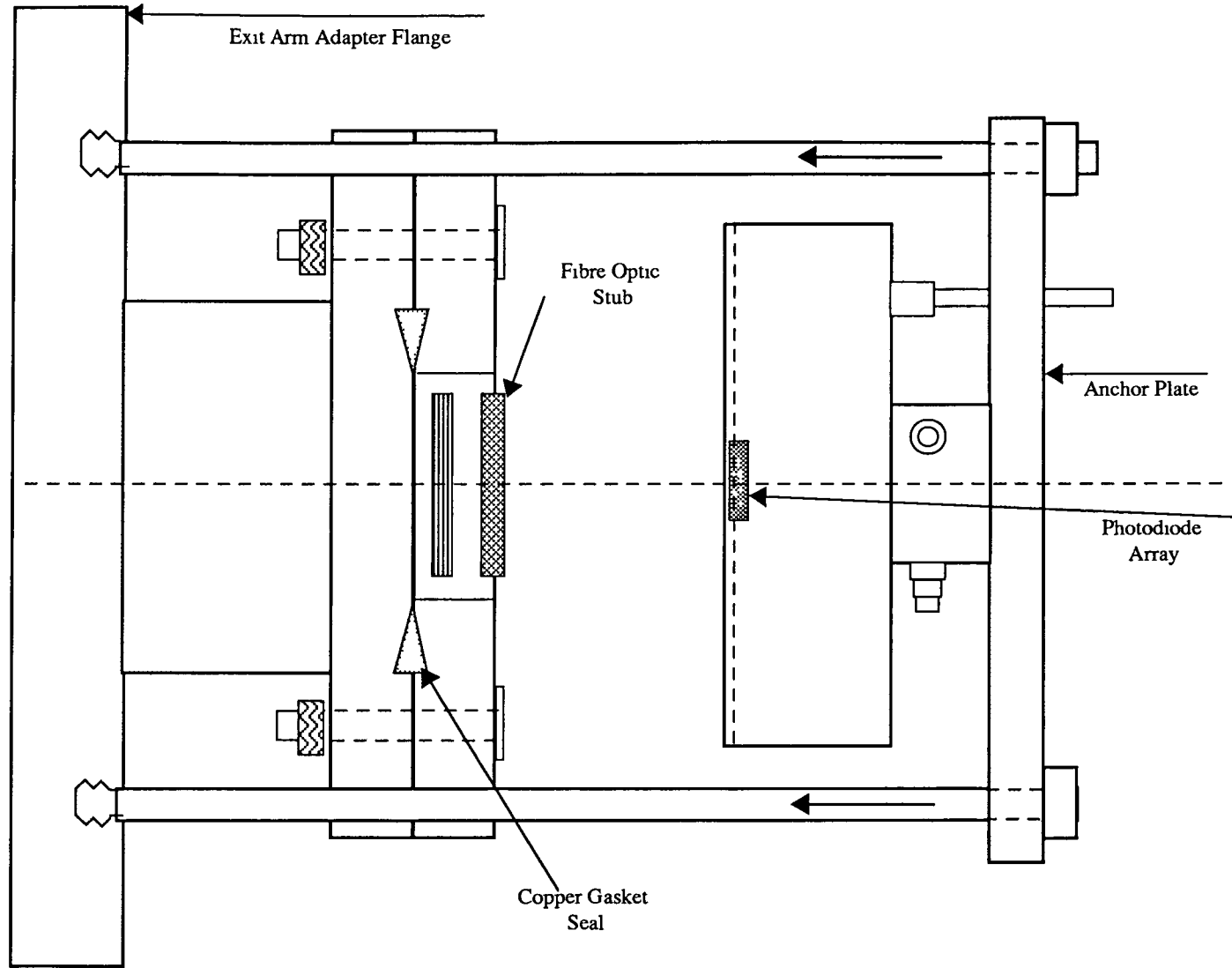
Replacement Assembly

MCP
(face recessed
21mm)

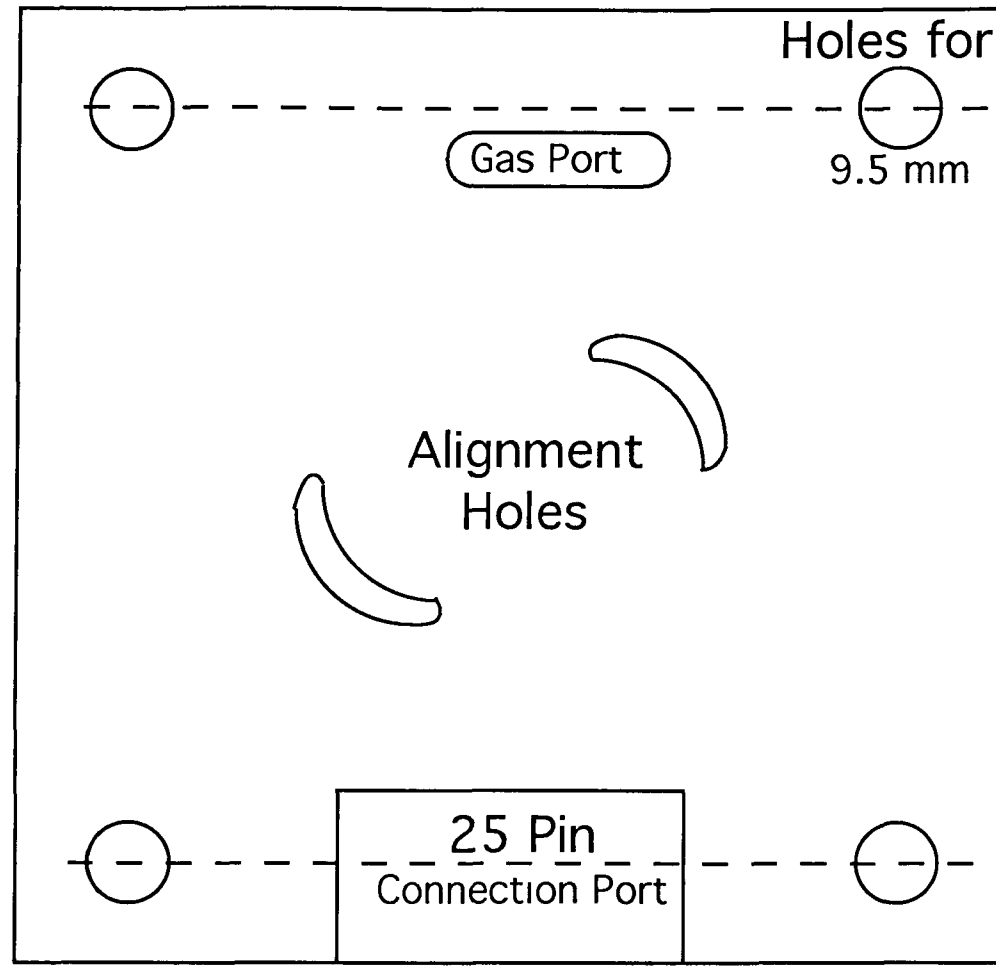
D-7



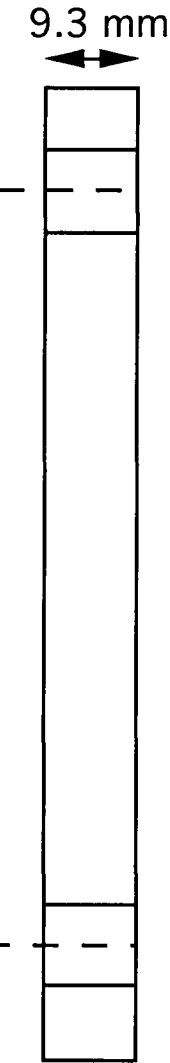
D₈



D-9



Front View



Side View

D-10

